ANALYTICAL TECHNIQUES AND OPERATIONAL PERSPECTIVES FOR A SPHERICAL INVERTED-F ANTENNA

A Thesis

by

DAVID LEE ROLANDO

Submitted to the Office of Graduate Studies of
Texas A&M University
in partial fulfillment of the requirements for the degree of

MASTER OF SCIENCE

December 2010

Major Subject: Electrical Engineering

ANALYTICAL TECHNIQUES AND OPERATIONAL PERSPECTIVES FOR A SPHERICAL INVERTED-F ANTENNA

A Thesis

by

DAVID LEE ROLANDO

Submitted to the Office of Graduate Studies of
Texas A&M University
in partial fulfillment of the requirements for the degree of

MASTER OF SCIENCE

Approved by:

Chair of Committee,	Gregory Huff
Committee Members,	Robert Nevels
	Deepa Kundur
	David Toback
Head of Department,	Costas Georghiades

December 2010

Major Subject: Electrical Engineering

ABSTRACT

Analytical Techniques and Operational Perspectives for a

Spherical Inverted-F Antenna. (December 2010)

David Lee Rolando, B.S., Texas A&M University

Chair of Advisory Committee: Dr. Gregory Huff

The spherical inverted-F antenna (SIFA) is a relatively new conformal antenna design that consists of a microstrip patch resonator on a spherical ground. The SIFA resembles a planar inverted-F antenna (PIFA) that has been conformally recessed onto a sphere. The basic design, simulation, and fabrication of a SIFA were recently reported. The aim of this thesis is to provide a three-fold improvement to the study of the SIFA: the fabrication of a dielectric-coated SIFA, a new analytical model based on the cavity method, and the analysis of a randomly oriented SIFA's operation in a remote networking scenario.

A key improvement to the basic SIFA design is the addition of a lossy dielectric coating to the outside of the sphere for purposes of impedance stability, bandwidth control, and physical ruggedization. The first contribution of this thesis is the fabrication of such a dielectric-coated SIFA. Two antennas are fabricated: a coated SIFA operating at 400 MHz, and an uncoated SIFA operating at 1 GHz for comparison. Both SIFAs are constructed of foam and copper tape; the coating is comprised of silicone rubber and

carbon fiber. The fabricated designs perform with reasonable agreement to corresponding simulations, providing a basic proof of concept for the coated SIFA.

The SIFA was previously studied analytically using a transmission line model. The second task of this thesis is to present a new model using the cavity method, as employed in microstrip patches. The SIFA cavity model uses a curvilinear coordinate system appropriate to the antenna's unique geometry and is able to predict the antenna's performance more accurately than the transmission line model.

The final portion of this thesis examines the performance of the SIFA in a remote network scenario. Specifically, a line-of-sight link between two SIFAs operating in the presence of a lossy dielectric ground is simulated assuming that each SIFA is randomly oriented above the ground. This analysis is performed for both uncoated and coated SIFAs. A statistical analysis of the impedance match, efficiency, and power transfer between these antennas for all possible orientations is presented that demonstrates a design tradeoff between efficiency and predictability.

TABLE OF CONTENTS

CHAPTER Page

LIST OF FIGURES

FIGURE Page

FIGURE Page

LIST OF TABLES

CHAPTER I

INTRODUCTION

Antennas have been used in a myriad of commercial, industrial, and military applications for purposes of communication and sensing [1, 2]. An antenna's ability to transduce guided electromagnetic waves into free space waves is a key component of many modern electrical systems that require communication over free space [3]. Applications range from everyday household items such as wireless routers, Bluetooth-enabled devices, and satellite TV, to state-of-the art reflectarrays, millimeter radioastronomy telescopes, and biomedical antennas [4-7]. New applications are pushing the limit for antenna engineers, increasing the popularity of multifunctional designs that combine several functions into one structure [e.g., 8].

Planar antennas are an important class of antennas, which, due to their thin, flat geometries, can be used to satisfy many application-based constraints. An example is the widely studied microstrip patch antenna, which consists of a metallic patch placed above a flat ground plane and separated from it by a thin dielectric substrate [e.g. 9]. The primary appeal of microstrip antennas and other planar designs is their low cost, easy construction, and low profile [10]. Their low profile in particular makes them useful components in high velocity vehicles – such as aircraft, missiles and spacecraft – where they can fit seamlessly into the aerodynamic demands of the overall structure. Other

---

This thesis follows the style of *IEEE Transactions on Antennas and Propagation*.

common planar designs besides the microstrip patch are slot antennas and planar dipoles [11].

Planar designs have given rise to another class of antennas: conformal antennas, which consist of an antenna that is conformed onto the surface of some pre-defined but arbitrarily-shaped object [e.g., 12-14]. Conformal antennas share in common with planar designs a low profile and amenability to high velocity environments. The basic concept behind a conformal antenna is to take a planar antenna and map it onto a surface that is not flat; in fact, most conformal designs can be traced to a corresponding planar design. Furthermore, the techniques used to analyze planar antennas can often be extended to conformal designs with some degree of accuracy; in general, rigorous analysis of conformal designs can be highly involved due to their non-planar geometries. Conformal antennas have a promising future in antenna engineering due to the high demand for high velocity vehicles and other low-profile applications [15].

The spherical inverted-F antenna, or SIFA, is a recently reported conformal antenna design [16]. Like most conformal antennas, the SIFA has a readily identifiable planar counterpart. It takes its name from the planar inverted-F antenna, or PIFA, from which its topology is derived. The PIFA is a fairly well known design that has been used extensively in applications such as cellular phones [17]. The SIFA is essentially a PIFA design that has been conformed into the surface of a metallic spherical ground plane, with its thickness recessed into the volume of the sphere. This basic SIFA design has been developed in analytical, simulated, and fabricated form [18].

One of the SIFA's most desirable characteristics is its viability as a multifunctional structure. Specifically, this means the SIFA has the potential ability to function as more than just an antenna. Much of the inside volume and surface area of the SIFA's spherical ground plane are relatively isolated from the antenna's required volume on the structure, leaving substantial free real estate on which to mount other electronic devices (e.g., to form an integrated system). Using this ability, the SIFA could potentially be developed into a self-sustaining electrical device performing all manner of communication, sensing, and telemetry. Another appealing characteristic of the SIFA is that its spherical shape yields relatively omnidirectional radiation, so its orientation is not critical.

In the context of a multifunctional structure, the SIFA's spherical geometry lends itself to numerous possible applications. It could be used as a microsatellite, a remote sensing device, or a buoy floating on top of water. Another application, heavily emphasized in [18], is that of biomedical implantation. If the SIFA is physically miniaturized, then it could be ingested like a pill to perform biomedical functions. Another application, which will be emphasized in this thesis, is remote sensing. In this context, the SIFA could be imagined as a rugged, energy-harvesting platform that could perform communication and telemetry in a remote environment with little to no maintenance or human interference.

The goal of this work is to advance the current state-of-the-art (SOA) and state-of-knowledge for the SIFA. This thesis begins with a summary of common antenna analysis techniques and quantities which are subsequently used throughout the work.

This is followed by a brief discussion to microstrip patch antennas, both planar and conformal. The spherical inverted-F antenna (as originally designed and reported) is then introduced, including the basic simulated and fabricated models, along with the relevant performance results. From there, the concept of a dielectric-coated SIFA is detailed; this section includes simulated dielectric SIFA results, details of the fabrication materials and methodologies for a coated SIFA, and results from the first fabricated dielectric SIFA prototype. The thesis then discusses analytical modeling of the SIFA using a cavity model based on the antenna's unique geometry. This model is proposed as an improved and more rigorous analysis tool than the previous transmission line model that had been employed. Calculated results from the model are compared with simulated results and those from the previous transmission line model. Following the cavity model, the thesis changes focus to consider the SIFA as a candidate for remote operation in an *ad hoc* network scenario. The coated and uncoated varieties of the SIFA are compared in a statistical analysis of the antenna's performance in the presence of a lossy dielectric environment; the results are evaluated to formulate a number of trade-offs in SIFA design related to this specific application. The final portion of the thesis offers a summary of the results of this work as well as a discussion of future work related to the SIFA.

CHAPTER II

BACKGROUND

A. Antenna Engineering Basics

A brief discussion of common antenna engineering quantities and methodologies is necessary to set the stage for the analysis of the SIFA in the remainder of this work. The information presented in this section is common knowledge to be found in any fundamental electromagnetics or antenna reference book [e.g. 19]. It should be noted here that the notation used for some quantities can be slightly different depending on the source they are taken from. The notation used in this background section represents the notation that will be used consistently throughout this thesis.

One of the most fundamental analyses that can be performed on any antenna is an evaluation of its impedance match. Typically, an antenna is connected to another electrical device (e.g. the RF front end in a receiving system) via a transmission line (such as the coaxial line). The antenna is typically modeled as a passive load using a complex-valued impedance Z_L. For antennas, this impedance is a function of the operating frequency and antenna topology and is called the input impedance of the antenna. Fig. 1 portrays such a transmission line topology that is terminated in a complex load to represent the antenna. Common electromagnetic theory dictates that a forward travelling voltage wave (i.e., a wave travelling towards the load), V_0^+, experiences reflection at the interface between the load and transmission line. The

reflected wave is V_0^-. The ratio of the reflected wave to the incoming wave is called the reflection coefficient Γ:

$$\Gamma = \frac{V_0^-}{V_0^+} \tag{1}$$

The magnitude of the reflected wave depends on how well the characteristic impedance of the transmission line is matched to the complex impedance of the load. Specifically, the reflection coefficient can be calculated as:

$$\Gamma = \frac{Z_0 - Z_L}{Z_0 + Z_L} \tag{2}$$

In (2), Z_0 is the characteristic impedance of the transmission line. This is a quantity characteristic to the geometry and material properties of the transmission line. By definition, it defines the ratio (3) of the voltage amplitude to the current amplitude on the line.

$$Z_0 = \frac{V_0}{I_0} \tag{3}$$

In (3), the voltage and current can represent either forward or backward travelling waves (or both combined). Note that the reflection coefficient in (2) can, in general, be a complex quantity with a magnitude and phase. The magnitude will always be a value between 0 and 1, with 0 corresponding to no reflection, and 1 corresponding to total reflection.

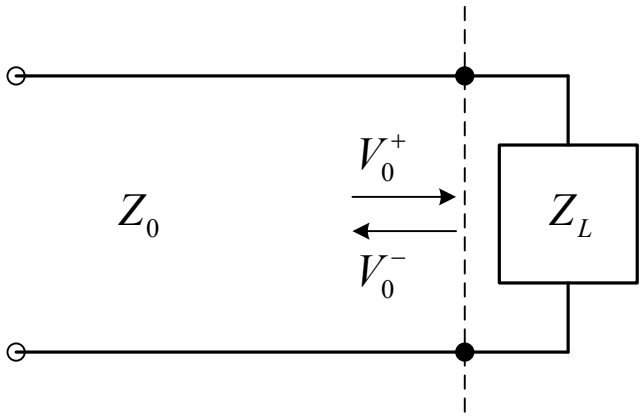

Fig. 1. Transmission line terminated in a load

Generally speaking, in a driven antenna, it is desirable to have the reflection coefficient be as close to zero as possible (i.e. no reflection of the incoming signal). This is due to a number of practical reasons: a reflected signal also means that power is being reflected, so ideal power transfer is not achieved; reflected signals can cause unwanted effects with electronic devices located upstream in the system; and reflected signals can interfere with subsequent incoming signals. To help quantify the amount of reflection experienced at an antenna's input terminal, antenna engineers typically use a quantity called the standing wave ratio (SWR). The name is derived from the fact that the forward and backward travelling waves on the transmission line interfere with each other to form a partial standing wave pattern (i.e., a pattern where the wave amplitude varies in time but not in space). More specifically, the SWR measures the ratio of the maximum amplitude of this standing wave (resulting from constructive interference) to the minimum amplitude of the standing wave (resulting from destructive interference). It turns out that these maximum and minimum amplitudes are simply the sum and

difference, respectively, of the incoming wave and the reflected wave. In most cases, this ratio is expressed in terms of voltage, so the SWR is often called the voltage standing wave ratio, or VSWR. The remainder of this thesis will refer exclusively to the VSWR. By definition, the VSWR is given by (4). Thus, the VSWR can be formulated directly from the reflection coefficient.

$$\text{VSWR} = \frac{V_0^+ + V_0^-}{V_0^+ - V_0^-} = \frac{V_0^+ + \Gamma V_0^+}{V_0^+ - \Gamma V_0^+} = \frac{1+\Gamma}{1-\Gamma} \tag{4}$$

A VSWR of 1 is the lowest possible value and corresponds to the case where there is no reflection; this is the VSWR of an ideal antenna-transmission-line junction. Progressively higher values of VSWR correspond to higher levels of reflection. Typically, in practical designs, antenna engineers often consider any VSWR less than 2 to be acceptable for most applications. In fact, the range of frequencies over which the antenna experiences a VSWR of less than 2 is normally considered to be the antenna's operating bandwidth. This particular definition of bandwidth is called the 2:1 VSWR bandwidth. Fig. 2 is a typical-looking graph which shows the VSWR of an antenna versus the operating frequency (the 2:1 bandwidth is also labeled). Note that on either side of this bandwidth, the VSWR becomes unacceptably high for reasonable use. Thus, the antenna is tuned to operate in a limited range of frequencies; based on (1) - (4), the antenna's impedance (along with the transmission line being used) is critical in this tuning. The VSWR provides an easy way for an antenna engineer to visualize an antenna's basic performance in terms of the operating bandwidth and the quality of the impedance match.

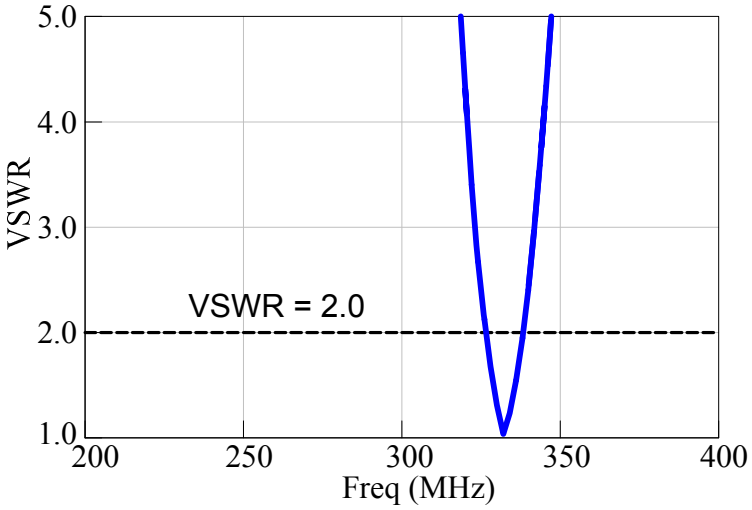

Fig. 2. Typical plot of voltage standing wave ratio (VSWR)

Antenna engineers have another common tool at their disposal to study an antenna's impedance match: the Smith chart. The Smith chart (Fig. 3), provides a graph on which the impedance curve – all of the input impedance values of the antenna over a given frequency range – can be plotted. Although the Smith chart's visible gridlines are in the shape of circles, the chart is based on an underlying Cartesian grid representing the complex plane of the reflection coefficient. The horizontal and vertical axes of this unseen Cartesian grid correspond to the real and imaginary parts, respectively, of the reflection coefficient; the origin (at the middle of the Smith chart) corresponds to zero reflection and is commonly referred to as a perfect match. The visible gridlines on the chart represent lines of constant normalized input resistance and normalized input reactance. These are labeled in Fig. 3 and correspond to the real and imaginary parts of the antenna's input impedance Z_{in} after being normalized by the characteristic

impedance Z_0 of the transmission line. The input impedance of an antenna at various frequencies within a range of interest can be plotted on the Smith chart using these grid lines to form the aforementioned impedance curve. Fig. 3 shows a typical impedance curve for an antenna on a Smith chart, which, in general, is a circular shape. The portion of the curve that passes most closely to the center of the chart corresponds to the lowest point (minimum) of the VSWR curve (Fig. 2).

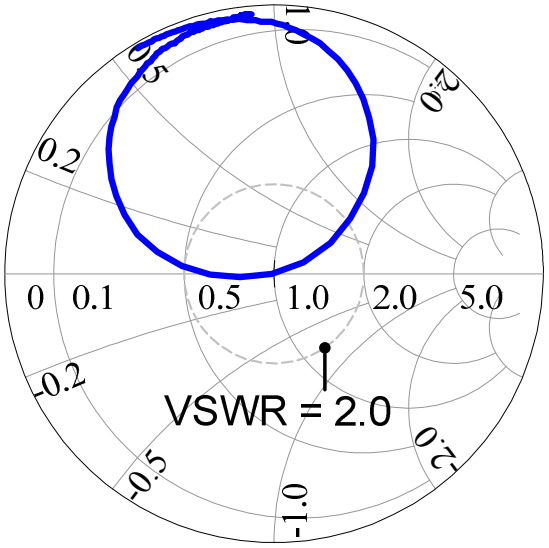

Fig. 3. Typical Smith chart with impedance curve

The details of how the Smith chart is used by antenna engineers is beyond the scope of this background section. It is sufficient to mention how the Smith chart will be used to interpret data in this thesis. Specifically, the following helpful statements can be made as Smith chart interpretation is concerned: the top half of the Smith Chart corresponds to inductive reactances, while the bottom corresponds to capacitive

reactances; and, if the circularly shaped impedance curve of an antenna makes more than one revolution, then the antenna is displaying more than one resonant frequency.

Besides the impedance match, an antenna can also be analyzed for its radiation (both electric and magnetic fields). This section will not develop how radiation information is calculated, but will instead focus on how radiation data is reported. Typically, a radiation pattern is used to summarize an antenna's radiation. The radiation pattern consists of the radiated electric field values on the surface of an imaginary sphere that fully encloses the antenna; these field values are defined for all points on the surface of the sphere, and they are reported as a function of the spherical angles θ and ϕ. The field values are typically given in units of electric field intensity (F/m); sometimes, these values are converted to dB (decibels) and plotted on a logarithmic scale, but the concept is the same. Since the radiation pattern of an antenna, in general, is in three dimensions, graphing and visualizing can be challenging. For this reason, it is customary to take two-dimensional "cuts" of the full three-dimensional pattern. For instance, two-dimensional cross sections can be taken in the xy, xz, or yz planes, corresponding to spherical cuts of $\theta = 90^\circ$, $\phi = 0^\circ$, and $\phi = 90^\circ$, respectively. Often, when linearly polarized antennas are in consideration, the so-called E-plane and H-plane cuts are used; these refer to the planes in which the electric field and magnetic field lie in, respectively (the electric and magnetic fields are perpendicular, of course). Fig. 4 shows several typical radiation pattern cut planes.

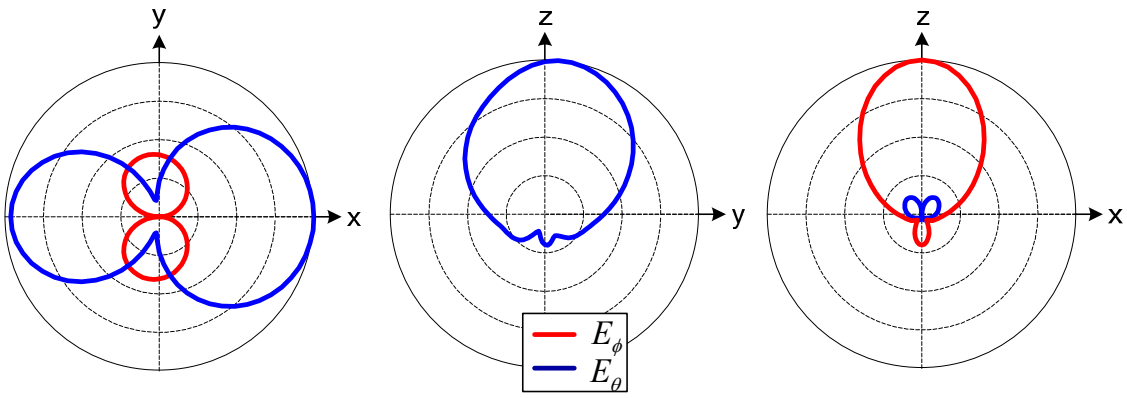

Fig. 4. Typical radiation pattern cut planes. The pattern is of the normalized electric field

B. Microstrip Patch Antennas

The SIFA is a modified version of a microstrip patch antenna, so it is important to give a brief summary of the characteristics of this widely used planar antenna. Fig. 5 shows a picture of a typical microstrip antenna geometry. The shape is essentially a rectangular prism, with the height h usually being considerably smaller than the length l and width w. The top and bottom faces of the prism are metallic, with the bottom ($z = 0$) being a ground plane and the top ($z = h$) being the primary radiating patch. The interior of the prism is the substrate of the patch, typically some type of dielectric material with a relative dielectric constant of ε_r.

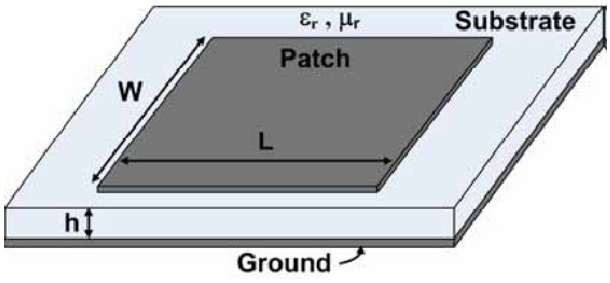

Fig. 5. Typical rectangular microstrip patch antenna

The microstrip patch operates by exciting resonant modes inside the rectangular structure; radiation is achieved by some of these resonant modes leaking power. Mathematically, the modes are similar to those of a 3-dimensional cavity resonator [e.g. 20]; the primary difference is in the boundary conditions. Whereas the cavity resonator has PEC (perfect electric conductor, meaning that the tangential electric field is forced to zero) boundaries on all surfaces, the microstrip cavity only has PEC surfaces on the top and bottom (for the metallic patch and ground plane, respectively). The proper boundary conditions for the microstrip patch are governed by the cavity model [21]. In this model, the four remaining surfaces of the rectangular cavity are assumed to be magnetic walls, or perfect magnetic conductor (PMC) boundaries where the tangential magnetic field is forced to zero and the vertical electric field is a maximum.

The cavity model for the microstrip patch antenna is summarized in Fig. 6, where the boundary condition for each surface has been listed. The cavity model makes several assumptions: the height h of the cavity is assumed to be small enough that the variation of the vertical electric field between the ground plane and the patch is essentially constant; the fringing of fields outside the footprint of the patch is assumed to be very small, so it can be safely ignored; and the electric field inside the cavity is assumed to be essentially normal to the ground plane and the patch, which means that cavity fields are transverse magnetic to the z direction, or TM_z. The TM_z notation means that the magnetic fields are only perpendicular (transverse) to the z direction (since the magnetic field is, by nature, perpendicular to the z-directed electric field). All of these assumptions make solving for the fields inside the cavity considerably easier.

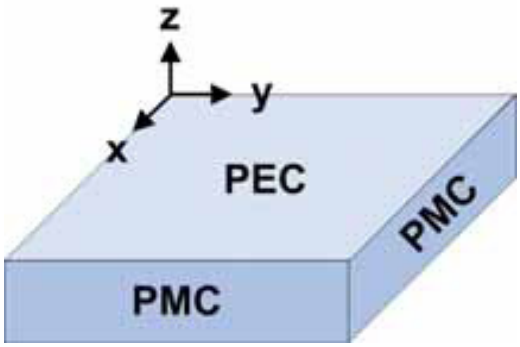

Fig. 6. Cavity model for a rectangular microstrip patch antenna

The intricacies of solving the cavity model for the resonant fields inside the cavity will not be detailed here. The major results will suffice. The process begins by finding the magnetic vector potential $\vec{A}$ inside the cavity (5), which can be used to directly compute the electric and magnetic field components inside the cavity in closed form (see [21]). Note that m, n, and p are integers greater than or equal to zero.

$$\vec{A} = A_{mnp} \cos\left(\frac{p\pi x}{L}\right)\cos\left(\frac{n\pi y}{W}\right)\cos\left(\frac{m\pi z}{H}\right) \tag{5}$$

This vector potential solution is only valid for certain discrete "modes" defined by these integers; each mode has a corresponding resonant frequency, with the lowest frequency mode called the dominant (or fundamental) mode. The factor A_{mnp} is a modal scaling coefficient that depends on the particular mode and the excitation used to excite the cavity. The computed fields are TM_z, with each mode denoted TM_{mnp}. The dominant mode is the TM_{101} mode. Fig. 7 shows a representation of the field distribution in the dominant mode. Note that a half-wavelength of variation occurs along the length of the

patch in the dominant mode; for this reason, the microstrip patch is said to be a half-wavelength resonator.

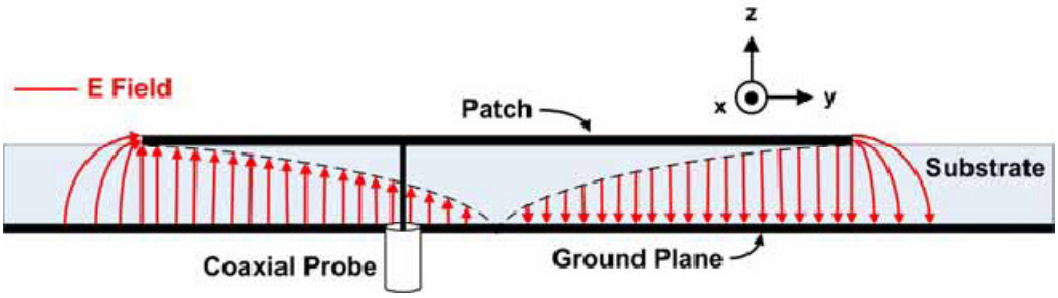

Fig. 7. Field distribution for the dominant TM_{101} mode in a rectangular microstrip patch antenna

The computed fields inside the cavity allow the radiating characteristics of the antenna to be determined. As stated before, the microstrip patch radiates through the mechanism of leaking power from the cavity. Specifically, this leaking energy comes from equivalent magnetic currents on the four PMC side walls of the cavity. These magnetic currents come from the basic electromagnetic principle of equivalence and are related to the electric field on the surface of these walls as:

$$\vec{M}_s = -2\hat{a}_n \times \vec{E} \tag{6}$$

Here, $\hat{a}_n$ refers to the unit normal vector to the surface. From classical antenna theory, current sources produce radiation, so these magnetic currents are the radiation mechanisms of the microstrip patch. In terms of the microstrip cavity model, these radiating surfaces are usually called "slots". It turns out that the two radiating slots along the length of the patch (x-axis) have phases that cancel out their contributions to

radiation, so they can be ignored. The microstrip patch, then, has two primary radiating slots.

Fig. 8 shows two cuts from the radiation pattern of a typical microstrip antenna. Note that the radiation is mostly concentrated in the half-space above the ground plane, with less backward radiation. In this half-space, the radiation is fairly omnidirectional.

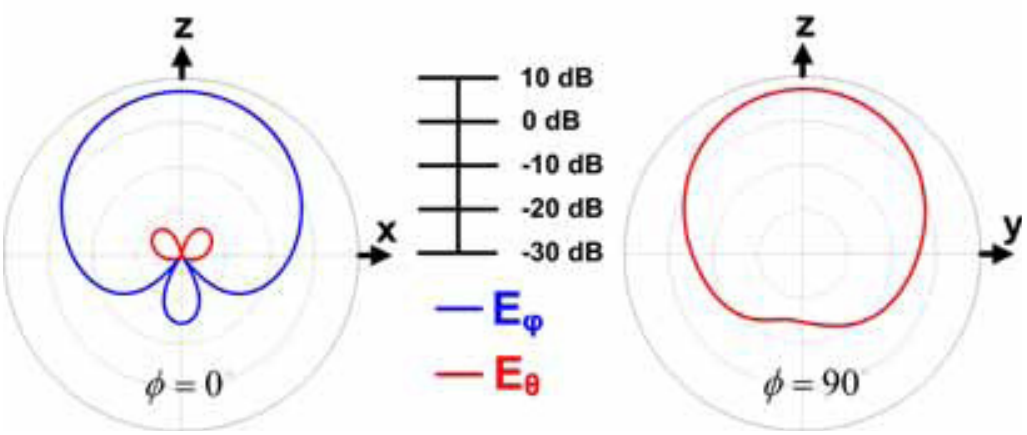

Fig. 8. Radiation pattern of a rectangular microstrip patch antenna

An important modification often used for microstrip antennas is to transform them into the PIFA. The PIFA is derived from a microstrip patch by simply placing a metallic shorting wall at the middle of the patch along its width, and then cutting the physical length of the patch in half [22]. The resulting structure is shown in Fig. 9 with a coaxial probe feed. The name "inverted-F" comes from the fact that, when viewed from the side, the geometry of the PIFA – in particular, the combination of the shorting wall, coaxial probe, and the metallic patch – resembles a sideways "F" that has been inverted. The reason for placing the shorting wall in the patch stems from the field distribution of

the microstrip patch in Fig. 7: at the middle of the patch's width, the electric field drops to zero, so inserting a metallic wall actually does not change the field structure because its boundary condition is automatically satisfied by the distribution of the electric fields. Thus, with the shorting wall present, the patch can be halved without disturbing the frequency of operation or the basic structure of the remaining fields. In essence, the microstrip antenna is transformed from a half-wavelength resonator to a quarter-wavelength resonator of the same frequency.

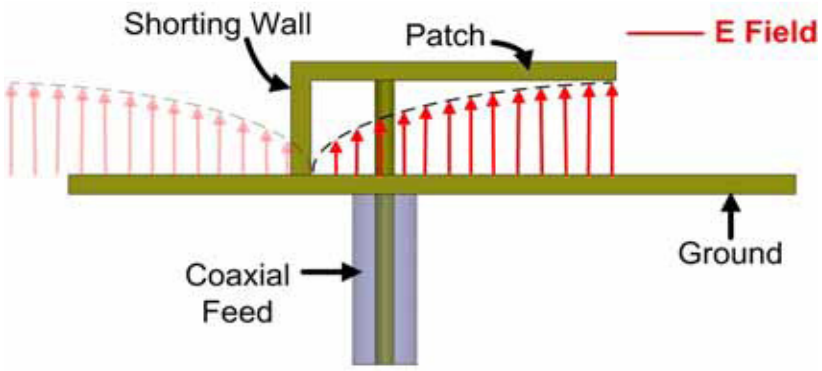

Fig. 9. Planar inverted-F antenna (PIFA) geometry viewed from the side

C. Conformal Microstrip Antennas

An important class of antennas which can be adapted directly from planar antennas (like the microstrip antenna) are conformal antennas. These are antennas which are shaped in order to conform to some predefined surface (which is often curved). Surfaces which are prime candidates to accept conformal antennas are cylinders and spheres [e.g. 23]. Conformal antenna designs often have their genesis in corresponding planar designs, mainly because both types of antennas lie on a surface and have a low

profile, and planar designs are abundant. In fact, planar analysis techniques can sometimes be applied directly to conformal antennas with decent results. Due to their popularity, microstrip antennas have been prime candidates to be adapted into conformal topologies [e.g. 24-25]. Typically, these antennas are dubbed “conformal microstrip antennas” [e.g. 26].

CHAPTER III

THE SPHERICAL INVERTED-F ANTENNA

A. Conceptual and Physical Models

The SIFA, in its most basic conceptual form, is a planar inverted-F antenna (PIFA) that has been conformed onto the surface of a sphere and recessed into its volume. The patch of the PIFA is conformed onto an outer sphere, and the ground plane of the PIFA is conformed onto an inner sphere; the substrate resides in a spherical shell between these two spheres of differing radii. Fig. 10 shows the basic physical model of the SIFA – the result of conformally recessing the PIFA into a spherical chassis. In this case, the patch structure is fed by a coaxial cable from the backside of the sphere. Note that the ground plane beneath the substrate is extended to include most of the outer sphere; this unique feature means that the patch structure resides above an essentially spherical ground. This spherically conformed PIFA has the same basic operating principles and as its planar counterpart: excitation of modal fields within the cavity between the ground plane and the patch lead to radiation "leaking" from the slots of this cavity. Some of the performance characteristics of the spherical design, however, differ from the planar design; for example, the radiation becomes much more omnidirectional than a planar design.

The fundamental SIFA geometry and its most pertinent dimensions are shown in Fig. 11. The orientation of the SIFA relative to the coordinate system in this figure is used as a standard reference system throughout this work. The basic structure consists of

two concentric spheres, the outer sphere having a radius of R_0 and the inner sphere having a radius of R_i. The entire patch structure is contained between the two spheres, with the inner sphere acting as the ground plane. The patch itself, on the outer sphere, has dimensions measured in angles. The width of the patch is ϕ_w. The patch is separated from the outer sphere ground plane by a gap with an angle θ_g; on the opposite side of the patch, it is connected to the outer sphere ground plane by a shorting strip with an angular length of θ_s. These two angles together determine the angular length of the patch, which is simply $\theta_l = \frac{\pi}{2} - \theta_g - \theta_s$. The coaxial feed is located in the middle of the patch by width and at angle of θ_f along the length of the patch.

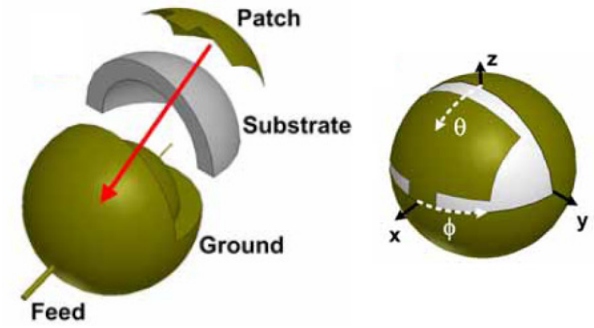

Fig. 10. Physical model of the SIFA

Note that, instead of the shorting wall being placed vertically (i.e. radially in the case of the SIFA) between the inner sphere ground plane and the patch, it is placed on the outer sphere between the metal of the patch and the metal of the ground plane on the

outer sphere. This is a slight variation from the PIFA design, since the shorting wall is "parallel" to the ground plane and patch, rather than perpendicular as in the PIFA.

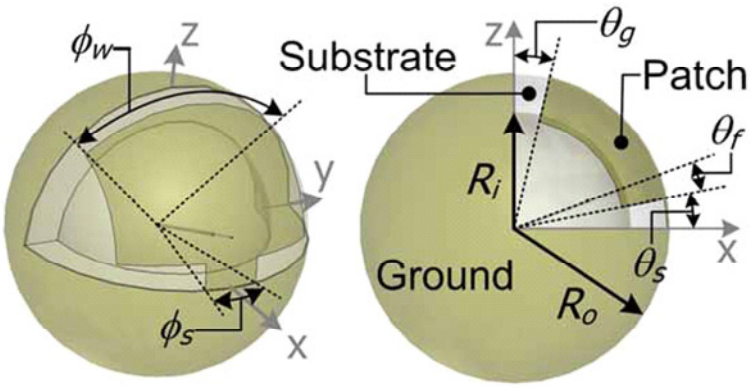

Fig. 11. Basic SIFA geometry and dimensions

Unlike the PIFA, which typically acts strictly as a radiating structure, the SIFA is inherently a multifunctional structure since it has the potential to perform tasks other than that of an antenna. This arises primarily from the fact that the patch structure occupies only about one quarter of the surface area of the outer sphere and less than one quarter of the inside volume of the sphere. This remaining space inside the structure and on its surface is free real estate, so to speak, in which other devices can be mounted in an integrated electronic system. For example, transmitting, receiving, and digital signal processing hardware, along with a local power supply, could be mounted in the SIFA to form a complete communication system. Thus, the SIFA can be thought of as a structural platform with radiating capabilities that can be adapted to a variety of applications. One such application would be biomedical: the SIFA could be miniaturized down to the size of a pill, allowing it to be ingested for endoscopy. Another possibility is

remote sensing: the SIFA could be equipped as a rugged, self-supporting telemetric device that could operate in a remote area for a long period of time, transmitting data that onboard sensors acquired. Other possibilities include using the SIFA as a buoy floating on water or as a micro-satellite. At its heart, then, the SIFA is more than just a mere mapping of a planar antenna to a conformal design: it is multifunctional adaption of a planar design.

B. Simulated Design

The dimensions of the original SIFA design are given in Table 1. This particular design was chosen to operate in the Medical Implants Communication Services (MICS) frequency band from 402 MHz to 405 MHz. This operating frequency range was chosen based on the original assumption that the SIFA could be used as a implantable biomedical device, a task for which this particular frequency band is devoted. Although the dimensions of this SIFA are not nearly small enough for biomedical applications, it was a good starting point for SIFA analysis that made fabrication and measurement achievable by hand. Even though a number of miniaturization techniques could be employed to bring the size of the antenna down to a reasonable range for this application, none were used in this preliminary design so as not to complicate the process. This SIFA design simply acted as a prototype and a proof of concept.

Table 1. Dimensions of simulated MICS band SIFA

Deign Variable	Description	Value
R_i	Inner radius	76.2 mm
R_o	Outer radius	101.6 mm
ϕ_w	Patch width	90°
ϕ_s	Short width	10°
θ_f	Feed angle	10°
θ_s	Short length	11°
θ_g	Gap width	13°

The basic SIFA model can be easily simulated in [27], an electromagnetic simulation software that uses finite element code. The SIFA is very amenable to construction in this three-dimensional CAD environment. Fig. 12 shows a snapshot of the SIFA model. A simple frequency sweep from 300-500 MHz provides the basic impedance characteristics of the SIFA as a function of frequency, and the radiation pattern can be computed at 402.5 MHz (the middle of the MICS band) for the ideal operational radiation characteristics.

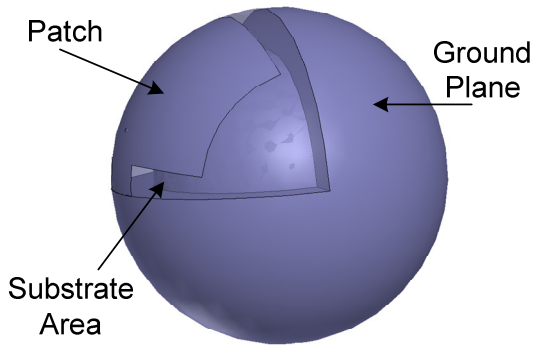

Fig. 12. Simulation model of MICS band SIFA

Fig. 13 shows the Voltage Standing Wave Ratio (VSWR) of the SIFA versus frequency, and Fig. 14 shows the corresponding impedance curve on the Smith Chart. Clearly, the VSWR 2:1 bandwidth falls within the desired MICS band, with a resonance at around 400 MHz. The Smith chart shows a mostly inductive impedance curve.

Fig. 15 plots the simulated radiation pattern of the SIFA. Note that the pattern is fairly omnidirectional in all cut planes; this is one of the advantages of taking a planar antenna and conforming it onto a sphere.

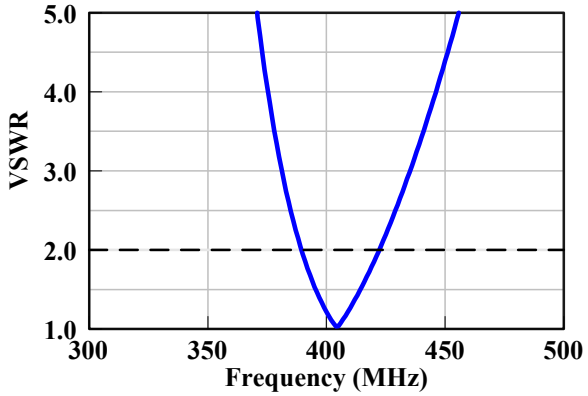

Fig. 13. Simulated VSWR of MICS band SIFA

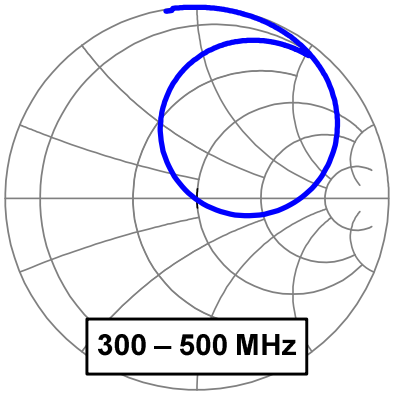

Fig. 14. Simulated impedance curve of MICS band SIFA

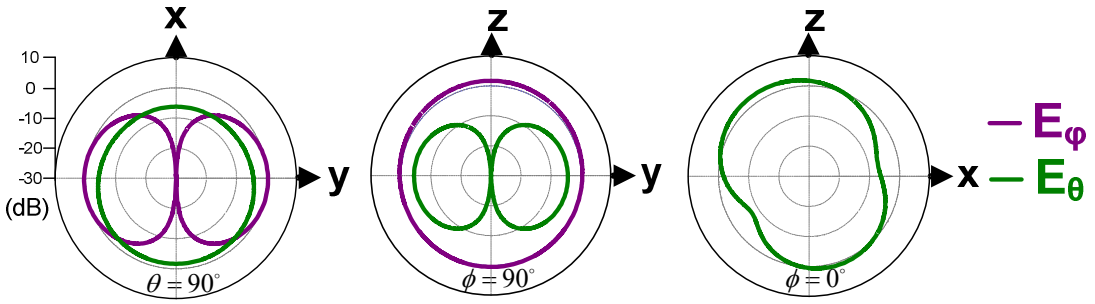

Fig. 15. Simulated radiation pattern of MICS band SIFA

C. Fabricated Design

A simple fabrication and measurement process was used to verify the results of the simulation. A SIFA prototype was constructed using foam and copper tape. All of the details of the fabrication process will not be outlined here, but can be summarized as follows: spherical foam balls were used as the inner and outer spheres of the SIFA, and copper tape was attached to these spheres to form the ground plane and the patch structure; the copper tape was soldered together to form a continuous electric conducting surface. A semi-rigid coaxial probe was inserted into the back of the outer foam sphere and pushed through the foam to the patch structure; the outer conductor of this probe was soldered to the inner sphere ground plane beneath the patch, and the inner conductor of the probe was soldered to the patch structure on the outer sphere. This probe allowed the SIFA to be fed by a coaxial cable externally (although in the simulations, the probe originated in the interior of the SIFA). A picture of the first fabricated SIFA is shown in Fig. 16.

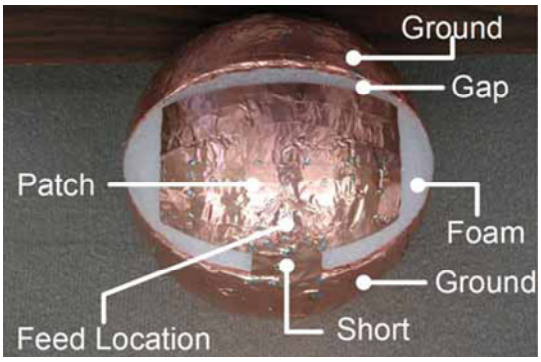

Fig. 16. Picture of fabricated MICS band SIFA

The SIFA prototype was measured using a network analyzer to compare its performance to that of the simulated antenna. Fig. 17 shows the results of these measurements in terms of the VSWR and the Smith chart impedance curve. Both graphs include the simulated data for comparison. The simulated and measured results agree well. Clearly, the simple hand construction of the SIFA using foam and copper tape proved to be a fairly accurate physical realization of the SIFA simulation model. More precise fabrication methods can hopefully provide even more accuracy.

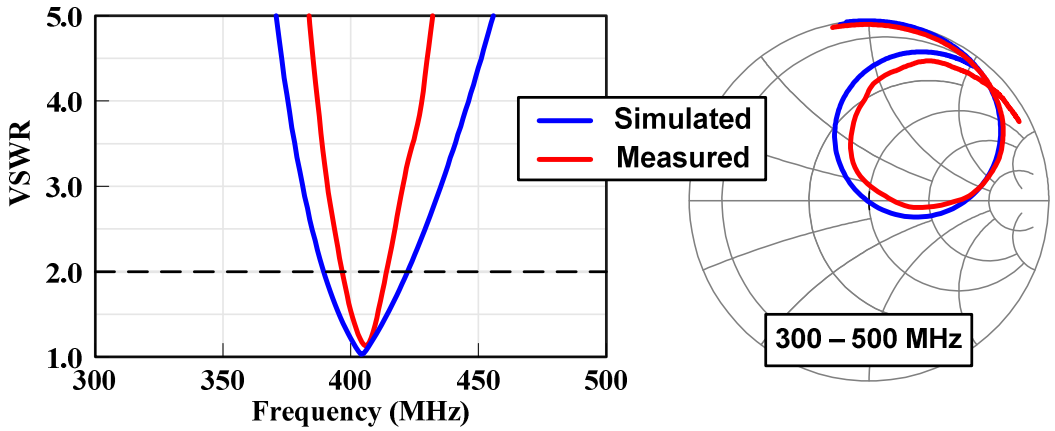

Fig. 17. Measured results compared to simulated performance, MICS band SIFA

CHAPTER IV

A DIELECTRIC-COATED SIFA

A. The Concept of a Coating

An important modification that can be made on the basic SIFA design is to add a thin spherical dielectric coating to the outside of the antenna. This dielectric coating can be designed with various relative dielectric constants and dielectric loss tangents to change the operating characteristics of the antenna. The coating can be thought of as a dielectric resonator in the shape of a spherical shell; the resonator is excited by the patch structure beneath it. In addition to the coating around the SIFA, the substrate under the radiating patch is also changed into dielectric material to match that of the coating. Having the dielectric material above and below the patch strengthens the effect of the dielectric (i.e. increases the effective dielectric constant), similar to adding a superstrate in a planar antenna [e.g., 28].

A dielectric coating on the SIFA can provide many advantages. Electromagnetically, the coating changes the resonant frequency of the antenna. Specifically, as the relative dielectric constant of the antenna increases, the resonant frequency decreases [e.g. 29]. In this way, a variety of lower resonant frequencies can be achieved while maintaining a constant physical size for the SIFA; in other words, the electrical size of the antenna (the ratio of the physical size to the wavelength of the operating frequency) can be reduced. Alternatively, the resonant frequency of the antenna can remain constant while the physical size decreases, with a higher dielectric

material leading to smaller physical designs. Thus, a coating allows for a broad range of miniaturization and resonant frequency shifting. It must be noted, however, that in any case, a higher dielectric constant in the coating always decreases the electrical size of the antenna. This in turn causes the radiating efficiency of the antenna to decrease [30]. This is one unwanted side-effect of the coating that cannot be avoided. However, depending on the demands of the specific application, this negative aspect of the coating can be tolerated as long as the benefits outweigh it; thus, the coating introduces a design trade-off for the SIFA.

Another electromagnetic effect of a dielectric coating around the SIFA is the possibility of increased performance in dielectric environments (i.e. when the SIFA is not operating in free space, but in the presence of one or many dielectric materials). If the coating can be made to have dielectric properties close to that of the media it will be surrounded by, then the detuning effect that this outside media would normally have on the antenna can be reduced by the better dielectric "match" between this media and the coating [31]. Additionally, the physical separation between the metallic patch and the outside environment created by the coating naturally reduces the effect of this outside environment on the antenna performance.

The idea of a dielectric coating can be taken a step further by introducing dielectric loss into the coating. Although this loss will cause the radiating efficiency of the antenna to be lowered, it can have a number of beneficial effects. First, coated designs with high dielectric constants tend to have very narrow bandwidths because of the electrical miniaturization caused by the dielectric; a lossy coating can lower the

quality factor of the antenna, in turn causing the bandwidth to widen [32]. This effect may actual be crucial in very electrically small SIFAs, where the bandwidth would almost be negligible for a strong, lossless dielectric coating. Another benefit of a lossy coating could be stabilization of the SIFA's impedance bandwidth in the presence of changing outside environments. The SIFA can be tuned fairly well to operate in free space, but if its surroundings change, the operating bandwidth needs to remain in the desired range. As mentioned before, the physical separation caused by the coating can help to alleviate this problem. A lossy coating can be even more effective, as the loss allows for a wider bandwidth and more stable impedance match such that the antenna does not detune in the presence of different surroundings. The effects of a lossy coating are explored more in Chapter VI, where the SIFA's performance in a remote network scenario is analyzed.

B. Simulated Dielectric SIFA Designs

A wide variety of design variations can be achieved by a dielectric coating around the SIFA. Several different simulated designs are reported here to demonstrate the range of possibilities.

The most basic variation accomplished by a coating is to drastically reduce the physical size of the antenna, while maintaining a constant resonant frequency. Fig. 18 shows a simulated coated design that is only 26 mm in diameter (including the coating); this design was presented previously in [33]. The coating (as well as the patch substrate) has a relative dielectric constant of 53; no dielectric loss is present in the coating. It was

designed to operate at in the MICS band (the same frequency range as the original uncoated SIFA design) at just over 400 MHz. Thus, a physical size reduction of 87% from the original SIFA design is achieved for the same operating frequency. The antenna was also designed for the purpose of operating in a lossy dielectric environment. This particular choice had the specific application of biomedical implantation in mind, as was previously discussed as a possibility for the SIFA; because of this choice, this particular antenna does not function well in free space. Fig. 18 also shows a commercially available biomedical antenna [34] (which can be ingested) next to this SIFA design as a physical comparison to show that a satisfactorily small SIFA can be achieved for biomedical purposes through use of a coating.

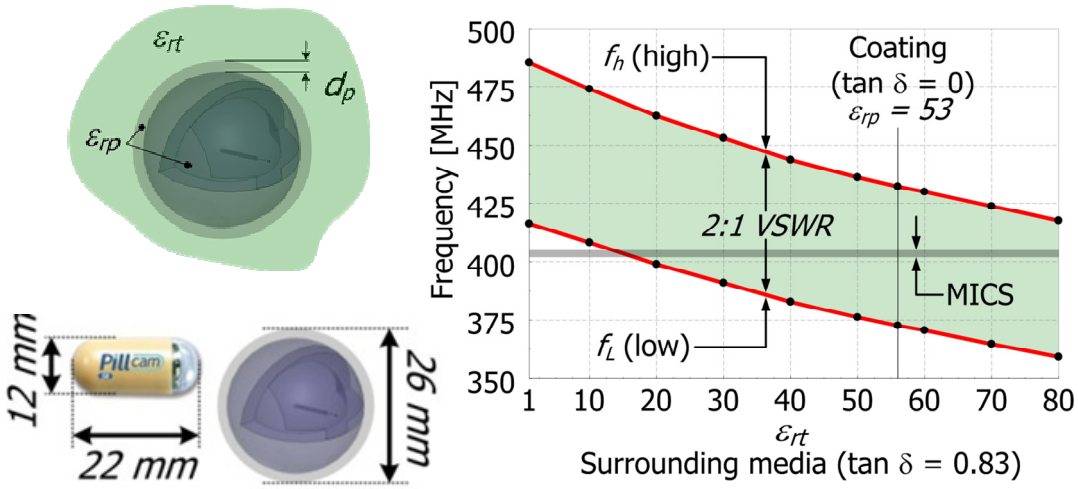

Fig. 18. Miniaturized dielectric SIFA. The size of this antenna is on the scale of commercially available biomedical devices

The simulated performance of this miniaturized SIFA is also summarized in Fig. 18. Specifically, the minimum and maximum frequencies in a 2:1 VSWR bandwidth are

reported as the dielectric constant of the surrounding media is varied (the media is given a constant dielectric loss tangent of 0.83). These minimum and maximum frequencies are shown as red lines on a vertical frequency scale that are functions of the relative dielectric constant of the surrounding media. The region between the minimum and maximum frequencies is shaded blue to represent the antenna's 2:1 VSWR bandwidth. Also shown is the MICS operating frequency band (shaded gray). The SIFA clearly maintains a stable 2:1 bandwidth for surrounding media relative dielectric constants ranging from about 15 all the way to the maximum simulated value of 80. Thus, the high dielectric coating allows the SIFA to be well "matched" to similarly high dielectric media, as would be encountered in a biomedical application. Note that, as mentioned earlier, this particular SIFA does not have a good VSWR in free space operation. Nonetheless, this simulated antenna provides an informative look at how a dielectric SIFA can achieve miniaturization as well as stable performance in a changing outside media.

In this work, another set of dielectric SIFA simulations was performed using a design with the same outer radius as the original MICS band SIFA. The original design was modified by adding a lossy dielectric coating of 2.5 cm around the outside and by changing the dimensions of the patch and the angle of the coaxial feed. The coating and substrate of the patch were given a relative dielectric constant of 50 and a dielectric loss tangent of 0.02. This high dielectric constant reduced the resonant frequency to around 74.5 MHz. The simulation model is shown in Fig. 19.

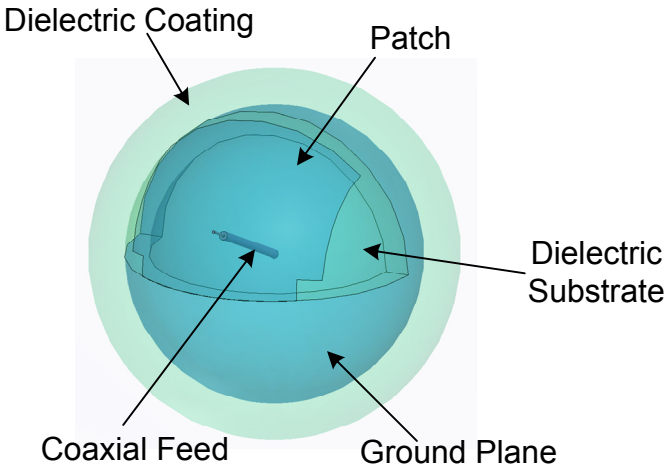

Fig. 19. 74.5 MHz dielectric SIFA simulation model

For this 74.5 MHz design, a parametric study was performed to determine the effects of the patch dimensions and the feed angle on the SIFA's performance. Also, for comparison, the original MICS band SIFA was subjected to similar parametric variations. The parameters varied for this study were the feed angle θ_f, the short width ϕ_s, the short length θ_s, the gap angle θ_g, the patch width ϕ_w, and the inner radius R_i.

The feed angle θ_f was varied for the 74.5 MHz (lossy coating) and MICS band 402 MHz (no coating) designs in the increments shown in Fig. 20. For the coated design, changing the feed angle changes the impedance match while keeping the resonant frequency essentially constant. Clearly, then, the feed angle can be used as a powerful design variation to match the coated design's impedance without changing operating frequency. For the uncoated design, changing the feed angle has a significant effect on the resonant frequency, and it can also upset the impedance match.

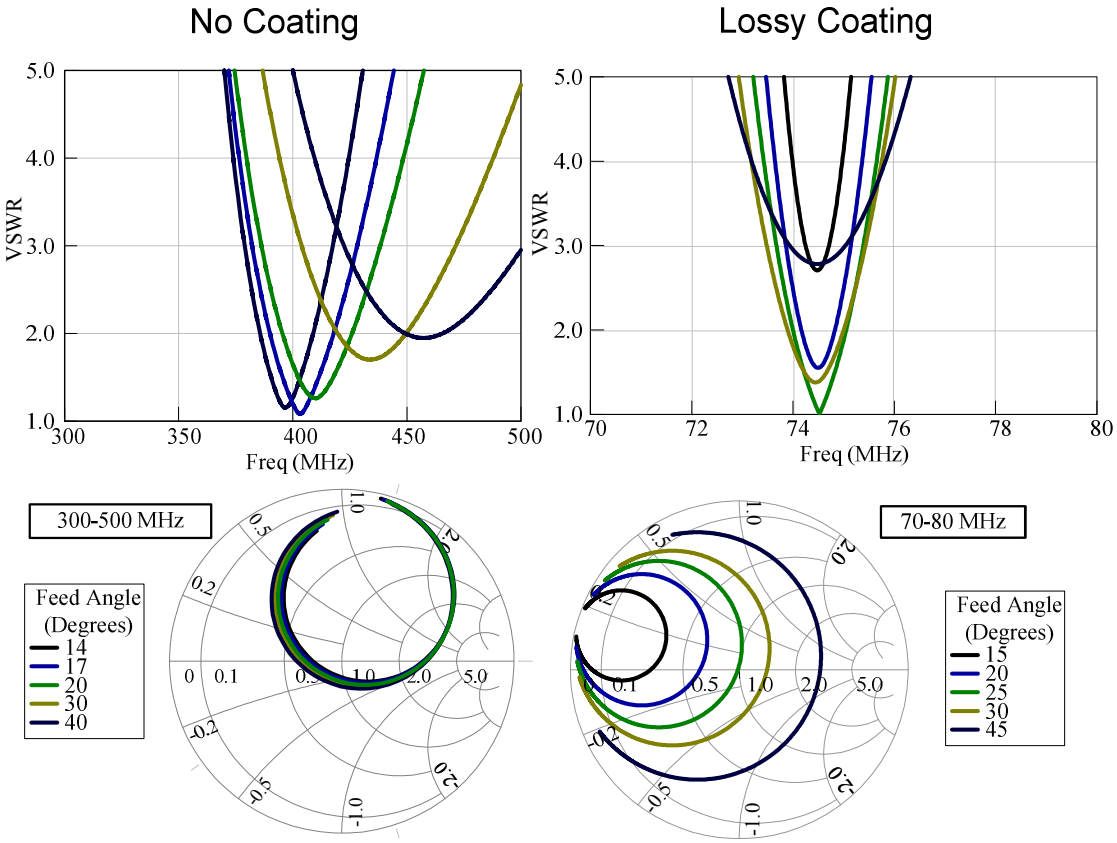

Fig. 20. Variation of the feed angle for coated and uncoated SIFAs

The variations on ϕ_s are shown in Fig. 21. For the coated design, varying the this parameter achieves significant shifting of resonant frequency with little disruption of the impedance match; this could be a useful design variation. For the coated design, variations in the short width cause significant impedance mismatches and frequency shifts; these would be difficult to control from a design perspective.

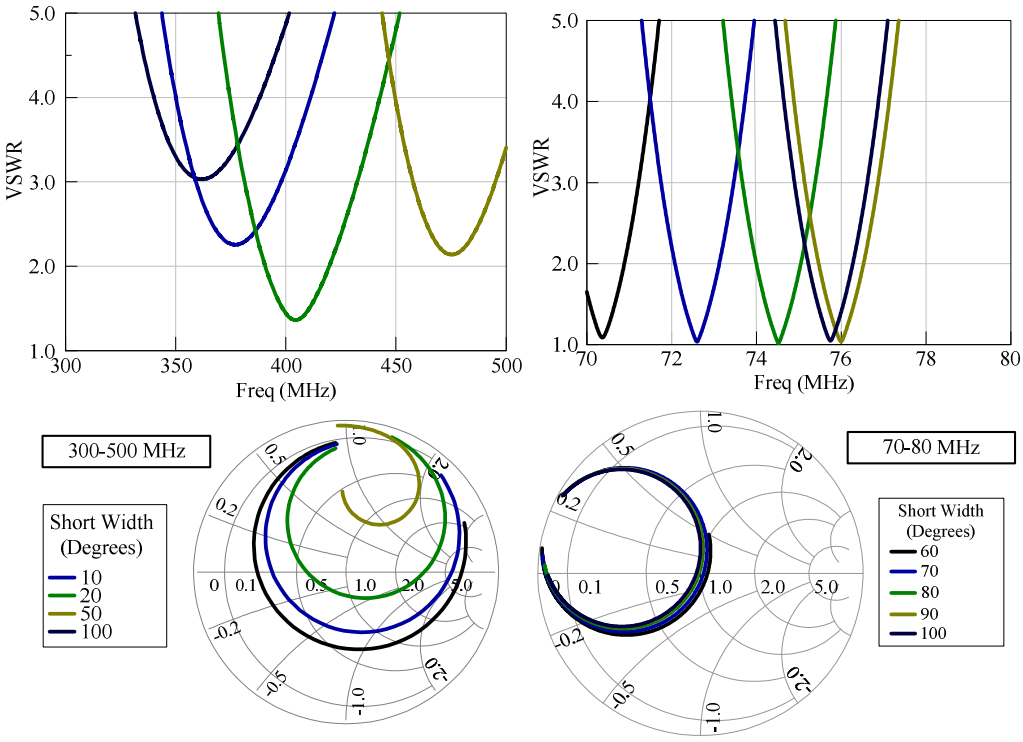

Fig. 21. Variation of the short width for coated and uncoated SIFAs

The variations on θ_s are shown in Fig. 22. Variations in this parameter lead the coated design to minor shifts in resonant frequency and no impedance mismatches. In the uncoated case, minor shifts in resonant frequency are also achieved, but a slight amount of impedance detuning is encountered.

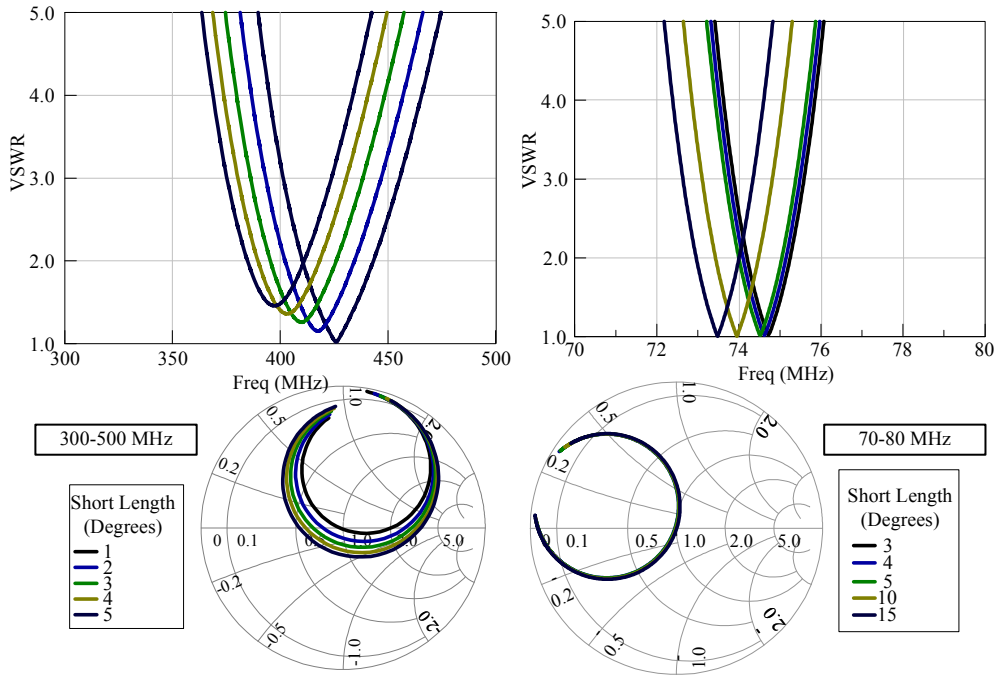

Fig. 22. Variation of the short length for coated and uncoated SIFAs

The variations in θ_g are shown in Fig. 23. For the coated design, this parameter can be used for significant shifts in frequency with very little change in the impedance match. This makes sense because the gap angle is related to the length of the resonant patch. For the uncoated design, frequency shifting is also achieved, but with slightly more change in impedance match.

The variations width ϕ_w are shown in Fig. 24. In both the coated and coated designs, variations in this parameter lead to minor shifts in resonant frequency accompanied by very little change in the impedance match. Overall, this is not a particularly sensitive parameter for design.

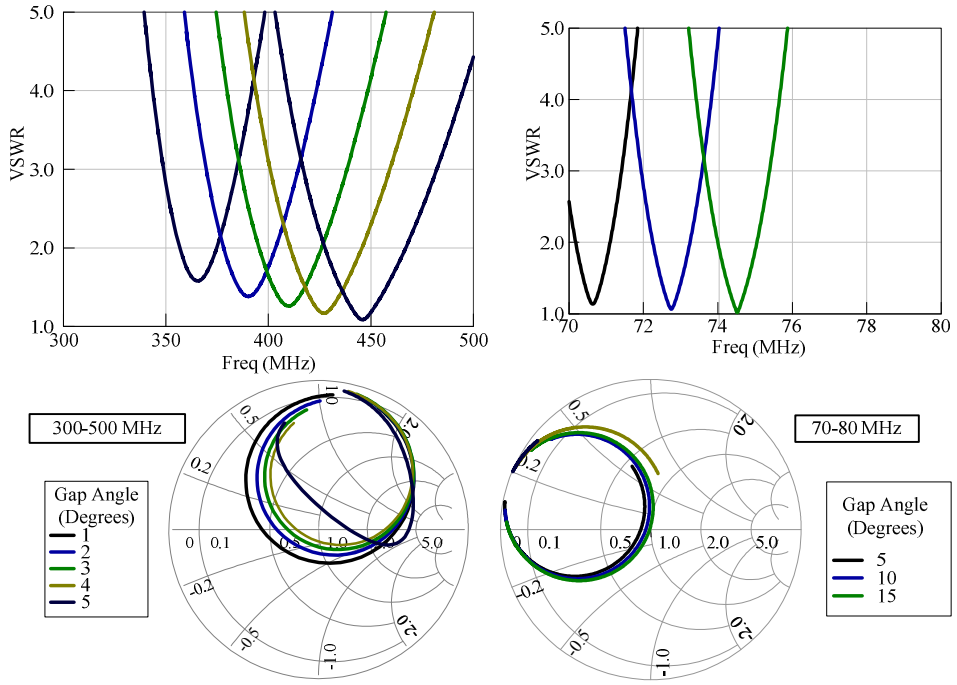

Fig. 23. Variation of the gap angle for coated and uncoated SIFAs

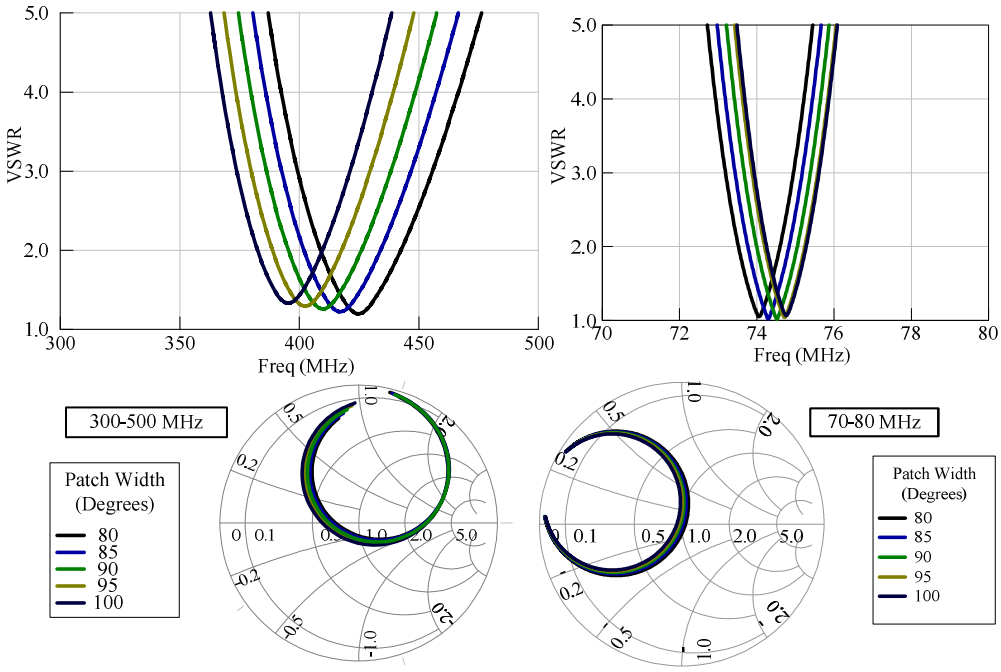

Fig. 24. Variation of the patch width for coated and uncoated SIFAs

Finally, the variations in R_i are shown in Fig. 25. In both the coated and uncoated designs, changes in this parameter result in significant changes in both resonant frequency and impedance match. This is expected, though, since changing the inner radius effectively changes the dimension of the resonant cavity.

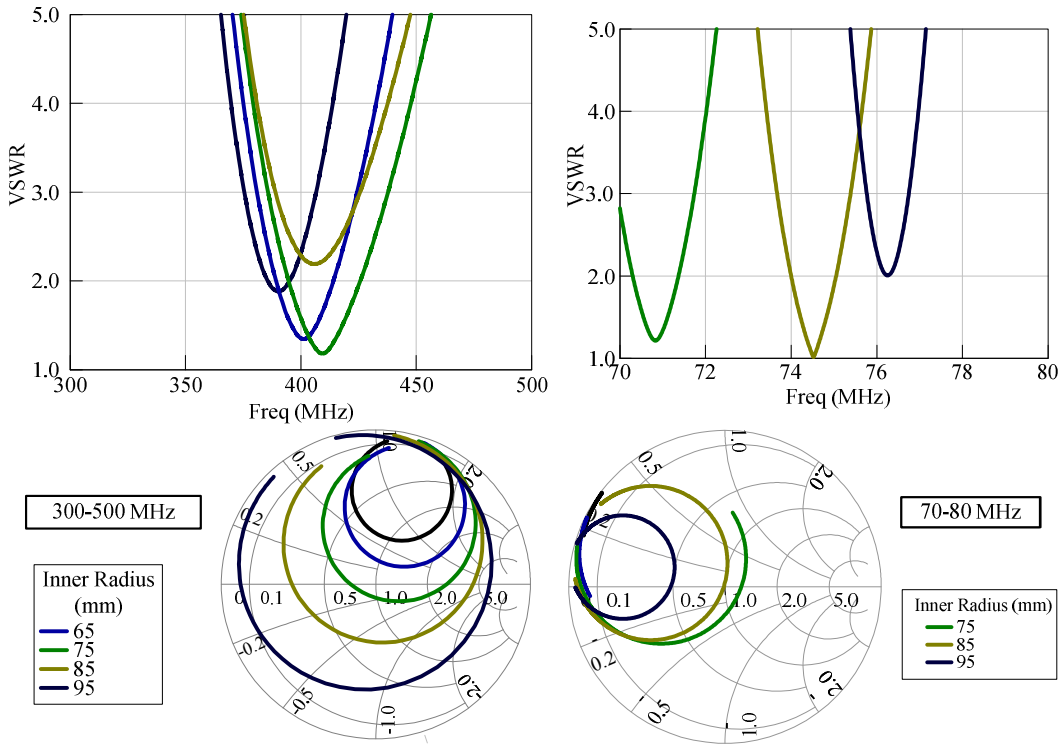

Fig. 25. Variation of the inner radius for coated and uncoated SIFAs

Overall, the parametric study demonstrated consistent trends in the effects of the SIFA dimensions on both the coated and uncoated designs, showing that the performance of the dielectric SIFA can be easily related back to the uncoated design. One significant difference, however, is that the coated SIFA provides several more useful design variables; specifically, changes in the feed angle and short width allow the

impedance and resonant frequency, respectively, to be modified relatively independently. This fact makes tuning a SIFA with a lossy coating somewhat easier than an uncoated design.

The final simulated design of a dielectric SIFA that will be mentioned here is the model on which a fabricated dielectric SIFA was based. The ground plane of this design has an outer radius of 2.5 inches (not including the coating); the coating is 1.25 inches thick. This design is slightly smaller than the 4-inch radius MICS band SIFA, but it operates at nearly the same frequency (around 400 MHz) because its coating and substrate have a dielectric constant of 7.5. The size of this design was chosen mostly due to the constraints of available fabrication materials. The primary interest in this design is its comparison value with the fabricated dielectric SIFA. Thus, the details of this design are discussed in the fabrication section later.

C. Coating Materials

In order to demonstrate the concept of a dielectric coated SIFA completely, a simple version was fabricated. Due to a lack of specialized equipment, this prototype fabrication had to be performed by hand; this presented a number of practical challenges in the fabrication process that limited the flexibility of the design. Nonetheless, a basic coated design could be realized.

The first decision pertaining to a fabricated coated SIFA was the material choice for the coating. For this work, two different materials were chosen as immediate possibilities for the coating: silicone rubber [35] and rigid polyurethane foam. These

materials were readily available commercially from a mold-making and casting company. These materials are intended to be used for mostly artistic casting purposes, but they can be easily used to cast the spherical shell and substrate necessary for the dielectric SIFA. Each material comes in a two-part liquid form (dubbed Part A and Part B); these liquid components for the silicone rubber are shown in their containers in Fig. 26. The two parts of the liquid are poured together into a mold in the correct proportion and allowed to cure into a solid.

Fig. 26. Silicone rubber used for dielectric SIFA fabrication

The rubber and rigid foam are good candidates for the SIFA coating because they are very amenable to the hand fabrication process due to the ease with which they can be used to cast arbitrary shapes; this is the primary reason for choosing them. The rigid foam, in particular, is an intriguing possibility. It is extremely strong and very lightweight; it could provide a structurally rigid "shell" for the SIFA which could protect the patch antenna inside from harsh outside environments. The silicone is much heavier and softer; it may not be ideal for real applications, but it at least provides a fabrication

material for a prototype dielectric SIFA. In fact, for fabrication purposes, the silicone rubber proved to be easier to handle than the rigid foam. It is much easier to release from molds than the foam once it has cured, primarily because it is soft and flexible. The rubber also does not expand when it cures from a liquid into a solid; the foam does expand to several times its initial volume, making filling a mold homogenously with the material more troublesome. For these reasons, the silicone rubber was chosen over the rigid polyurethane foam for purposes of fabricating the first dielectric coated SIFA. However, the foam remains a possible candidate for future designs.

Although the silicone rubber provides a good casting material for making the SIFA coating, it only has fixed dielectric properties. It was desirable to be able to make a wide range of dielectric materials for SIFA fabrication. Additionally, the rubber has only nominal dielectric loss; a lossy coating, then, as discussed previously, cannot be achieved by rubber alone. In order to obtain a variety of relative dielectric constants and loss tangents, another material needed to be added to the rubber; this second material was chosen to be carbon fiber. The carbon fiber can easily be mixed into the liquid Part A and Part B of the rubber before they are mixed for curing; it does not interfere with the curing process itself. Generally speaking, as more carbon fiber is added to the rubber, the dielectric constant and the loss tangent of the resultant material increase.

The idea of using carbon fiber as a lossy agent in silicone rubber was actually derived from a biomedical work in which this same combination of materials was used to achieve a wide range of dielectric properties in order to simulate the electromagnetic properties of various biological materials [36]. Another work actually used two different

types of carbon fiber dispersed in the rubber in varying proportions [37]. By varying the concentration of these two carbon fiber types, a wide range of both relative dielectric constants and loss tangents were achieved, as shown in Fig. 27. The same concept of varying carbon fiber concentration is used for the SIFA coating to obtain desired dielectric properties.

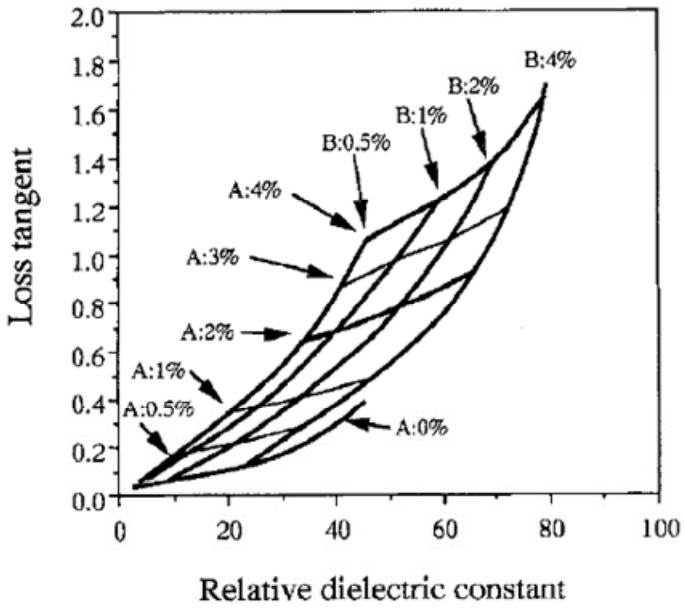

Fig. 27. Example of rubber-carbon-fiber dielectric properties. Various relative dielectric constants and loss tangents are achieved by mixing two types of carbon fiber in silicone rubber (from [37])

For simplicity, only one type of carbon fiber was used to make the material for the dielectric SIFA. This severely limited the diversity of material properties as would have been possible with a second type of carbon fiber, since an increase in the single type of fiber would unilaterally result in an increase in both dielectric constant and loss tangent. These two dielectric properties could not be modified independently.

Nonetheless, the basic silicone rubber could be transformed into a lossy coating by adding the carbon fiber.

When making this rubber-carbon-fiber mixture, Parts A and B of the silicone rubber were used in equal volumes. Before mixing these two liquid parts, the desired amount of carbon fiber was mixed into part A, which is the less viscous of the two liquids; the mixture is made as homogeneous as possible. Then, the two liquids are mixed together to cure into the rubber-carbon-fiber mixture.

D. Dielectric Characterization

A method was needed to characterize the electromagnetic properties of the rubber-carbon-fiber mixture: namely, the relative dielectric constant ε_r and the dielectric loss tangent $\tan\delta$. The only immediately available dielectric measurement tool was a coaxial probe system designed for use with liquids; this proved difficult to apply to the solid rubber mixture with any repeatable results. For the purposes of this work, only an approximately accurate material characterization was required. The fabrication would only be a first-pass prototype, so extreme accuracy was not needed. Thus, it was not necessary to take the time to build or acquire the services of a legitimate measurement system for solids; instead, an simple approach using a network analyzer, a coaxial probe connector, and simulations was employed to achieve a reasonable material characterization.

The methodology for this material characterization was to use the network analyzer to take S_{11} reflection measurements of a sample piece of rubber mixture by

pressing the coaxial probe connector flush against the surface of the material. This sample piece of rubber was cut into the shape of a rectangular prism. Then, the material and the coaxial probe were simulated together (in exact dimensions) with the dielectric properties (both relative dielectric constant and loss tangent) of the material being varied in a parametric sweep. Finally, the measured magnitude and phase of S_{11} were matched to the closest magnitude and phase from the simulation variations in order to pinpoint the dielectric properties. Specifically, the measured phase of S_{11} was matched first against simulated phase curves for zero loss and varying dielectric. This allowed the relative dielectric constant to be determined because the phase curves were essentially independent of the loss tangent. The magnitude of S_{11} was then fitted (in a least-squares sense) to simulated magnitude curves in which the dielectric constant was kept constant and the loss tangent was varied; this allowed the loss tangent of the material to be determined.

Fig. 28 shows the simulation used in this material characterization process. The rectangular shape of the test material allowed easy construction for the simulation. Fig. 29 shows the simulated S_{11} phase curves versus frequency for relative dielectric constants ranging from 10 to 50 in steps of 10 (a relative dielectric constant of 1 is also included); the loss tangent for these simulations is simply set to zero since the curves are independent of the dielectric loss. Note that increasing the dielectric constant makes the slope of the curves become steeper; in fact, it is the slope that needs to be matched to the simulated results to find the correct dielectric constant. Fig. 30 shows the simulated S_{11} magnitude curves that were obtained while sweeping the loss tangent from 0 to 1.0 in

steps of 0.2. The relative dielectric constant was assumed to be approximately 7.5 and was kept constant for each variation of the loss tangent. Again, as for the phase curves, increasing the loss tangent increases the slope of these magnitude curves; the slope can be matched to that of the measured S_{11} magnitude. It should be noted that these magnitude curves are only valid for one value of dielectric constant; they will change as the dielectric constant changes.

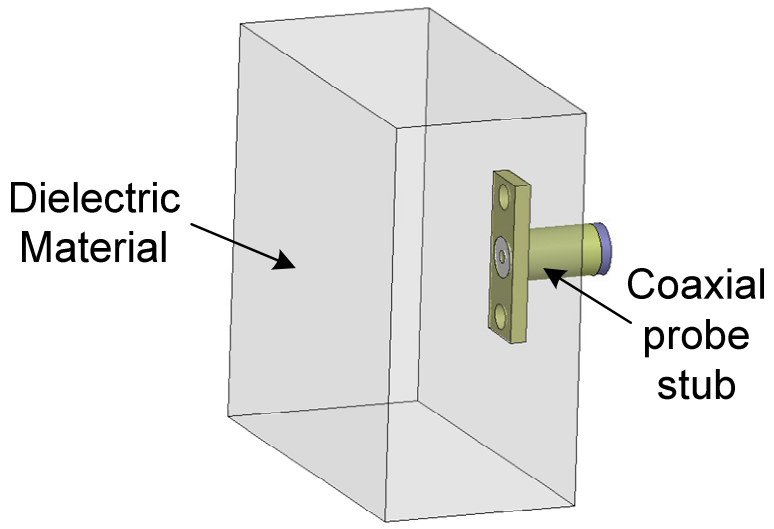

Fig. 28. Simulation of dielectric characterization

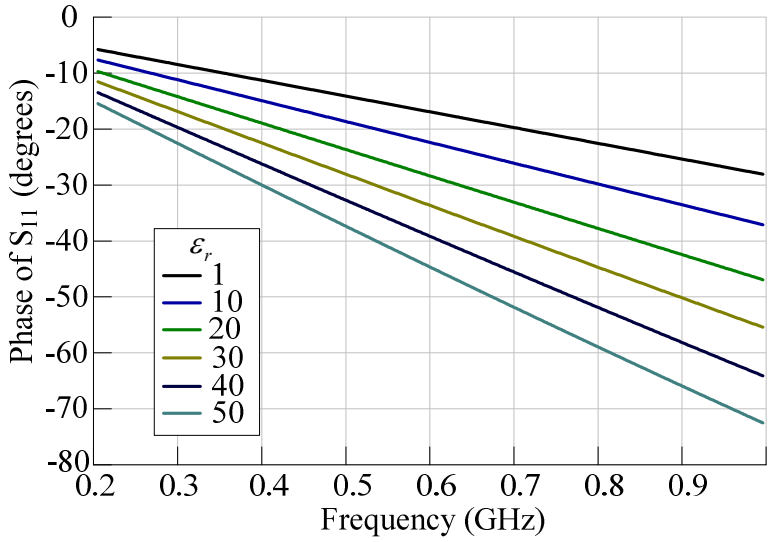

Fig. 29. Simulated S_{11} phase curves for dielectric characterization. The loss tangent is assumed to be zero, although the phase curves should be independent of it. Measured phase of S_{11} was matched to the closest curve to approximate the relative dielectric constant

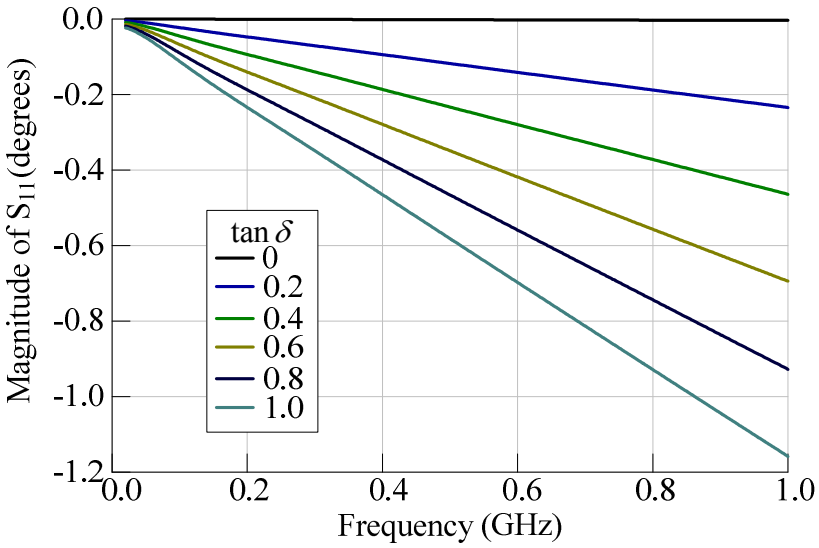

Fig. 30. Simulated S_{11} magnitude curves for dielectric characterization. Relative dielectric constant is assumed to be 7.5. For a fixed relative dielectric constant, the measured magnitude of S_{11} was matched to the closest curve to approximate the dielectric loss

A number of different rubber-carbon-fiber mixtures were subjected to this probe measurement technique to get a feel for how the carbon fiber concentration impacted the dielectric properties of the rubber. The results from all of these different test mixtures will not be enumerated here; only the pure rubber (i.e. no carbon fiber) and the particular mixture used for fabricating a coated SIFA are of significant interest here. The amount of carbon fiber to disperse in the rubber was a somewhat arbitrary choice; no particular combination of dielectric properties was set as a "goal". In the end, the amount of dispersed fiber was somewhat limited by rubber: as more fiber was added, the mixture eventually became too viscous to ensure proper homogeneous mixing. The final dispersion ratio that was used for the fabricated coated SIFA design was 1 gram of carbon fiber per 10 mL of rubber (Parts A and B combined in liquid form); this provided a easy ratio for measurement and mixing purposes and also achieved a relatively large concentration of carbon fiber so as not to make the mixture too viscous.

The final rubber-carbon-fiber mixture was subjected to dielectric characterization by measuring a block of it with a coaxial probe connected to a network analyzer. The magnitude and phase of S_{11} was measured. First, the phase was compared to the simulated phase curves in Fig. 29. Matching the measured phase curve to a simulated curve was fairly successful using a least-squares approach; a dielectric constant of $\varepsilon_r = 7.5$ was estimated (note that, although Fig. 28 only shows curves for six relative dielectric constants, the simulation actually had curves for dielectric constants ranging from 1 to 50 in steps of 0.1 in order to achieve a decent level of precision). Next, the magnitude of S_{11} was simulated with the relative dielectric constant fixed at 7.5 (as

shown in Fig. 30). The measured magnitude curve was compared to this simulation, but, unfortunately, the measured results were not good enough to match to any simulated curve. There appeared to be too much noise in the magnitude measurement. Thus, not even a decent approximation to the dielectric loss could be found. However, it was decided that the fabrication would proceed anyway, and the dielectric loss could be estimated after fabrication by comparing the bandwidth to simulated versions of the fabricated SIFA (a larger loss tangent would result in a wider bandwidth).

The dielectric characterization method outlined above should yield fairly accurate results since it is a deterministic system. The simulation is straightforward and should also be very accurate, so matching the measured results to it should be fairly reliable. However, a number of practical issues limit the accuracy of the method. Generally speaking, it is difficult to achieve a clean contact between the coaxial probe and the rubber. Specifically, cutting the rubber into the desired rectangular shape leaves the surface somewhat irregular, as opposed to the ideally smooth surface in the simulation. Also, since the rubber is soft and flexible, the probe can be pressed against the rubber with a variable amount of pressure; it is difficult to say what amount of pressure corresponds most closely to the idealized conditions in the simulations. Finally, it is difficult to achieve a perfectly rectangular shape of rubber with the hand cutting tools that are available; this introduces a measure of geometric inaccuracy into the situation as compared to the simulation. Overall, this dielectric characterization method can only be viewed as a reasonable first-pass method. It is acceptable for this work because extremely accurate dielectric measurements are not the focus, whereas a

fabricated dielectric SIFA is. Only reasonable knowledge of the dielectric properties of the rubber-carbon-fiber mixture is necessary to construct a working prototype of the coated antenna. Future fabrications, of course, could rely on more accurate dielectric characterizations.

E. Dielectric SIFA Fabrication Process

Characterization of the material properties of the rubber-carbon-fiber mixture allowed a simple prototype of a dielectric SIFA to be fabricated. For purposes of comparison, both an uncoated design and a coated design with the same ground plane radii were fabricated. The size and operating characteristics of the antenna were fairly limited by the available fabrication materials and methodology, as well as the dielectric properties determined from the material characterization. More specifically, hemispherical aluminum molds (typically used for baking purposes) were used in the fabrication for casting of the rubber; these molds were only available in certain sizes, thereby limiting possibilities for the physical size of the designs. The dimensions of the chosen designs (both coated and uncoated) are listed in Table 2. The radii of the ground plane for these designs are 37.5% smaller than the original fabricated uncoated SIFA. The uncoated design is designed to operate at about 1 GHz, higher than the original SIFA fabrication. The coated design, due to the high dielectric substrate and coating, operates near the original SIFA at around 400 MHz; thus, this design represents uses the coating as an agent of physical miniaturization. Both designs were simulated in for comparison later with the fabricated versions.

Table 2. Dimensions of fabricated SIFAs. Both the coated and uncoated are included

Design Variable	Description	Value (Uncoated Design)	Value (Coated Design)
R_i	Inner radius	49.2 mm	49.2 mm
R_o	Outer radius	60.3 mm	60.3 mm
ϕ_w	Patch width	90°	90°
ϕ_s	Short width	24°	34°
θ_f	Feed angle	12°	3°
θ_s	Short length	13°	34°
θ_g	Gap width	12°	12°
r_c	Coat thickness	Not applicable	19 mm

The ground planes of these new antennas were fabricated in the same manner as the original SIFA: using two spherical foam balls corresponding to the inner and outer radius (specifically, 4-inch and 5-inch diameter balls, respectively), with copper tape attached to the outside and tacked with solder to insure electric continuity. Since the inside of the SIFA's ground plane is electromagnetically isolated from the rest of the antenna, the choice of foam for this part of the structure did not interfere with the rest of the design at all. Once these ground planes were constructed, the coaxial feed structure was constructed. To do this, the semi-rigid coaxial probe was pushed through the foam of the ground plane from the backside and out of middle of the substrate area (in an identical fashion to what was performed in original uncoated SIFA fabrication). The portion of the probe emerging in the substrate area was stripped down to the inner conductor to make the probe feed for the patch, and the outer conductor was soldered to the ground plane. It should be noted that the insertion of this coaxial probe through the ground plane was one of the more inaccurate aspects of the hand fabrication process,

since the exact angle of the feed probe is very important to the antenna impedance; this point will be discussed further along with the measured results from the fabrication. After the feed structure was complete, the fabrication proceeded differently for the coated and uncoated designs: the uncoated design was finished in the same manner as the original SIFA fabrication, so the details will not be repeated here; the coated SIFA was continued with the rubber-carbon-fiber portion of the design.

To make the substrate for the patch, an appropriate amount of the rubber-carbon-fiber mixture was poured into a hemispherical mold fitting the outside of the ground plane exactly. The rubber was allowed to dry, and the whole ground plane was released from the mold, with the substrate attached. The resulting rubber substrate, in the shape of a quarter-spherical shell, was matched to the ground plane in size and shape.

Next, the patch had to be constructed on the surface of the rubber substrate; this was done using copper tape, as in the original uncoated SIFA fabrication. The only complication was that the tape did not adhere well to the cured rubber surface. However, this was remedied by making a small additional amount of rubber-carbon-fiber mixture; spreading a thin layer of it on the substrate surface with a paintbrush; placing the copper tape on top of the new liquid layer; and allowing the thin layer to cure. After the rubber was allowed to cure while in contact with the tape, the adherence of the tape was acceptable. Fig. 31 shows a picture of the dielectric SIFA up to this stage in the fabrication process, without a coating.

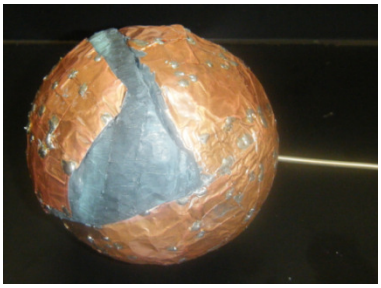

Fig. 31. Fabricated dielectric SIFA without its coating. The dielectric substrate is visible

The final stage of the dielectric SIFA fabrication process was to make the outer coating itself. This was done by making two hemispherical sections of the coating, placing these around the ground plane, and fusing them together. Each hemisphere of the coating was created by pouring rubber into an 8-inch diameter hemispherical aluminum mold; placing a hemisphere the same size as the ground plane into the liquid mixture in the mold, making sure it is centered relative to the mold; and allowing the rubber mixture to cure. After curing, the rubber was released from the mold as a hemispherical shell with a thickness just over one inch. Once two such hemispherical shells were created, they were placed over the SIFA from opposite ends (one shell needed to have the coaxial probe stuck through it). For measurement purposes, these two halves of the SIFA were held together by tying them tightly with strings; this provided enough of a seal to perform measurements. Theoretically, these two hemispheres of the coating could be sealed together permanently by using a paintbrush to spread a small amount of additional liquid rubber-carbon-fiber mixture along the seam between the two halves. After curing, the rubber of the two hemispheres would be fused together.

The coated and uncoated SIFA fabrications are shown in Fig. 32. The original MICS band uncoated design is also shown in the picture for comparison. Fig. 33 shows three detail views of the new fabrications: a side profile of the dielectric SIFA with its coating removed; a side profile of the new uncoated design; and a view of the dielectric SIFA with one hemisphere of coating removed.

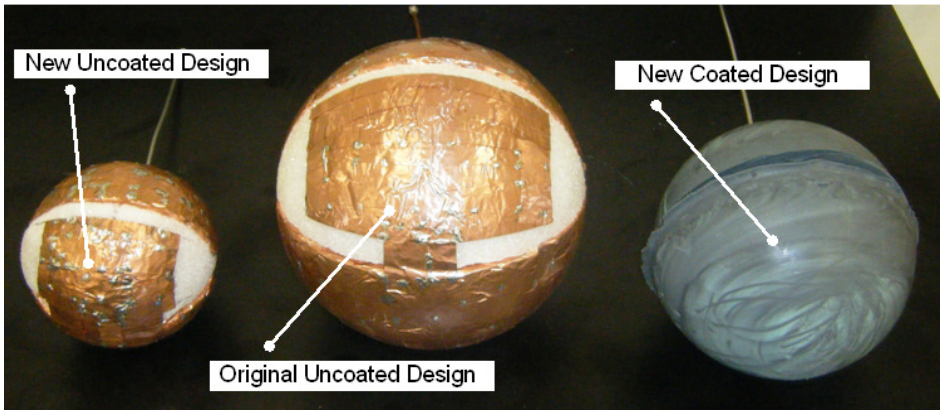

Fig. 32. Fabricated SIFAs. Shown are the new uncoated design (left), the new coated design (right), and the original MICS band SIFA (middle)

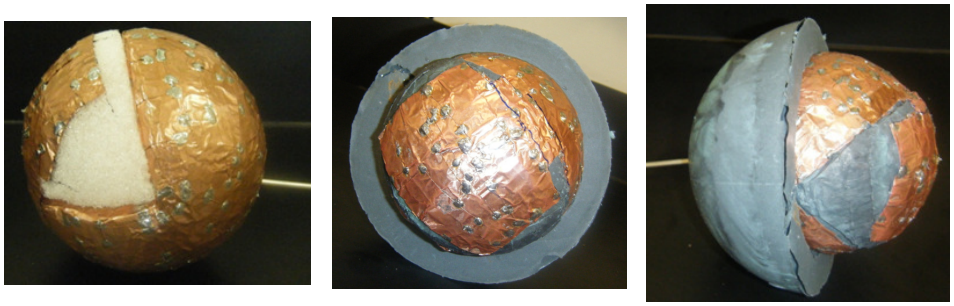

Fig. 33. Detail views of fabricated SIFAs. On the left is a side profile of the new uncoated SIFA. On the right and in the middle are two views of the new dielectric SIFA with one hemisphere of its coating removed

F. Dielectric SIFA Fabrication Results

After fabrication, the input impedances of the coated and uncoated SIFA fabrications were measured on a network analyzer. Fig. 34 shows the measured VSWR for both antennas, along with the corresponding simulated curves. The figure also shows the simulated and measured impedance loci on a Smith chart. The results show a general correspondence between the predicted performance of the simulations and the measured data. It is immediately evident that a reasonably functioning dielectric SIFA was successfully fabricated.

There are a few issues with the measured results that should be addressed. First, the agreement between the measured and expected VSWR curves is not as good as for the original fabricated SIFA (which were within 5% of the simulated results). There are several possible explanations for this. First, for the new uncoated design, the electrical size of this antenna was larger than the original fabricated SIFA. The new uncoated design had a diameter of 0.423λ, while the original SIFA had a diameter of 0.273λ. The significance of these sizes is that for the electrically larger new uncoated SIFA, slight inaccuracies in the fabricated geometry (which are unavoidable with the hand fabrication process) would have a more profound effect on the antenna performance, since they are larger relative to the operating wavelength. Thus, the original SIFA was more "forgiving" as far as hand fabrication tolerances were concerned, and achieving an accurate resonant response was more difficult for the new uncoated design; this was borne out by the fact that the new fabrication resonated at a lower frequency than predicted. This problem was compounded by the smaller physical size of the new

antenna; using the same fabrication materials and technique, small irregularities in the fabrication were larger relative to the overall geometry than they were in the original design, leading to less accurate results.

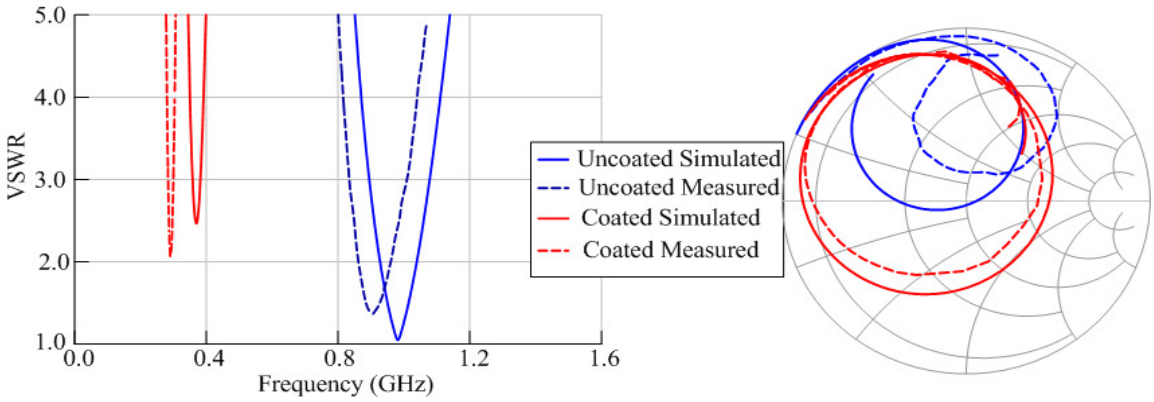

Fig. 34. Measured and simulated data for fabricated SIFAs. On the left is a VSWR plot, and on the right is the input impedance loci on a Smith chart

Electrical size was not a factor in fabrication inaccuracy for the coated design since its diameter was 0.212λ, only slightly less than the original SIFA. However, since the ground plane and patch size were the same as the new uncoated design, the smaller physical size of the coated design compared to the original SIFA could certainly have added inaccuracies. But perhaps the most important factor affecting the coated design's performance was the uncertainties about the dielectric properties of the rubber-carbon-fiber mixture. As detailed earlier, only a rough characterization process was employed for this material, and the results were never expected to be entirely accurate. The fact that the measured 2:1 bandwidth of the fabricated coated SIFA had at least a small overlap with the simulated bandwidth showed that the dielectric characterization was at

least a decent approximation to the true material properties of the carbon-fiber-laden rubber. Overall, this prototype was a good first pass at fabrication of the coated SIFA.

Another point of interest is the dielectric characterization of the fabricated dielectric SIFA – specifically, the characterization of the dielectric loss. As mentioned before, the dielectric characterization failed to provide a meaningful value for the loss tangent. However, after simulating the fabricated dielectric SIFA with different loss tangent values, a reasonable value was found: 0.04. This was estimated by roughly matching the bandwidth of the simulated design (i.e. the width of the VSWR curve) to the bandwidth from the measurements. Although not desirable, this method at least provided an estimate of the dielectric loss that could not otherwise be obtained. In the end, this first fabrication of a dielectric SIFA was estimated to have dielectric properties of $\varepsilon_r = 7.5$ and $\tan\delta = 0.04$. In future work, it would certainly be desirable to have better methods for characterizing the dielectric properties of the coating.

Generally speaking, the fabrication of a new smaller uncoated SIFA, along with a coated design of the same ground plane size, was a success in that it offered a proof of concept for the coated SIFA. A simple hand fabrication yielded decent first results. Certainly, the combination of better fabrication methods (and materials), along with more accurate dielectric material measurements, would drastically improve the accuracy of fabricated designs in future work.

CHAPTER V

SIFA CAVITY MODEL

A. Previous Model: Transmission Line Model

The SIFA has previously been modeled analytically by a transmission line model. This model is modified from the corresponding transmission line model for a PIFA, which is well documented. The SIFA model is identical to the planar model, with the linear distances of the PIFA patch replaced by the arc lengths of the patch geometry on the SIFA's spherical surface.

The structure of the transmission line model is shown in Fig. 35. The coaxial feed point is considered to be the input for the model. The patch is modeled as two parallel microstrip transmission lines originating at the feed, running along the length of the patch in either direction away from the feed. The characteristic impedance of these lines, Z_p, is determined using equations for a planar microstrip line, with an approximate height $h = R_o - R_i$ and width $w_p = R_o \phi_p$. One of these microstrip lines is terminated in a complex admittance representing primary radiating slot. The other line has a third microstrip line in series after it with Z_s based on $h = R_o - R_i$ and $w_s = R_o \phi_s$; this is the shorting strip connecting the main patch to the ground plane and body of the SIFA. The final component to the model is a shunt conductance, G_{ss}, which represents the radiation conductance of the two side slots; it is found across the input to the model.

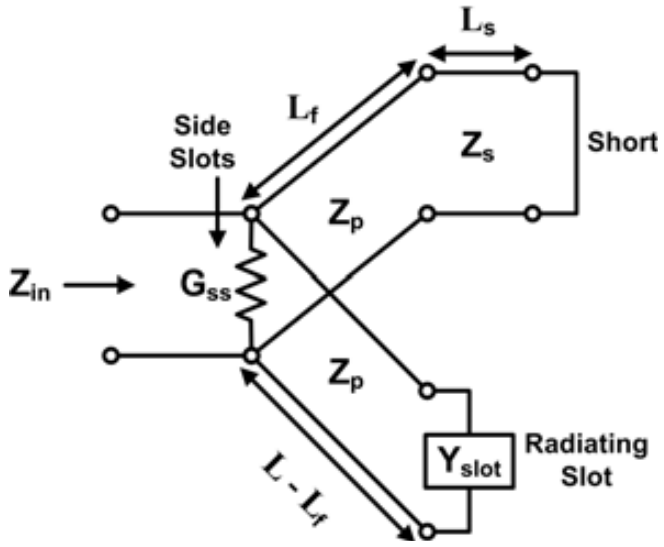

Fig. 35. Transmission line model of the SIFA. This model is identical to that used for the PIFA

The transmission line model approximates the SIFA patch as a PIFA with linear lengths equivalent to the arc lengths of the SIFA patch. It makes no special consideration for the spherical geometry of the SIFA. As such, it only provides a first-order approximation to the performance. Fig. 36 shows the VSWR curve and Smith Chart impedance curve for both the transmission line model and the simulation of the original MICS band SIFA.

The transmission line model is clearly only a rough approximation. For this reason, it is desirable to develop a more rigorous analytical model that incorporates more appropriately the unique geometry of the SIFA. In this work, the chosen technique for this task was the cavity method, which is widely used in planar microstrip antenna designs. Before proceeding directly to analysis of the SIFA under the cavity method, the

cavity model as applied to the PIFA is first introduced and discussed in detail. This will help to lay the foundation for the application of the same techniques to the SIFA.

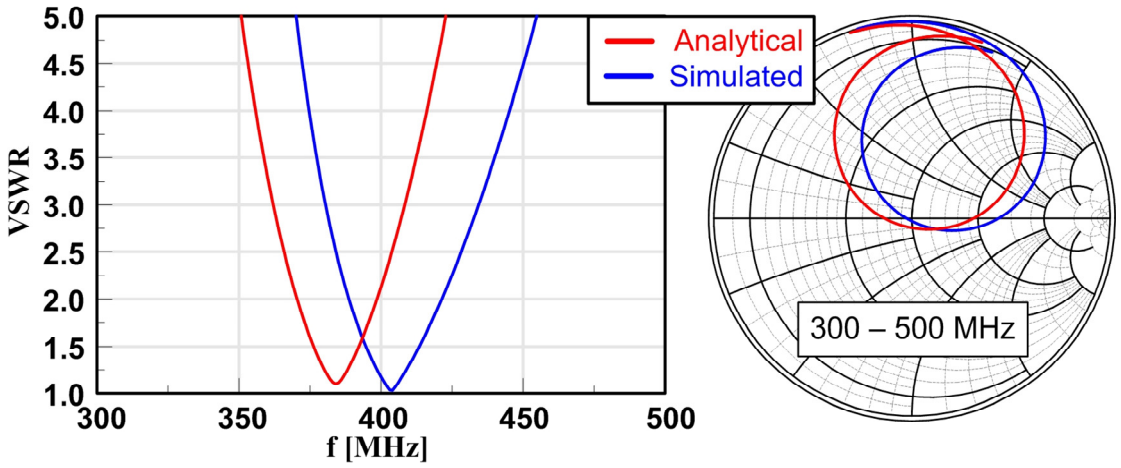

Fig. 36. Results from the transmission line model. Shown are the VSWR and Smith Chart plots of the TL (analytical) and simulated models of the MICS band SIFA. Results are shown over a frequency range of 300-500 MHz

B. PIFA Cavity Model

Before introducing the cavity model specific to the SIFA, it is necessary to briefly explain how the cavity model is developed for a standard rectangular PIFA. In planar patch designs, the cavity model is very accurate way of predicting performance. The basics of the cavity model were briefly discussed in the background section with regards to microstrip patch antennas. Now, a full treatment of the cavity model for the PIFA will be provided, consisting of a three-dimensional analysis of the electromagnetic fields in the "cavity" between the patch surface and the ground plane. This cavity is in the mathematically friendly shape of a rectangular prism.

A standard rectangular cavity for a PIFA is shown in Fig. 37. It has a height h, length l, and width w. The top and bottom of the cavity are the patch surface and the ground plane, respectively, and are modeled as PEC surfaces, or electrical walls. Also, the vertical shorting wall, the defining feature of the PIFA, is considered to be a PEC surface at $x = l$. The three remaining walls of the cavity are not physical barriers, but rather "imaginary" walls that are approximated as PMC surfaces (i.e., magnetic walls). This approximation is appropriate given several assumptions: the height h is assumed to be relatively small compared to the wavelength ($h \ll \lambda$); the electric field will be approximately constant in the vertical direction (z direction); and only a small portion of the fields extend outside of the area directly beneath the patch (i.e. only small fringing fields exist there). As long as h is sufficiently small, this assumption is relatively accurate and allows the magnetic walls to be constructed around the outside of the cavity without losing too much accuracy.

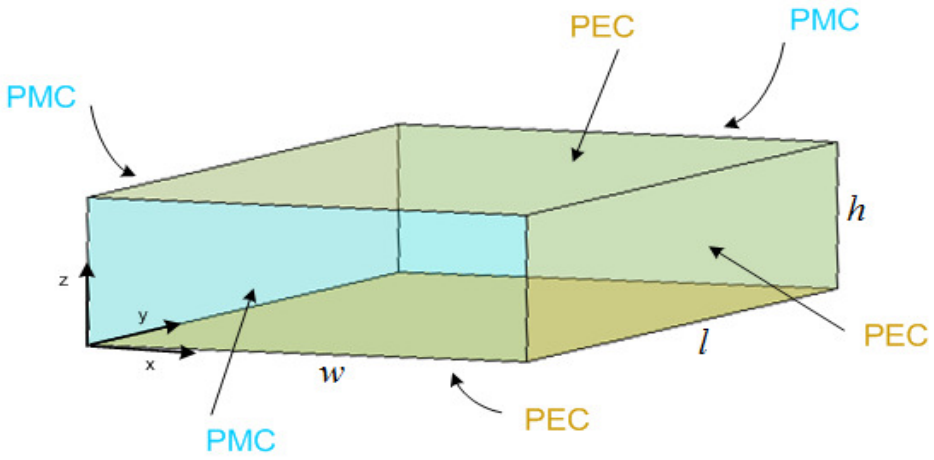

Fig. 37. Cavity model of the PIFA. The metallic surfaces (top, bottom, and $x = l$) are shown in yellow and are PEC surfaces. The remaining surfaces are PMC

Since the PIFA is a radiating structure, the cavity must account for the loss of power due to this radiation. To do this, it is modeled as a leaky cavity; otherwise, it would simply be a lossless rectangular resonator. Specifically, radiation is assumed to emanate from the three PMC walls due to magnetic surface currents on them. These radiating walls are dubbed "slots". The magnetic wall directly opposite the shorting wall is considered to be the primary radiating slot, since it produces most of the radiation; the other two magnetic walls are called "side slots".

Development of the cavity model begins by writing the wave equation for the cavity and solving it subject to the boundary conditions. The general expression for the complex scalar wave equation, or Helmholtz equation, given in (7), is applicable to any homogenous region (ψ is a scalar "wave potential" that is related to the magnetic vector potential $\vec{A}$ or electric vector potential $\vec{F}$)

$$\nabla^2\psi + k^2\psi = 0 \tag{7}$$

Based on the assumptions that were made for the PIFA cavity, most of the electric field will be vertically oriented between the ground plane and the patch (i.e. z-directed), so the vertical magnetic field (H_z) will also be zero. This type of field structure is known as transverse magnetic – specifically, transverse magnetic to the vertical z direction, or TM_z. The TM_z field assumption, which is common in the cavity method, allows the magnetic vector potential to be written in terms of the wave potential (8). In other words, $\vec{A}$ only has a z-directed component, which is related to ψ.

$$\vec{A} = A_z\hat{a}_z = \psi\hat{a}_z \tag{8}$$

At this point, a brief aside about $\vec{A}$ and $\vec{F}$ is appropriate. These two vector potentials have little physical meaning, but they are immensely useful mathematically and arise directly from electric and magnetic sources in the region of interest. Specifically, electric sources ($\vec{J}$) give rise to a magnetic vector potential (9). Similarly, magnetic sources ($\vec{M}$) give rise to an electric vector potential (10).

$$\vec{A}(\vec{r}) = \frac{1}{4\pi}\iiint \frac{\vec{J}(\vec{r}')e^{-jk|\vec{r}-\vec{r}'|}}{|\vec{r}-\vec{r}'|}dV' \tag{9}$$

$$\vec{F}(\vec{r}) = \frac{1}{4\pi}\iiint \frac{\vec{M}(\vec{r}')e^{-jk|\vec{r}-\vec{r}'|}}{|\vec{r}-\vec{r}'|}dV' \tag{10}$$

In these integrals, $\vec{r}'$ represents a position vector from the origin to a point in the source region, V' is the volume containing the source region, and $\vec{r}$ is a position vector from the origin to any point in the desired field region. Thus, the volume integral is carried out over the source region, resulting in a vector potential that is a function of position $\vec{r}$. In the case of the PIFA cavity, the vector potential inside the cavity is caused by whatever feed mechanism the antenna uses; this could be a microstrip feed, a coaxial line, etc.

The electric and magnetic vector potentials are extremely useful for two reasons. First, they provide a natural separation of a problem into those fields caused by electric sources and those caused by magnetic sources. Secondly, and even more importantly, is that once the vector potentials are calculated, the electric and magnetic fields can be computed in closed form. These fields are obtained from (11) and (12) along with the

TM_z field assumption. The specific components of the fields in Cartesian coordinates are given by (13)-(18).

$$\vec{E} = -\nabla \times \vec{F} + \frac{1}{j\omega\varepsilon}\nabla \times \nabla \times \vec{A} \tag{11}$$

$$\vec{H} = \nabla \times \vec{A} + \frac{1}{j\omega\mu}\nabla \times \nabla \times \vec{F} \tag{12}$$

$$E_x = \frac{j}{\omega\mu\varepsilon}\frac{\partial^2 \psi}{\partial z \partial x} \tag{13}$$

$$E_y = \frac{j}{\omega\mu\varepsilon}\frac{\partial^2 \psi}{\partial z \partial y} \tag{14}$$

$$E_z = \frac{j}{\omega\mu\varepsilon}\left(\frac{\partial^2}{\partial z^2} + k^2\right)\psi \tag{15}$$

$$H_x = \frac{\partial \psi}{\partial y} \tag{16}$$

$$H_y = -\frac{\partial \psi}{\partial x} \tag{17}$$

$$H_z = 0 \tag{18}$$

With the details regarding the vector potentials clear, the wave equation must be solved. Expanded into its Cartesian form, the wave equation appears as:

$$\frac{\partial^2 \psi}{\partial x^2} + \frac{\partial^2 \psi}{\partial y^2} + \frac{\partial^2 \psi}{\partial z^2} + k^2\psi = 0 \tag{19}$$

This is a separable partial differential equation, meaning that its solution can be written as:

$$\psi = A(x)B(y)C(z) \tag{20}$$

The three differential equations associated with this solution are:

$$\frac{1}{A}\frac{\partial^2 A}{\partial x^2} = -k_x{}^2 \tag{21}$$

$$\frac{1}{B}\frac{\partial^2 B}{\partial y^2} = -k_y{}^2 \tag{22}$$

$$\frac{1}{C}\frac{\partial^2 C}{\partial z^2} = -k_z{}^2 \tag{23}$$

Here, the wavenumber k is given by:

$$k = \sqrt{k_x{}^2 + k_y{}^2 + k_z{}^2} \tag{24}$$

Clearly, (21) - (23) are simple harmonic equations with sinusoidal solutions.

The specific solutions to these equations can be ascertained by looking simultaneously at the PEC and PMC boundary conditions previously discussed for the PIFA and the field equations (13) - (18). On the ground plane and patch surface ($z = 0$ and $z = h$, respectively), the tangential electric fields, E_x and E_y, must be zero; in order to satisfy (13) and (14), $\partial\psi / \partial z$ must be zero, so:

$$C(z) = \cos\left(\frac{m\pi z}{h}\right), \quad k_z = \frac{m\pi}{h}, \quad m = 0,1,2,\ldots \tag{25}$$

The tangential magnetic field H_x must be zero on the magnetic walls at $y = 0$ and $y = w$ to satisfy (16). This means that $\partial\psi / \partial y$ must be zero and:

$$B(y) = \cos\left(\frac{n\pi y}{w}\right), \quad k_y = \frac{n\pi}{w}, \quad n = 0,1,2,\ldots \tag{26}$$

The z-directed solution is the most challenging; the tangential magnetic field (H_y) must go to zero on the magnetic wall at $x=0$, but the tangential electric fields (E_y and E_z) must go to zero on the electric wall at $x=l$. These conditions can be satisfied by the solution in (27) with odd (or quarter-wave) index p:

$$A(x)=\cos\left(\frac{p\pi x}{2l}\right),\quad k_x=\frac{p\pi}{2l},\quad p=1,3,5,\ldots \tag{27}$$

The total solution, then, can be written as:

$$\psi_{mnp}=A_{mnp}\cos\left(\frac{m\pi}{h}\right)\cos\left(\frac{n\pi}{w}\right)\cos\left(\frac{p\pi}{2l}\right) \tag{28}$$

Note that because of the integer indexes m, n, and p, only certain modal solutions can exist inside the cavity (hence the mnp subscript notation on ψ). Furthermore, since k_x, k_y, and k_z depend on m, n, and p, each mode has its own frequency of operation as governed by the wavenumber in equation (24). Each mode also has an associated scaling factor A_{mnp}. The modes that are present in the cavity depend on the particular excitation of the antenna. In general, many modes are excited in the cavity simultaneously with varying amplitudes; the total field in the cavity is simply the sum of all of the modal contributions. Mathematically, this summing of modes can be summarized as:

$$\psi_{total}=\sum_{m,n,p}A_{mnp}\psi_{mnp} \tag{29}$$

The mode with the lowest corresponding resonant frequency is called the dominant mode. Typically, this dominant mode is much stronger than the other modes. The antenna is generally designed to operate at the frequency of the dominant mode.

Once the total fields are determined in the cavity, a number of subsequent calculations can be performed to determine a number of desired antenna performance parameters. For brevity, only a few of these calculations will be summarized here. The first calculation that can be made is the radiated fields and radiated power from the antenna. As stated before, three "slots" in the PIFA cavity model contribute to radiation: a primary radiating slot at $x = 0$ and two side slots at $y = 0$ and $y = w$. The radiated power for each of the three slots is calculated separately and identically; then, the three contributions are added. First, the electric fields on the slot surfaces are converted into equivalent magnetic surface currents, as in (6):

$$\overrightarrow{M}_s = -2\hat{a}_n \times \vec{E} \tag{30}$$

These magnetic currents act as the radiating mechanisms, producing an electric vector potential per (10):

$$\vec{F} = \frac{\epsilon}{4\pi} \iint_{S'} \overrightarrow{M}_s \frac{e^{-jk\left|\vec{R}-\vec{R}'\right|}}{\left|\vec{R}-\vec{R}'\right|} dS' \tag{31}$$

Here, the volume integral has been reduced to a surface integral because the source region is simply the surface of the slot. Next, the far field electric field can be determined directly from $\vec{F}$ using equation (11) (note that here, $\vec{A}$ is zero):

$$\vec{E}_{far} = -\nabla \times \vec{F} \tag{32}$$

Finally, this field can be integrated over a sphere in the far field to find the total power flowing through the sphere (i.e. the total radiated power):

$$P_{rad} = \frac{1}{\eta} \iint_{4\Omega} \left(\left|E_\theta\right|^2 + \left|E_\phi\right|^2 \right) R^2 d\theta d\phi \tag{33}$$

Finding the radiated power is crucial to the next calculation step in the cavity model: finding the input impedance. A general formula for the input impedance that can be used in conjunction with this model is:

$$Z_{in} = \frac{|V_{in}|^2}{P_{rad} + j2\omega(W_E - W_M)} \tag{34}$$

Here, V_{in} is the driving voltage at the input to the cavity, which depends on the specific feed structure used by the antenna; W_E is the time-averaged stored electric energy; and W_M is the time-averaged stored magnetic energy. Note that this formula assumes that the antenna is essentially lossless (with the exception of the power lost to radiation, of course). In reality, conductor losses, dielectric losses, etc., exist. These can be included in the formula by simply adding the power dissipated in these various forms to P_{rad} in the denominator. The time-averaged stored electric and magnetic energies are computed through standard electromagnetic integrals over the volume of the cavity:

$$W_e = \frac{1}{2}\iiint_V \epsilon |E|^2 \, dV \tag{35}$$

$$W_m = \frac{1}{2}\iiint_V \mu |H|^2 \, dV \tag{36}$$

Here, E and H are the total fields inside the cavity, as expressed in equations (13) - (18).

In summary, once the total field inside the cavity is determined, the radiated fields, radiated power, and input impedance can be calculated. This allows a host of other quantities to be computed, such as the VSWR, gain, beamwidth, etc. However,

most of these further calculations are fundamental to antenna engineering and are omitted here.

The cavity model provides a reasonable way to predict the performance of planar patch antennas, including the PIFA. The same principles are applied to the SIFA in the next several sections of this chapter. First, a custom coordinate system is introduced to describe the geometry of the SIFA. The geometry of the SIFA cavity itself is then described and its boundary conditions defined. Finally, the wave equation is solved inside the SIFA cavity, and the subsequent desired calculations are performed. The performance of the SIFA cavity model is compared to previous simulated and measured results.

C. Custom Coordinate System

Close inspection of the patch geometry of the SIFA reveals that it can only be described mathematically by a complex combination of spherical and rectangular coordinates. In fact, the SIFA patch can be expressed much more efficiently by introducing a custom curvilinear coordinate system tailored specifically to the patch geometry. Fig. 38 summarizes such a coordinate scheme. It is given in terms of coordinates u, v, and w, with u being a linear quantity and v and w being angular quantities. This *uvw* system has many similarities to the standard spherical coordinates. The coordinate u is a radial distance measured from the origin to any point of interest, denoted P_1; this is equivalent to the spherical coordinate r, with a constant-u surface defining a sphere. The coordinate v is similar to the spherical coordinate θ and is

defined as the angle measured between the z-axis and a constant-v half-plane defined by P_1 and the y-axis. The coordinate w is similar to the spherical coordinate ϕ and is defined as the angle measured from the x-axis to the line segment from the origin to the point found on the xy-plane that lies on the curve of intersection between the constant-u sphere and the constant-y plane that both contain P_1. The constant-w surface is fairly difficult to describe and is omitted from Fig. 38. Instead, since it is more intuitive, the constant-y plane that helps to define w is included in the figure.

The relation of the *uvw* coordinates to standard Cartesian coordinates is given as follows:

$$x = u\cos(w)\sin(v) \tag{37}$$

$$y = u\sin(w) \tag{38}$$

$$z = u\cos(w)\cos(v) \tag{39}$$

Note that this coordinate system bears much resemblance to the spherical coordinate system, with only a few minor differences. In *uvw* space, the SIFA can be said to occupy the following region:

$$R_i \le u \le R_o \tag{40}$$

$$\theta_g \le v \le \frac{\pi}{2} - \theta_s \tag{41}$$

$$-\frac{\phi_w}{2} \le w \le \frac{\phi_w}{2} \tag{42}$$

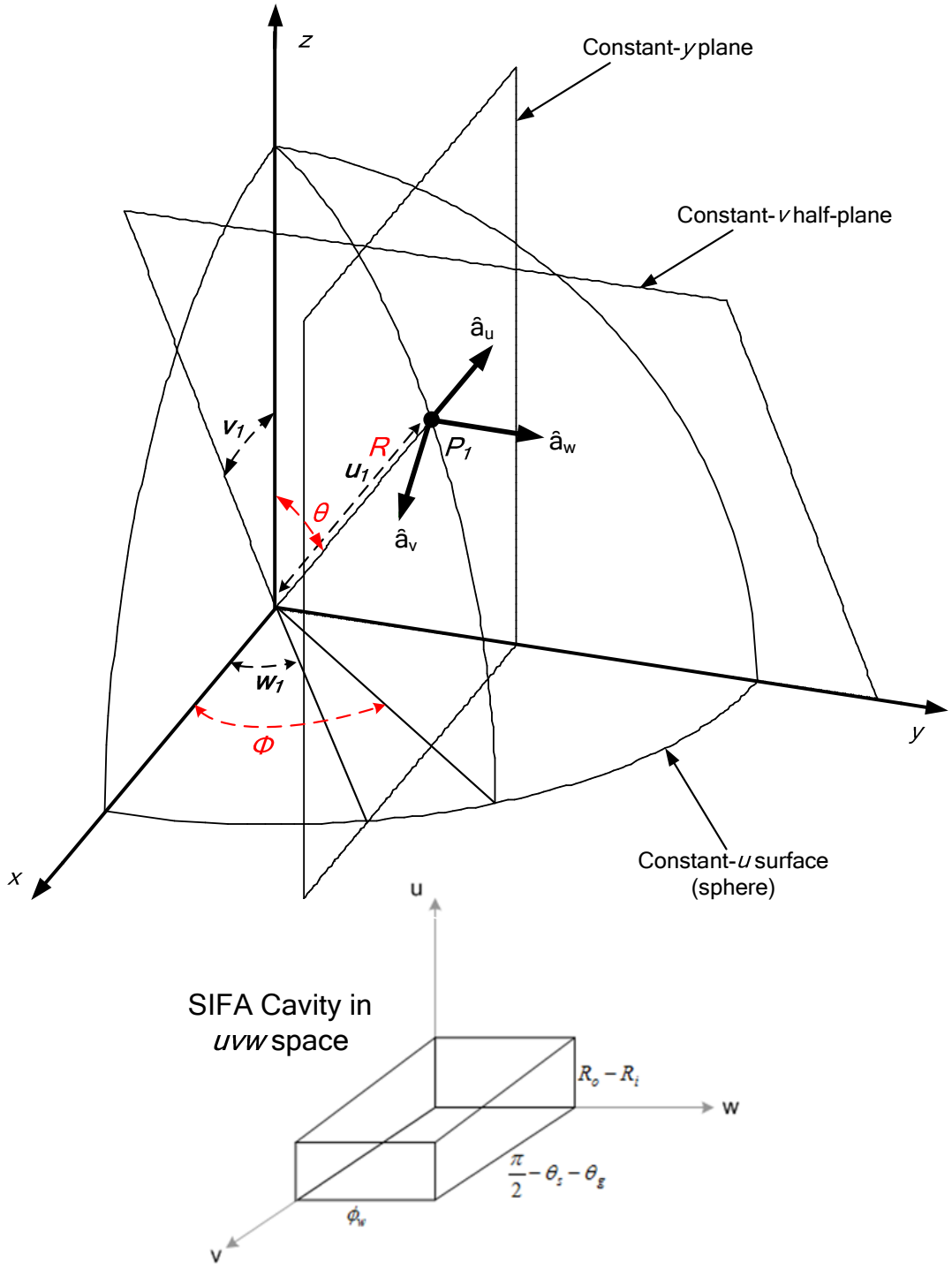

Fig. 38. Custom curvilinear coordinate system for the SIFA cavity. The standard spherical coordinates are shown in red for reference. Also included is a view of the SIFA cavity in *uvw* space

To explain the motivation for using this custom curvilinear coordinate system in lieu of spherical coordinates, Fig. 38 includes a view of the SIFA cavity in *uvw* space. Clearly, when mapped from Cartesian space to *uvw* space, the SIFA is in the familiar shape of a rectangular prism. Thus, in *uvw* space, the problem becomes analogous to the planar cavity model in Cartesian coordinates.

Several important quantities associated with the *uvw* curvilinear coordinate system are as follows. The Jacobian determinant is:

$$\left|J\left(u,v,w\right)\right| = u^2 \cos w \tag{43}$$

The metric coefficients [38] are given in (44)-(46); the subscripts 1, 2, and 3 correspond to the coordinates u, v, and w, respectively. Physically, these coefficients represent factors of multiplication that transform differential angles into differential arc lengths (note that $h_1 = 1$ because u is not an angle but is already a distance). These coefficients are necessary in determining *uvw* operators, such as the curl operator (47).

$$h_1 = 1 \tag{44}$$

$$h_2 = u \cos w \tag{45}$$

$$h_3 = u \tag{46}$$

$$\begin{aligned}\nabla \times \vec{A} = {} & \frac{1}{u\cos w}\left[\frac{\partial A_w}{\partial v} - \frac{\partial}{\partial w}\left(\cos w A_v\right)\right]\hat{a}_u + \frac{1}{u}\left[\frac{\partial A_u}{\partial w} - \frac{\partial}{\partial u}\left(uA_w\right)\right]\hat{a}_v + \\ & \frac{1}{u}\left[\frac{\partial}{\partial u}\left(uA_v\right) - \frac{1}{\cos w}\frac{\partial A_u}{\partial v}\right]\hat{a}_w\end{aligned} \tag{47}$$

D. The SIFA Cavity

The "cavity" of the SIFA that corresponds most closely to the rectangular cavity of a planar patch antenna is a fairly complex geometrical structure. It can visualized as follows: first, the two-dimensional patch geometry on the surface of the SIFA is removed from the sphere, then, this two-dimensional surface is extruded radially inward a distance $h = R_o - R_i$. The resulting three-dimensional structure is shown in Fig. 39. Note that the radial cross section of this cavity is the same shape for every value of the radius; the surface area of each cross section simply increases with the radial distance.

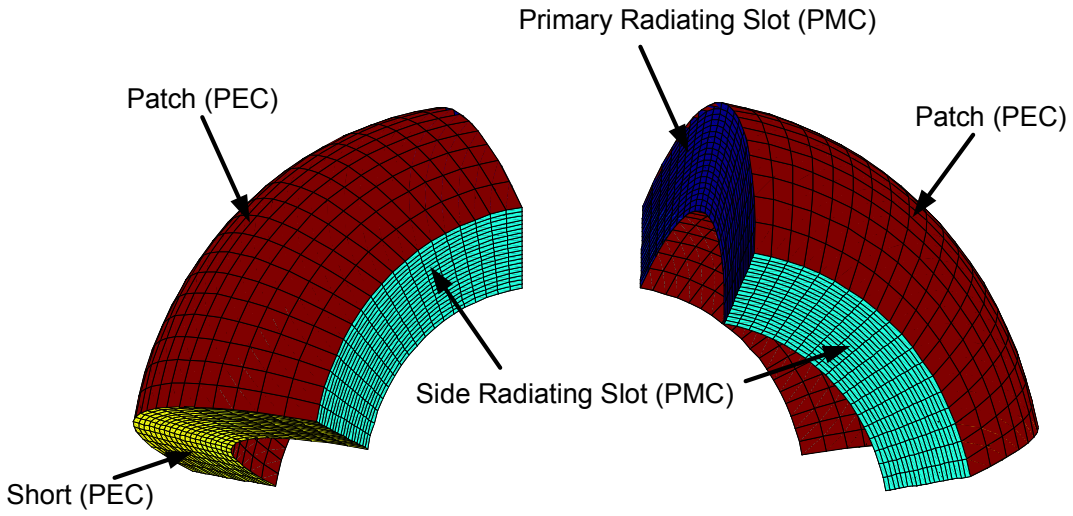

Fig. 39. The SIFA cavity. The cavity is shown from two viewpoints so as to include all six surfaces

Each of the six surfaces of this cavity are assigned either a PEC or PMC boundary condition. The constant $u = R_0$ surface represents the actual metallic patch of the SIFA and is thus a PEC surface. The constant $u = R_i$ surface is part of the SIFA's

ground plane and is also a PEC surface. The constant $w = \phi_w / 2$ and $w = -\phi_w / 2$ surfaces are the side radiating slots and are modeled as PMC surfaces. The constant $v = \theta_g$ surface is the primary radiating slot and is also a PMC surface. The final surface, at a constant $v = \pi - \theta_s$, is modeled as a shorting wall with PEC boundary condition, just as in the PIFA cavity model. Note that this shorting wall does not accurately represent the physical shorting strip in the actual SIFA design, which is conformal to the spherical surface rather than radially directed; however, this modeling is a good approximation based on the PIFA cavity that helps to greatly simplify the SIFA cavity analysis.

E. The Wave Equation and Its Solution

The first step in applying the cavity method to the SIFA, as with the PIFA, is to write out and solve the wave equation for the cavity. As for the PIFA, the complex scalar wave equation, or Helmholtz equation, is:

$$\nabla^2 \psi + k^2 \psi = 0 \tag{48}$$

In the SIFA's custom coordinate system, the wave equation can be expanded as:

$$\frac{1}{u^2}\frac{\partial}{\partial u}\left(u^2 \frac{\partial \psi}{\partial u}\right) + \frac{1}{\left(u\cos w\right)^2}\frac{\partial^2 \psi}{\partial v^2} + \frac{1}{u^2 \cos w}\frac{\partial}{\partial w}\left(\cos w \frac{\partial \psi}{\partial w}\right) + k^2 \psi = 0 \tag{49}$$

To solve this equation, the method of separation of variables is used; the solutions are assumed to take on the form:

$$\psi = A(u)B(v)C(w) \tag{50}$$

With this assumption, the wave equation can be separated into three one-variable equations as follows:

$$\frac{1}{B}\frac{\partial^2 B}{\partial v^2} = -\mu_r{}^2 \tag{51}$$

$$\frac{1}{\cos w}\frac{\partial}{\partial w}\left(\cos w \frac{\partial C}{\partial w}\right) + \left[\nu_r\left(\nu_r + 1\right) - \frac{\mu_r{}^2}{\left(\cos w\right)^2}\right] = 0 \tag{52}$$

$$\frac{\partial}{\partial u}\left(u^2 \frac{\partial A}{\partial u}\right) + A\left[k^2 u^2 - \nu_r\left(\nu_r + 1\right)\right] = 0 \tag{53}$$

Here, μ_r and ν_r are separation constants that are introduced in the separation process. The subscript r is included simply to differentiate them from, say, electromagnetic permeability μ.

The boundary conditions for the problem are defined by the PEC and PMC surfaces discussed for the SIFA cavity in the previous section. The three separated equations can be solved subject to these boundary conditions. Two of the three solutions require accompanying transcendental equations; these solution forms are attained following the manner of [39]. The first equation shown in (51) is simply a harmonic equation with a general solution (54) and factor μ_r given by (55). This solution assures that the tangential electric field goes to zero on the shorting section at $v = \frac{\pi}{2} - \theta_s$ and the tangential electric field goes to zero at $v = \theta_g$.

$$B = \cos\left(\mu_r\left[v - \theta_g\right]\right) \tag{54}$$

$$\mu_r = \frac{m\pi}{2\left(\frac{\pi}{2} - \theta_s - \theta_g\right)}, \quad m = 1,3,5\ldots \tag{55}$$

The second separated equation in (52) is a Legendre differential equation. A general solution that satisfies the boundary condition at $w = \phi_w / 2$ is:

$$C = Q_{\nu_r}^{\mu_r\prime}\left(\sin\frac{\phi_w}{2}\right) P_{\nu_r}^{\mu_r}\left(\sin w\right) - P_{\nu_r}^{\mu_r\prime}\left(\sin\frac{\phi_w}{2}\right) Q_{\nu_r}^{\mu_r}\left(\sin w\right) \tag{56}$$

Here, $P_{\nu_r}^{\mu_r}\left(x\right)$ is an associated Legendre function of the first kind with order μ_r and degree ν_r, and $Q_{\nu_r}^{\mu_r}\left(x\right)$ is an associated Legendre function of the second kind with order μ_r and degree ν_r; $P_{\nu_r}^{\mu_r\prime}\left(x\right)$ and $Q_{\nu_r}^{\mu_r\prime}\left(x\right)$ are the derivatives of these functions, respectively. These two associated Legendre functions are linearly independent solutions to the basic Legendre equation and are put together here in a linear combination. In this case, their order and degree are arbitrary fractional values, as opposed to integer values that appear in many other applications of the Legendre equation. These fractional values make computation of these functions somewhat more involved than would be necessary with integer values. In order to satisfy the other boundary condition of the w-dependent Legendre equation at $w = -\phi_w / 2$, the transcendental equation (57) must be satisfied. This transcendental equation determines the value of the unknown parameter ν_r to be used in (56).

$$Q_{\nu_r}^{\mu_r\prime}\left(\sin\frac{\phi_w}{2}\right) P_{\nu_r}^{\mu_r\prime}\left(\sin\left[-\frac{\phi_w}{2}\right]\right) = P_{\nu_r}^{\mu_r\prime}\left(\sin\frac{\phi_w}{2}\right) Q_{\nu_r}^{\mu_r\prime}\left(\sin\left[-\frac{\phi_w}{2}\right]\right) \tag{57}$$

The third and final separated equation (53) is a spherical Bessel equation with a general solution written as:

$$A = n_{\nu_r}{}'\left(k_d R_i\right) j_{\nu_r}\left(k_d u\right) - j_{\nu_r}{}'\left(k_d R_i\right) n_{\nu_r}\left(k_d u\right) \tag{58}$$

This satisfies the first boundary condition at $u = R_i$, with $j_{\nu_r}\left(x\right)$ a spherical Bessel function of the first kind with order ν_r and $n_{\nu_r}\left(x\right)$ a spherical Bessel function of the second kind with order ν_r; $j_{\nu_r}{}'\left(x\right)$ and $n_{\nu_r}{}'\left(x\right)$ are the derivatives of these functions. These two functions are linearly independent solutions of the spherical Bessel equation, and they are put together in (58) as a linear combination. The order ν_r is an arbitrary fractional number, as opposed to more commonly seen integer values, making computation of the Bessel functions more difficult. The second boundary condition at $u = R_o$ must be satisfied by a transcendental equation:

$$n_{\nu_r}{}'\left(k_d R_i\right) j_{\nu_r}{}'\left(k_d R_o\right) = j_{\nu_r}{}'\left(k_d R_i\right) n_{\nu_r}{}'\left(k_d R_o\right) \tag{59}$$

This equation provides the value of the unknown parameter k_d, which can then be used in (58). This parameter k_d (60) is the wavenumber of the cavity for a particular mode; the resonant frequency of each mode can be determined from it.

$$k_d = \omega\sqrt{\mu\varepsilon} \tag{60}$$

The resonant frequency of a particular mode can be determined from the relation above.

In summary, solutions can be found for the three separated, one-dimensional differential equations in terms of known harmonic functions and special functions. The use of (55), along with the transcendental equations in (57) and (59), yield the fractional

modal quantities μ_r, ν_r, and k_d. These modal quantities correspond to the integer modal indexes found, for example, in the PIFA cavity model. Although not as mathematically convenient as integer indexes, these fractional modal quantities are the best way to describe the wave potential in the SIFA cavity. If so desired, they can be mapped to integer indexes since they are, in fact, a countable and infinite set. However, in this work, they will be kept in fractional form.

F. Superposition of Solutions

The expressions in (54), (56), and (59) provide modal solutions to the wave equation inside the SIFA cavity. Now, the relative strengths of the excited modes in the cavity must be determined, and the modes must be superimposed to provide a total solution. In other words, the effect of the excitation by the coaxial probe must be accounted for. To do this, the non-homogenous Helmholtz equation (61) is needed.

$$\left(\nabla^2 + k^2\right)\psi = -j\omega\mu J \tag{61}$$

The non-homogeneous equation is simply the original wave equation (48) with the additional right-hand term, or forcing function, $-j\omega\mu J$. This term accounts for the current driving the fields inside the cavity, with J being the current density and μ being permeability. The solution of (61) provides the specific modes within the SIFA cavity, based on the known coaxial probe excitation. From basic knowledge of differential equations, the solution to a non-homogenous equation involves finding a particular solution as well as the known solution to the homogeneous equation.

As was mentioned in the PIFA cavity model discussion, the total solution to the wave equation inside the cavity is simply the sum of the modal contributions, as in (29), with each mode having a specific amplitude. For the SIFA, assume that the total solution ψ has the following form:

$$\psi = \sum M_{\mu\nu k} \psi_{\mu\nu k} \tag{62}$$

Here, $M_{\mu\nu k}$ are the unknown modal weighting coefficients to be determined, and $\psi_{\mu\nu k}$ are the modal solutions to the wave equation. The subscript $\mu\nu k$ refers to the modal indexes μ_r, ν_r, and k_d. Furthermore, the summation is assumed to be over all possible modes (a single summation sign is used for simplicity). Subtracting the non-homogeneous Helmholtz equation from the homogeneous one and substituting the summation of (62) for ψ yields (63), which can be manipulated into (64).

$$k_d^2 \sum M_{\mu\nu} \psi_{\mu\nu} - k^2 \sum M_{\mu\nu} \psi_{\mu\nu} = j\omega\mu J \tag{63}$$

$$\sum \left(k_d^2 - k^2 \right) M_{\mu\nu k} \psi_{\mu\nu k} = j\omega\mu J \tag{64}$$

Next, an inner product is applied to both sides of the equation to exploit the orthogonality of the modal solutions. Specifically, the inner product of each side with the quantity ψ^*_{mnp} is computed, where $*$ denotes a complex conjugate and mnp are arbitrary fractional modal quantities. The notion of an inner product here will not be fully developed mathematically. In this case, it suffices to mimic the cavity method in rectangular coordinates, in which the inner product consists of spatial integration over the volume of the cavity. This volume integral in uvw space is given in terms of generic vector space elements a and b as follows:

$$\langle a,b\rangle = \iiint_V ab^* u^2 \cos w \, du\, dv\, dw \tag{65}$$

The inner product, then, is denoted by $\langle\ \rangle$. Application of the inner product operation to (64) yields:

$$\sum \left(k_d^2 - k^2\right) M_{\mu\nu k} \left\langle \psi_{\mu\nu k}, \psi_{mnp}^* \right\rangle = j\omega\mu \left\langle J, \psi_{mnp}^* \right\rangle \tag{66}$$

Note that since the inner product is a linear operator, it can move inside the summation, and scalars can move outside of it.

The harmonic functions, associated Legendre functions, and spherical Bessel functions used in the solution for $\psi_{\mu\nu k}$ all have nice orthogonality properties, which will not be discussed in detail here. By virtue of this orthogonality, only one of the terms in the summation is nonzero (specifically, the term with index mnp), and equation (66) can be reduced to:

$$\left(k_d^2 - k^2\right) M_{\mu\nu k} \left\langle \psi_{mnp}, \psi_{mnp}^* \right\rangle = j\omega\mu \left\langle J, \psi_{mnp}^* \right\rangle \tag{67}$$

At this point, the mnp subscript is arbitrary, so it is fair to revert back to the original $\mu\nu k$ subscript to get:

$$\left(k_d^2 - k^2\right) M_{\mu\nu k} \left\langle \psi_{\mu\nu k}, \psi_{\mu\nu k}^* \right\rangle = j\omega\mu \left\langle J, \psi_{\mu\nu k}^* \right\rangle \tag{68}$$

The unknown coefficients can now be solved for easily, resulting in:

$$M_{\mu\nu k} = \frac{j\omega\mu}{k_d^2 - k^2} \frac{\left\langle J, \psi_{\mu\nu k}^* \right\rangle}{\left\langle \psi_{\mu\nu k}, \psi_{\mu\nu k}^* \right\rangle} \tag{69}$$

Substitution of (69) into (62) means that the total solution ψ is:

$$\psi = \sum \frac{j\omega\mu_0}{k_{\mu\nu}^2 - k^2} \frac{\left\langle J, r\psi_{\mu\nu}^* \right\rangle \psi_{\mu\nu}}{\left\langle \psi_{\mu\nu}, \psi_{\mu\nu}^* \right\rangle} \tag{70}$$

Here, the summation is over all possible modes. This solution for ψ contains all of the modes excited in the SIFA cavity, along with their amplitudes; it also includes the specific effect of the feed mechanism.

G. Cavity Fields

For the PIFA, assumptions about the fields in the cavity led to solving the cavity only for transverse magnetic fields – specifically, TM_z. The same principles can be applied to the SIFA. For the SIFA cavity, solutions only need to found for TM_u fields (i.e. transverse magnetic to the radial direction). This means that the radially directed magnetic field, H_u, will be zero.

At this point, the SIFA cavity model will follow a procedure based on standard electromagnetic solutions in spherical coordinates. This is due to the similarity between the *uvw* coordinates and spherical coordinates. Specifically, in spherical coordinates, TM_r solutions (transverse magnetic to the radial direction) are most often assumed, and this corresponds directly to the assumption of TM_u for the SIFA. Following the lead of spherical solutions, the relation between the wave potential and the magnetic vector potential inside the SIFA cavity can be written as:

$$\psi = \frac{A_u}{u} \tag{71}$$

Additionally, the following can be written:

$$\vec{A} = A_u \hat{a}_u = \psi u \hat{a}_u = \psi \vec{u} \tag{72}$$

Note that the magnetic vector potential only has a u-directed component (A_u). The reasons for including the factor of $1/u$ in (71) will not be detailed here; this choice is adopted from spherical solution methods.

The electric and magnetic fields inside the cavity can now be computed directly using reduced forms of equations (11) and (12) (assuming that $\vec{F}$ is zero and $\vec{A}$ is given by (71) and (70)):

$$\vec{E} = \frac{1}{j\omega\varepsilon} \nabla \times \nabla \times \vec{A} \tag{73}$$

$$\vec{H} = \nabla \times \vec{A} \tag{74}$$

Expanding these equations into their uvw components yields:

$$E_u = \frac{1}{j\omega\varepsilon} \left(\frac{\partial^2 (\psi u)}{\partial u^2} + k^2 (\psi u) \right) \tag{75}$$

$$E_v = -\frac{1}{j\omega\varepsilon u \cos w} \frac{\partial^2 (\psi u)}{\partial u \partial v} \tag{76}$$

$$E_w = \frac{1}{j\omega\varepsilon u} \frac{\partial^2 (\psi u)}{\partial u \partial v} \tag{77}$$

$$H_u = 0 \tag{78}$$

$$H_v = \frac{1}{u} \frac{\partial (\psi u)}{\partial w} \tag{79}$$

$$H_w = -\frac{1}{u \cos w} \frac{\partial (\psi u)}{\partial v} \tag{80}$$

The superimposed solution for ψ is simply substituted into these equations to find the three-dimensional field intensities inside the cavity.

The wave potential ψ in (72) is always multiplied by the radial vector $\vec{u}$ before $\vec{A}$ is used, via (73) and (74), to compute the field quantities. In spherical coordinates, it is customary to incorporate the magnitude of $\vec{u}$ into the wave potential solution ψ by introducing what are known as Schelkunoff-type spherical Bessel functions. Specifically, the spherical Bessel functions $j_{\nu_r}(x)$ and $n_{\nu_r}(x)$ used in (58) and (59) for the solution to the wave equation are replaced with Schelkunoff-type functions $\hat{J}_{\nu_r}(x)$ and $\hat{N}_{\nu_r}(x)$, respectively. The Schelkunoff-type functions are simply the standard spherical Bessel functions times the radial distance u (or r in spherical coordinates):

$$\hat{J}_{\nu_r}(x) = uj_{\nu_r}(x) \tag{81}$$

$$\hat{N}_{\nu_r}(x) = un_{\nu_r}(x) \tag{82}$$

Note that the Schelkunoff-type spherical Bessel functions are distinguished from standard Bessel functions by the hat symbol ($\wedge$). If the standard spherical Bessel functions in equations (58) and (59) are replaced by the Schelkunoff-type functions, the results are:

$$A = \hat{N}_{\nu_r}{}'(k_d R_i)\hat{J}_{\nu_r}(k_d u) - \hat{J}_{\nu_r}{}'(k_d R_i)\hat{N}_{\nu_r}(k_d u) \tag{83}$$

$$\hat{N}_{\nu_r}{}'(k_d R_i)\hat{J}_{\nu_r}{}'(k_d R_o) = \hat{J}_{\nu_r}{}'(k_d R_i)\hat{N}_{\nu_r}{}'(k_d R_o) \tag{84}$$

If (83) and (84) are used in the computation of ψ given in (50), then the relation of the magnetic vector potential and this new wave potential – call it $\hat{\psi}$ (the hat symbol designates it as being computed using Schelkunoff-type functions) – becomes:

$$\vec{A} = \hat{\psi}\hat{a}_u \tag{85}$$

This more closely resembles the rectangular case of the PIFA (i.e., equation (8)), in which ψ is simply a component of $\vec{A}$. This is a simpler relation than was necessary in (71) and (72).

In summary, then, the wave potential $\hat{\psi}$, employing the Schelkunoff-type functions, can be directly used in equations (75)-(80) in place of ψu (i.e., without the need to multiply by the factor u). This final step of finding the fields in the cavity by using Schelkunoff-type spherical Bessel functions, while not necessary, gives a more convenient solution that is more directly analogous to rectangular problems for the cavity model (e.g. the PIFA). Additionally, this step mimics the customary procedure used in spherical electromagnetic problems.

H. Side Slot Radiated Power

As in the PIFA cavity model, one of the most important calculations following the solution of the fields inside the cavity is the radiated power. The SIFA has three radiating slots, each of which can be handled separately. Computation of the radiation from the side slots is performed first here. Due to symmetry, the power radiated by both

side slots should be identical, although the actual fields produced by each slot are different.

The process of computing the radiation is best started by writing the Cartesian coordinates of the side slots as functions (86)-(88) of the custom *uvw* coordinates. These are combined into a vector description (89) of the side-slot surfaces $\overrightarrow{R'}$.

$$x = u\cos\left(\frac{\phi_w}{2}\right)\sin(v) \tag{86}$$

$$y = \pm u\sin\left(\frac{\phi_w}{2}\right) \tag{87}$$

$$z = u\cos\left(\frac{\phi_w}{2}\right)\cos(v) \tag{88}$$

$$\overrightarrow{R'} = u\cos\left(\frac{\phi_w}{2}\right)\sin(v)\hat{a}_u \pm u\sin\left(\frac{\phi_w}{2}\right)\hat{a}_v + u\cos\left(\frac{\phi_w}{2}\right)\cos(v)\hat{a}_w \tag{89}$$

Here, the prime on $\overrightarrow{R'}$ does not refer to a derivative; it is simply there for notational purposes. Note that this surface is entirely tangent to the radial (R) direction in spherical coordinates. Thus, the radial electric field is completely tangent to the surface. This field is obtained from the modal calculations – specifically, equation (75) – and is denoted here by:

$$\overrightarrow{E}_{ss} = E_0 E_u(u,v)\hat{a}_u \tag{90}$$

Here, the field has a magnitude of E_0, varies as the unit-normalized function $E(u,v)$, and is directed in the $\hat{a}_u$ direction. The subscript ss signals that the field occurs on the

side slot. In the most general case, this field varies both with u and v. The field on the side slot surfaces gives rise to an equivalent magnetic surface current:

$$\vec{M}_s = -2\hat{a}_n \times \vec{E}_{ss} \tag{91}$$

Here, $\hat{a}_n$ is the unit normal vector to the side slot surface. The electric vector potential caused by the side slot current can be computed directly from $\vec{M}_s$:

$$\vec{F} = \frac{\epsilon}{4\pi} \iint_{S'} \vec{M}_s \frac{e^{-jk\left|\vec{R}-\vec{R'}\right|}}{\left|\vec{R}-\vec{R'}\right|} dS' \tag{92}$$

$$\vec{F} = \frac{\epsilon}{4\pi} \iint_{S'} \left(-2\hat{n} \times \vec{E}\right) \frac{e^{-jk\left|\vec{R}-\vec{R'}\right|}}{\left|\vec{R}-\vec{R'}\right|} dS' \tag{93}$$

The primed quantities (surface S', vector $\vec{R'}$) correspond to the side slot surface, whereas the unprimed quantity $\vec{R}$ refers to a point in the far field.

The electric vector potential $\vec{F}$ in equation (93) can be simplified as follows. Using a parallel ray approximation standard for antenna problems (e.g. as in [40]), the phase term in the integral can be approximated as:

$$e^{-jk\left|\vec{R}-\vec{R'}\right|} = e^{-jk\left(R-\left|R'\cos\alpha\right|\right)} = e^{-jk\left(R-u\left|\cos\alpha\right|\right)} \tag{94}$$

Here, α is the angle between the vectors $\vec{R}$ and $\vec{R'}$. The parallel ray approximation also dictates that the denominator of the integrand (magnitude term) be reduced to:

$$\frac{1}{\left|\vec{R}-\vec{R'}\right|} \cong \frac{1}{R} \tag{95}$$

The term $\cos\alpha$ can be derived from the dot product between $\vec{R}$ and $\vec{R'}$ (since $\vec{R}\cdot\vec{R'}=\left|\vec{R}\right|\left|\vec{R'}\right|\cos\alpha$). This dot product can be performed in Cartesian coordinates:

$$\begin{aligned}\cos\alpha =&\left(\sin\theta\cos\phi\hat{a}_x+\sin\theta\sin\phi\hat{a}_y+\cos\theta\hat{a}_z\right)\\ \bullet&\left(\cos\left(\frac{\phi_w}{2}\right)\sin(v)\hat{a}_x\pm\sin\left(\frac{\phi_w}{2}\right)\hat{a}_y+\cos\left(\frac{\phi_w}{2}\right)\cos(v)\hat{a}_z\right)\end{aligned} \tag{96}$$

$$\cos\alpha=\sin\theta\cos\phi\cos\left(\frac{\phi_w}{2}\right)\sin(v)\pm\sin\theta\sin\phi\sin\left(\frac{\phi_w}{2}\right)+\cos\theta\cos\left(\frac{\phi_w}{2}\right)\cos(v) \tag{97}$$

Employing the parallel ray approximations changes equation (93) to the following:

$$\vec{F}=\frac{\epsilon}{4\pi R}\iint_{S'}\left(-2\hat{a}_n\times\vec{E}\right)e^{-jk\left(R-u\left|\cos\alpha\right|\right)}dS' \tag{98}$$

Now, the normal vector to the slot, $\vec{n}$, must be determined. To do this, the partial derivatives of $\vec{R'}$ with respect to u and v are computed:

$$\frac{\partial}{\partial u}\vec{R'}=\vec{R}_u{}'=\cos\left(\frac{\phi_w}{2}\right)\sin(v)\hat{a}_x\pm\sin\left(\frac{\phi_w}{2}\right)\hat{a}_y+\cos\left(\frac{\phi_w}{2}\right)\cos(v)\hat{a}_z \tag{99}$$

$$\frac{\partial}{\partial v}\vec{R'}=\vec{R}_v{}'=u\cos\left(\frac{\phi_w}{2}\right)\cos(v)\hat{a}_x-u\cos\left(\frac{\phi_w}{2}\right)\sin(v)\hat{a}_z \tag{100}$$

The normal vector to the surface (not the unit normal) is then given by:

$$\vec{n}=\vec{R}_u{}'\times\vec{R}_v{}' \tag{101}$$

$$\begin{aligned}\vec{n}=&-u\sin\left(\frac{\phi_w}{2}\right)\cos\left(\frac{\phi_w}{2}\right)\sin(v)\hat{a}_x\pm u\left(\cos\left(\frac{\phi_w}{2}\right)\right)^2\hat{a}_y\\ &-u\sin\left(\frac{\phi_w}{2}\right)\cos\left(\frac{\phi_w}{2}\right)\cos v\hat{a}_z\end{aligned} \tag{102}$$

This Cartesian vector can be converted into a vector in terms of spherical unit vectors:

$$\begin{aligned}\vec{n} = &\begin{pmatrix} -\sin\left(\frac{\phi_w}{2}\right)\cos\left(\frac{\phi_w}{2}\right)\sin(v)\sin(\theta)\cos(\phi)+\cos\left(\frac{\phi_w}{2}\right)^2\sin(\theta)\sin(\phi) \\ -\sin\left(\frac{\phi_w}{2}\right)\cos\left(\frac{\phi_w}{2}\right)\cos(v)\cos(\theta) \end{pmatrix}\hat{a}_r \\ +u&\begin{pmatrix} -\sin\left(\frac{\phi_w}{2}\right)\cos\left(\frac{\phi_w}{2}\right)\sin(v)\cos(\theta)\cos(\phi)+\cos\left(\frac{\phi_w}{2}\right)^2\cos(\theta)\sin(\phi) \\ +\sin\left(\frac{\phi_w}{2}\right)\cos\left(\frac{\phi_w}{2}\right)\cos(v)\sin(\theta) \end{pmatrix}\hat{a}_\theta \\ +u&\left(\sin\left(\frac{\phi_w}{2}\right)\cos\left(\frac{\phi_w}{2}\right)\sin(v)\sin(\phi)+\cos\left(\frac{\phi_w}{2}\right)^2\cos(\phi)\right)\hat{a}_\phi\end{aligned} \quad (103)$$

This normal vector is then crossed with $\hat{a}_r$ (which is the same as $\hat{a}_u$) to obtain:

$$\begin{aligned}\vec{n}\times\hat{a}_r = \vec{n}\times\hat{a}_u = u&\begin{pmatrix} \sin\left(\frac{\phi_w}{2}\right)\cos\left(\frac{\phi_w}{2}\right)\sin(v)\cos(\theta)\cos(\phi)- \\ \cos\left(\frac{\phi_w}{2}\right)^2\cos(\theta)\sin(\phi)- \\ \sin\left(\frac{\phi_w}{2}\right)\cos\left(\frac{\phi_w}{2}\right)\cos(v)\sin(\theta) \end{pmatrix}\hat{a}_\phi \\ +u&\left(\sin\left(\frac{\phi_w}{2}\right)\cos\left(\frac{\phi_w}{2}\right)\sin(v)\sin(\phi)+\cos\left(\frac{\phi_w}{2}\right)^2\cos(\phi)\right)\hat{a}_\theta\end{aligned} \quad (104)$$

Referring back to the expression for $\vec{F}$ in equation (98), the surface differential dS' can be expanded as:

$$dS' = \left|\vec{n}\right| du dv \quad (105)$$

Now, $\vec{F}$ from equation (98) can be rewritten as:

$$\vec{F} = \frac{\varepsilon}{4\pi R}\iint_{S'}\left(-2\frac{\vec{n}}{\left|\vec{n}\right|}\times\vec{E}\right)e^{-jk\left(R-u\left|\cos\alpha\right|\right)}\left|\vec{n}\right| du dv \quad (106)$$

$$\vec{F} = \frac{-2\varepsilon}{4\pi R} \iint_{S'} \left(\vec{n} \times \vec{E} \right) e^{-jk\left(R - u|\cos\alpha|\right)} du dv \tag{107}$$

$$\vec{F} = \frac{-2\varepsilon E_0}{4\pi R} \iint_{S'} \left(\vec{n} \times \hat{a}_u \right) E\left(u,v\right) e^{-jk\left(R - u|\cos\alpha|\right)} du dv \tag{108}$$

$$\vec{F} = \frac{-2\varepsilon E_0 e^{-jkR}}{4\pi R} \iint_{S'} \left(\vec{n} \times \hat{a}_u \right) E\left(u,v\right) e^{-jku|\cos\alpha|} du dv \tag{109}$$

Note that all of the terms in the double integral, including $\vec{n} \times \hat{a}_u$, $E\left(u,v\right)$, and $\cos\alpha$ are now known; the integral can now be computed numerically. The term $-2\varepsilon / 4\pi$ is also known. The terms E_0, e^{-jkR}, and $1/R$ can be kept for now, since all three of these terms will be cancelled out shortly. Denoting the integral and the known multiplicative constants as $\overrightarrow{I^a}$, the electric vector potential can simply be written as:

$$\vec{F} = \frac{E_0 e^{-jkR} \overrightarrow{I^a}}{R} \tag{110}$$

$$\overrightarrow{I^a} = \frac{-2\varepsilon}{4\pi} \iint_{S'} \left(\vec{n} \times \hat{a}_u \right) E\left(u,v\right) e^{-jku|\cos\alpha|} du dv \tag{111}$$

Note that the integral results in both a θ and a ϕ component (and is thus a vector), since the term $\vec{n} \times \hat{a}_u$ contains these two components; that is, $\overrightarrow{I^a}$ is composed of I_ϕ^a and I_θ^a and $\vec{F}$ is likewise composed of F_ϕ and F_θ:

$$\overrightarrow{I^a} = I_\phi^a \hat{a}_\phi + I_\theta^a \hat{a}_\theta \tag{112}$$

$$\vec{F} = F_\phi \hat{a}_\phi + F_\theta \hat{a}_\theta \tag{113}$$

Note further that both components of $\overrightarrow{I^a}$ (and thus $\vec{F}$) are themselves functions of ϕ and θ, since the terms $\vec{n}\times\hat{a}_u$ and $\cos\alpha$ are function of these angles.

The computed electric vector potential can be used to determine the radiated electric field in the far field. Specifically:

$$E_\theta = -j\omega\eta F_\phi \tag{114}$$

$$E_\phi = -j\omega\eta F_\theta \tag{115}$$

These relations result from $\vec{E} = \nabla\times\vec{F}$ reduced into its components. At this point, the radiated field pattern of the SIFA side slot is known.

From the electric far field, the total radiated power can now be calculated by integrating the field over a full sphere in the far field:

$$P_{rad} = \frac{1}{\eta}\iint_{4\Omega}\left(\left|E_\theta\right|^2 + \left|E_\phi\right|^2\right)R^2 d\theta d\phi \tag{116}$$

$$P_{rad} = \frac{1}{\eta}\iint_{4\Omega}\left(\left|-j\omega\eta F_\phi\right|^2 + \left|j\omega\eta F_\theta\right|^2\right)R^2 d\theta d\phi \tag{117}$$

$$P_{rad} = \omega^2\eta\iint_{4\Omega}\left(\left|\frac{E_0 e^{-jkR} I_\phi^a}{R}\right|^2 + \left|\frac{E_0 e^{-jkR} I_\theta^a}{R}\right|^2\right)R^2 d\theta d\phi \tag{118}$$

$$P_{rad} = \omega^2\eta E_0^2\iint_{4\Omega}\left(\left|I_\phi^a\right|^2 + \left|I_\theta^a\right|^2\right)d\theta d\phi \tag{119}$$

The terms I_ϕ^a and I_θ^a are already known as functions of θ and ϕ, so this double integral can be computed numerically over the full range of these angles. Denoting this integral multiplied by the constants $\omega^2\eta$ as I^b (a scalar), the radiated power can simply be written as:

$$P_{rad} = E_0^2 I^b \tag{120}$$

$$I^b = \omega^2 \eta \iint_{4\Omega} \left(\left| I_\phi^a \right|^2 + \left| I_\theta^a \right|^2 \right) d\theta d\phi \tag{121}$$

This completes the computation of the radiation from the side slots of the SIFA. The radiated fields themselves are given in (114), (115), (110), and (111), whereas the power is given by equations (120) and (121) above. For now, the amplitude E_0 of the electric field inside the cavity is unknown; it is dependent on the strength of the excitation of the coaxial probe.

I. Primary Slot Radiated Power

The derivation of the radiation from the primary slot of the SIFA cavity follows the same steps as were performed for the side slots; only the geometrical terms change in the equations. For the sake of the thoroughness of this new model, however, all of the steps are repeated here. The primary slot surface has Cartesian coordinates – given as functions of the custom curvilinear coordinate system – as follows:

$$x = u \cos(w) \sin(\theta_g) \tag{122}$$

$$y = u \sin(w) \tag{123}$$

$$z = u \cos(w) \cos(\theta_g) \tag{124}$$

The vector description of the primary slot , $\overrightarrow{R'}$, then, is given by:

$$\overrightarrow{R'} = u \cos(w) \sin(\theta_g) \hat{a}_x + u \sin(w) \hat{a}_y + u \cos(w) \cos(\theta_g) \hat{a}_z \tag{125}$$

Like the side slots, this surface is entirely tangent to the radial (R) direction in spherical coordinates. Thus, the radial electric field is completely tangent to the surface. The field, taken from modal superposition inside the cavity, is denoted here by:

$$\vec{E}_{ps} = E_0 E_u \left(u, w\right) \hat{a}_u \tag{126}$$

That is, the field has a magnitude of E_0, varies as the unit-normalized function $E\left(u, w\right)$, and is directed in the $\hat{a}_u$ direction. The subscript ps denotes this field as occurring on the primary slot. In the most general case, this field varies both with u and w.

The electric field on the primary slot surface gives rise to an equivalent magnetic surface current:

$$\overrightarrow{M}_s = -2\hat{a}_n \times \vec{E}_{ps} \tag{127}$$

Here, $\hat{a}_n$ is the unit normal vector to the primary slot. The electric vector potential caused by the slot can be computed directly from $\overrightarrow{M}_s$:

$$\overrightarrow{F} = \frac{\varepsilon}{4\pi} \iint_{S'} \overrightarrow{M}_s \frac{e^{-jk\left|\vec{R}-\overrightarrow{R'}\right|}}{\left|\vec{R}-\overrightarrow{R'}\right|} dS' \tag{128}$$

$$\overrightarrow{F} = \frac{\varepsilon}{4\pi} \iint_{S'} \left(-2\hat{a}_n \times \vec{E}_{ps}\right) \frac{e^{-jk\left|\vec{R}-\overrightarrow{R'}\right|}}{\left|\vec{R}-\overrightarrow{R'}\right|} dS' \tag{129}$$

Again, the primed quantities (surface S', vector $\overrightarrow{R'}$) correspond to the primary slot surface, whereas the unprimed quantity $\vec{R}$ refers to a point in the far field.

As was done for the side slot, the electric vector potential of the primary slot in equation (129) can be simplified as using a parallel ray approximation. The phase term in the integral becomes:

$$e^{-jk\left|\vec{R}-\vec{R'}\right|} = e^{-jk\left(R-\left|R'\cos\alpha\right|\right)} = e^{-jk\left(R-u\left|\cos\alpha\right|\right)} \tag{130}$$

Here, α is the angle between the vectors $\vec{R}$ and $\vec{R'}$. The denominator of the integrand (magnitude term) in equation (129) can be reduced to:

$$\frac{1}{\left|\vec{R}-\vec{R'}\right|} \cong \frac{1}{R} \tag{131}$$

As before, the term $\cos\alpha$ in the phase can be derived from the dot product between $\vec{R}$ and $\vec{R'}$ ($\vec{R}\cdot\vec{R'} = \left|\vec{R}\right|\left|\vec{R'}\right|\cos\alpha$). Specifically:

$$\begin{aligned}\cos\alpha = &\left(\sin\theta\cos\phi\hat{a}_x + \sin\theta\sin\phi\hat{a}_y + \cos\theta\hat{a}_z\right)\\ &\cdot\left(\cos\left(w\right)\sin\left(\theta_g\right)\hat{a}_x + \sin\left(w\right)\hat{a}_y + \cos\left(w\right)\cos\left(\theta_g\right)\hat{a}_z\right)\end{aligned} \tag{132}$$

$$\cos\alpha = \sin\theta\cos\phi\cos\left(w\right)\sin\left(\theta_g\right) + \sin\theta\sin\phi\sin\left(w\right) + \cos\theta\cos\left(w\right)\cos\left(\theta_g\right) \tag{133}$$

Employing the parallel ray approximation in equation (129) yields:

$$\vec{F} = \frac{\varepsilon}{4\pi R}\iint_{S'}\left(-2\hat{a}_n \times \vec{E}\right)e^{-jk\left(R-u\left|\cos\alpha\right|\right)}dS' \tag{134}$$

Now, the normal vector $\vec{n}$ must be determined. The partial derivatives of $\vec{R'}$ with respect to u and w are computed:

$$\vec{R}_u{}' = \cos\left(w\right)\sin\left(\theta_g\right)\hat{a}_x \pm \sin\left(w\right)\hat{a}_y + \cos\left(w\right)\cos\left(\theta_g\right)\hat{a}_z \tag{135}$$

$$\vec{R}_v{}' = -u\sin\left(w\right)\sin\left(\theta_g\right)\hat{a}_x \pm u\cos\left(w\right)\hat{a}_y - u\sin\left(w\right)\cos\left(\theta_g\right)\hat{a}_z \tag{136}$$

The normal vector to the surface (not the unit normal) is then given by:

$$\vec{n} = \vec{R}_u{}' \times \vec{R}_v{}' \tag{137}$$

$$\vec{n} = -u\cos\left(\theta_g\right)\hat{a}_x + u\sin\left(\theta_g\right)\hat{a}_z \tag{138}$$

This vector can be converted from a Cartesian vector to a spherical vector as:

$$\begin{aligned}\vec{n} = u\Big(&-\cos\left(\theta_g\right)\sin\left(\theta\right)\cos\left(\phi\right)+\sin\left(\theta_g\right)\cos\left(\theta\right)\Big)\hat{a}_r \\ -u\Big(&\cos\left(\theta_g\right)\cos\left(\theta\right)\cos\left(\phi\right)+\sin\left(\theta_g\right)\sin\left(\theta\right)\Big)\hat{a}_\theta + u\cos\left(\theta_g\right)\sin\left(\phi\right)\hat{a}_\phi\end{aligned} \tag{139}$$

This normal vector can be crossed with $\hat{a}_r$ (which is the same as $\hat{a}_u$) to obtain:

$$\begin{aligned}\vec{n}\times\hat{a}_r = \vec{n}\times\hat{a}_u = u\Big(&\cos\left(\theta_g\right)\cos\left(\theta\right)\cos\left(\phi\right)+\sin\left(\theta_g\right)\sin\left(\theta\right)\Big)\hat{a}_\phi \\ &+u\cos\left(\theta_g\right)\sin\left(\phi\right)\hat{a}_\theta\end{aligned} \tag{140}$$

Referring back to the expression for $\vec{F}$ in equation (134), the surface differential dS' can be expanded as:

$$dS' = \left|\vec{n}\right| dudw \tag{141}$$

Now, $\vec{F}$ in equation (134) can be rewritten as:

$$\vec{F} = \frac{\varepsilon}{4\pi R}\iint_{S'}\left(-2\frac{\vec{n}}{\left|\vec{n}\right|}\times\vec{E}\right)e^{-jk\left(R-u\left|\cos\alpha\right|\right)}\left|\vec{n}\right| dudw \tag{142}$$

$$\vec{F} = \frac{-2\varepsilon}{4\pi R}\iint_{S'}\left(\vec{n}\times\vec{E}\right)e^{-jk\left(R-u\left|\cos\alpha\right|\right)} dudw \tag{143}$$

$$\vec{F} = \frac{-2\varepsilon E_0}{4\pi R}\iint_{S'}\left(\vec{n}\times\hat{a}_u\right)E\left(u,w\right)e^{-jk\left(R-u\left|\cos\alpha\right|\right)} dudw \tag{144}$$

$$\vec{F} = \frac{-2\varepsilon E_0 e^{-jkR}}{4\pi R}\iint_{S'}\left(\vec{n}\times\hat{a}_u\right)E\left(u,w\right)e^{-jku\left|\cos\alpha\right|} dudw \tag{145}$$

This double integral can be computed numerically. The constant term $-2\varepsilon/4\pi$ is known; the terms E_0, e^{-jkR}, and $1/R$ can be retained. Denoting the integral and the known multiplicative constants $\overrightarrow{I^c}$, the electric vec tor potential can simply be written as:

$$\overrightarrow{F} = \frac{E_0 e^{-jkR}\overrightarrow{I^c}}{R} \tag{146}$$

$$\overrightarrow{I^c} = \frac{-2\varepsilon}{4\pi}\iint_{S'}\left(\vec{n}\times\hat{a}_u\right)E(u,w)e^{-jku|\cos\alpha|}dudw \tag{147}$$

Here, $\overrightarrow{F}$ and $\overrightarrow{I^c}$ have both θ and ϕ components, each of which is a function of θ and ϕ.

The computed electric vector potential can be used to determine the radiated electric field in the far field by the following relations:

$$E_\theta = -j\omega\eta F_\phi \tag{148}$$

$$E_\phi = -j\omega\eta F_\theta \tag{149}$$

From the electric far field, the total radiated power can be calculated as:

$$P_{rad} = \frac{1}{\eta}\iint_{4\Omega}\left(\left|E_\theta\right|^2 + \left|E_\phi\right|^2\right)R^2 d\theta d\phi \tag{150}$$

$$P_{rad} = \frac{1}{\eta}\iint_{4\Omega}\left(\left|-j\omega\eta F_\phi\right|^2 + \left|j\omega\eta F_\theta\right|^2\right)R^2 d\theta d\phi \tag{151}$$

$$P_{rad} = \omega^2\eta\iint_{4\Omega}\left(\left|\frac{E_0 e^{-jkR}I_\phi^c}{R}\right|^2 + \left|\frac{E_0 e^{-jkR}I_\theta^c}{R}\right|^2\right)R^2 d\theta d\phi \tag{152}$$

$$P_{rad} = \omega^2\eta E_0^2\iint_{4\Omega}\left(\left|I_\phi^c\right|^2 + \left|I_\theta^c\right|^2\right)d\theta d\phi \tag{153}$$

This double integral can be computed numerically. Denoting this integral multiplied by the constants $\omega^2\eta$ as I^d (a scalar), the total radiated power can simply be written as:

$$P_{rad} = E_0^2 I^d \tag{154}$$

$$I^d = \omega^2\eta \iint_{4\Omega} \left(\left| I_\phi^c \right|^2 + \left| I_\theta^c \right|^2 \right) d\theta d\phi \tag{155}$$

This completes the derivation of the radiation from the SIFA's primary slot. The radiation from each of the three slots can simply be added together to determine the SIFA's overall radiation characteristics.

J. Input Impedance

The radiation calculations in the previous two sections allow the input impedance of the SIFA to be calculated fairly easily. Specifically, equation (34), used in the PIFA cavity model, can also be applied to the SIFA:

$$Z_{in} = \frac{\left| V_{in} \right|^2}{P_{rad} + j2\omega\left(W_E - W_M \right)} \tag{156}$$

This equation simply models the SIFA as a leaky cavity. The leaked power is composed entirely of radiation (i.e. the cavity is otherwise lossless); the radiation accounts for the real part of the impedance. The cavity also has time-average electric (W_E) and magnetic (W_M) stored energies due to the fields inside; these account for the imaginary part of the impedance. The input voltage V_{in} is measured at the input to the cavity (i.e. where the coaxial probe enters at the ground plane). The quantities W_E, W_M, and V_{in} need to be determined before equation (156) can be used.

The stored electric and magnetic energies in the SIFA cavity are given by the same volume integrals as listed for the PIFA cavity in equations (35) and (36). The only difference is that these volume integrals need to be tailored to the SIFA's custom coordinate system. Specifically:

$$W_e = \frac{1}{2}\int_{-\frac{\phi_w}{2}}^{\frac{\phi_w}{2}}\int_{\theta_g}^{\pi-\theta_s}\int_{R_i}^{R_o}\epsilon\left|E\right|^2 u^2\cos w\,du\,dv\,dw \tag{157}$$

$$W_m = \frac{1}{2}\int_{-\frac{\phi_w}{2}}^{\frac{\phi_w}{2}}\int_{\theta_g}^{\pi-\theta_s}\int_{R_i}^{R_o}\mu\left|H\right|^2 u^2\cos w\,du\,dv\,dw \tag{158}$$

The limits of integration are simply taken from the boundaries listed for the SIFA cavity in equations (40)-(42). Also, note the presence of the Jacobian $u^2\cos w$. The values for the electric and magnetic fields are taken from the field calculations inside the cavity.

Now the input voltage V_{in} must be determined. For the probe-fed SIFA, this is simply the voltage across the coaxial probe. Specifically, this can be found by multiplying the electric field along the coaxial probe by the actual length of the probe (this is an electric field times a distance, which is a voltage). If h is the height of the probe (which is simply $h = R_o - R_i$) and E_p is the average value of the electric field along the probe, then the input voltage can be calculated simply as:

$$V_{in} = E_p h = E_p\left(R_o - R_i\right) \tag{159}$$

This allows equation (156) to be computed.

K. Numerical Routine and Results

The equations of the SIFA cavity model presented above can be implemented numerically in a coded program [41]. The details of this code are presented in Appendixes A and B. A brief summary of the procedure is as follows. First, the resonant modes are determined in the cavity: equations (55), (57), and (59) are used to determine the modal parameters μ_r, ν_r, and k_d. This requires solving two transcendental equations. Next, for each mode, the modal coefficient in equation (69) is calculated; this allows the modes to be superimposed for the total solution in the cavity, per equation (70). Note that, technically, there are an infinite number of modes; for this numerical procedure, the number of modes must be truncated (i.e. all modes below a certain cut-off frequency). Once the total wave potential solution is known in the cavity, the fields inside the cavity, as well as the radiated fields from each of the radiating slots, can be calculated directly using the appropriate equations. The final step is to calculate the radiated power and input impedance, which can all be done directly.

The numerical results of the cavity method, as applied to the original MICS band SIFA, are presented in Fig. 40. The first plot in the figure shows the VSWR versus frequency curves from four sources for comparison: the cavity model, the transmission line model, the simulated design, and the fabricated design. Note that the cavity method has good agreement with the simulated model, and, in general, is closer to the simulated model than the transmission line model. The resonant frequency predicted by the VSWR curve of the cavity model is much closer to the simulated model than that predicted by the transmission line model.

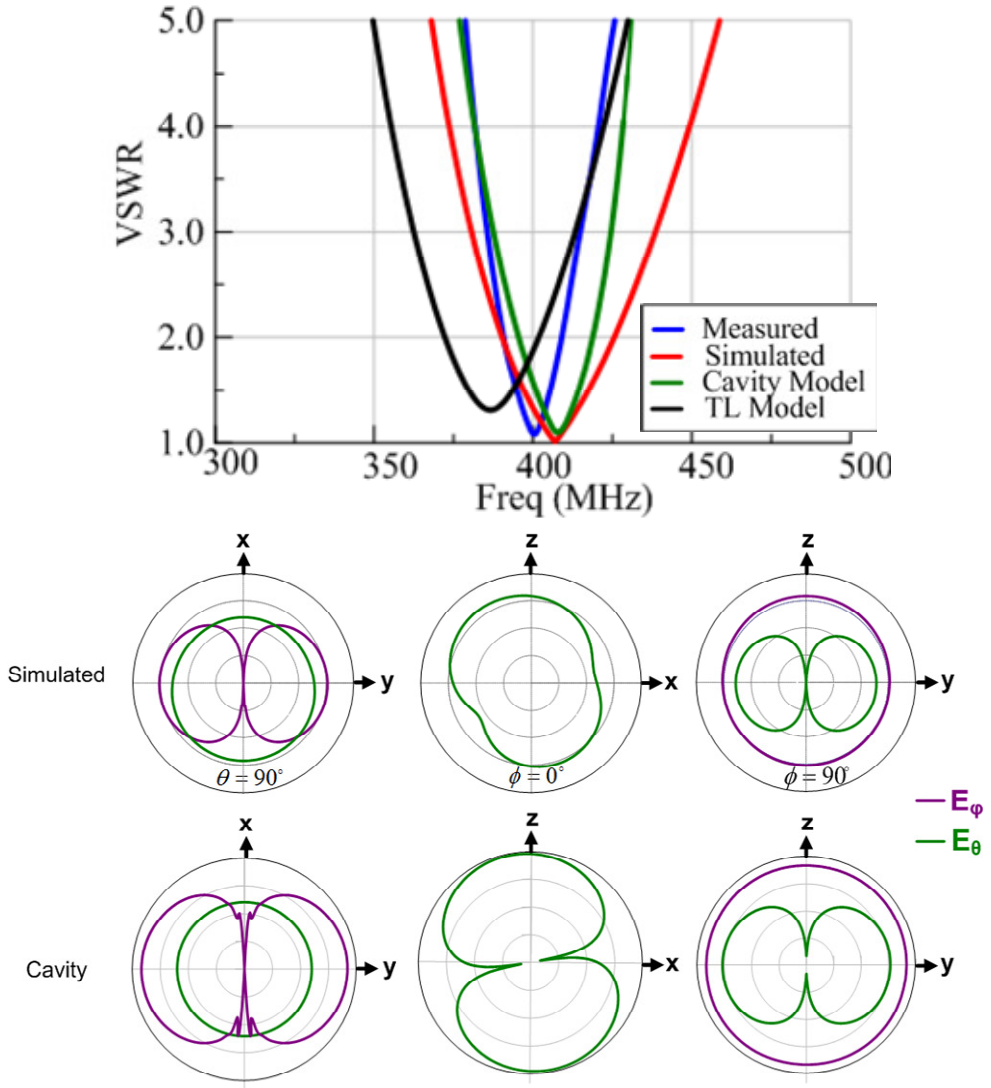

Fig. 40. Results of the SIFA cavity model. For the VSWR plot, the transmission line model, simulated design, and fabricated version of the MICS band SIFA are compared to the cavity model. For the radiation patterns, the simulated design is compared to the cavity model

The second plot in Fig. 40 shows the radiation pattern predicted by the cavity model in comparison to that from the simulated model. The results are again very good. The basic shape of the cavity model's radiation pattern in the three provided cut planes is roughly the same as the simulated model's pattern. The most substantial differences are

in the relative magnitude (strength) of the various polarizations. However, these differences can be simply explained by the cavity model's exclusion of the entire spherical ground plane from consideration; this ground plane will, in general, have an influence shaping the radiation pattern.

Overall, the results demonstrate the legitimacy of the new SIFA cavity model, and, furthermore, they suggest that the cavity method can provide more accurate predictions of the SIFA's performance than the much simpler transmission line model. If nothing else, the cavity model provides more physical insight into operation of the SIFA's patch simply by accounting for the antenna's unique geometry. The cavity method represents another step in the analytical treatment of the SIFA.

CHAPTER VI

THE SIFA IN A REMOTE NETWORK SCENARIO

A. General Considerations for Remote Networking

One possible and promising application of the SIFA is in a remote network. In this scenario, a number of SIFAs could be deployed into a remote environment for telemetric, communication, or other purposes. Each SIFA would thus serve as a single node in an *ad hoc* network. The SIFAs would complete be self-supporting packages, with their own onboard power, communication, and sensing systems. Ideally, this network would be able to remain in such a remote setting more or less indefinitely with little to no maintenance necessary. Furthermore, it would be desirable to make the SIFAs capable of harvesting their own power, through solar or other means.

The SIFA provides a good candidate for such remote operation for several reasons. First, the SIFA design itself provides a structural platform on which other electronic devices in an integrated system can be mounted. Specifically, approximately three-quarters of the interior of the sphere (inside the ground plane) as well as three-quarters of the outside surface area of the sphere are free space in which to mount other devices. The inside of the sphere, in particular, provides prime space for other devices, since it is electrically isolated from the antenna by the ground plane. This characteristic of the SIFA would allow it to be developed into a complete self-supporting package, with its own power, sensing, and communication equipment.

The second positive characteristic of the SIFA for remote operation is that it could allow for rapid deployment of a network. If all of components of the SIFA were contained completely inside the spherical ground plane in a structurally rigid package, each SIFA could literally be thrown out into the desired environment like a ball. This deployment could even be done from a moving vehicle: a truck on the ground or a low-flying airplane or helicopter. In any case, an *ad hoc* network could be deployed and operational in a very short span of time.

The final characteristic of the SIFA that makes it a good candidate for remote operation is its potential for solar power harvesting. The ability to collect its own energy would be hugely advantageous to making a long-term self-sustaining network of SIFAs. Having a spherical, shape, the SIFA provides a unique opportunity to collect solar radiation efficiently. Fig. 41 demonstrates this potential by comparing a spherical solar collector to a planar solar collector operating above ground. The spherical shape provides the best opportunity to collect radiation because not only does it receive rays directly from the sun, but it also can receive reflected rays off of the ground [e.g. 42].

The primary design challenge presented by this remote network scenario – from an antenna engineering perspective, at least – would be the randomness of the environments that the SIFA is exposed to. Each different environment would have its own specific dielectric properties, lossy properties, as well as multipath, fading, and shadowing characteristics. As each SIFA would be resting on the ground in the presence of a lossy dielectric material, the free-space radiation and propagation characteristics of the SIFA would be irrelevant. To further complicate the situation, if the SIFAs were

deployed rapidly (i.e. tossed like a ball into the environment, as described previously), each node would be resting in a random orientation above the ground; in fact, a SIFA might even become partially buried under the ground. All of these factors would have a direct effect on antenna parameters such as input impedance, radiation efficiency, and polarization efficiency, as well as propagation characteristics. Ideally, the SIFA should not have to be redesigned to cope with varying environments. In this case, reliable node-to-node communication would have to be ensured despite such random environments and orientations.

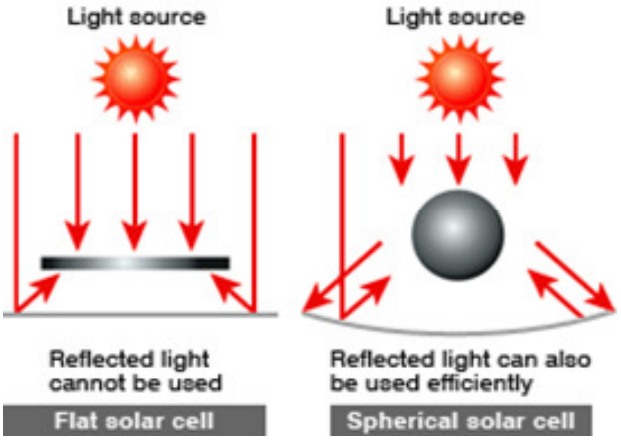

Fig. 41. Solar collection of a spherical cell vs. a flat cell. Picture available at http://www.kyosemi.co.jp/product/pro_ene_sun_e1.html

B. Two-Node LOS Remote Network Scenario

One to determine if the SIFA could work effectively in a remote scenario would be to simulate its performance in that environment. However, it would be next to impossible to determine how the SIFA performs in every type of remote environment. There are simply too many variables: dielectric properties of the earth, terrain profile, as

well as objects like trees, bushes, and rocks. To demonstrate this wide diversity, Table 3 provides a list of a number of materials commonly found in the ground, along with their relative dielectric constants and dielectric loss tangents. The purpose of the simulation work that follows is not to exhaust all of the possibilities for remote environments; it is simply to provide a broad overview of how the SIFA might perform and some of the design factors to look for when considering remote operation.

Table 3. Dielectric properties of various materials found in the earth

Material	Permittivity	Loss Tangent
Dry Sand	3-5	0.01
Saturated Sand	20-30	0.1-1.0
Limestone	4-8	0.5-2
Shales	5-15	1-100
Silts	5-30	1-100
Clays	5-40	2-1000
Granite	4-6	0.01-1
Dry Salt	5-6	0.01-1

To test the effectiveness of the SIFA in a remote network scenario, a simple simulation scenario was devised to test the SIFA's performance in a two-node communication link scenario in the presence of a dielectric ground. Fig. 42 summarizes such a scenario. Two SIFAs (one a transmitter, the other a receiver) are placed at a height h above a lossy dielectric ground (with unknown properties ε_r and $\tan\delta$), with a distance of R between them. The ground is assumed to be flat so that a line-of-sight

(LOS) link exists between the antennas. For simplicity, multipath is ignored such that this LOS link is the only link between the antennas. Also, both antennas are assumed to be randomly oriented above the ground, rotated around two axes to a specific position, as shown by the rotation arrows. This accounts for the randomness introduced if the SIFAs are rapidly deployed by throwing them like balls into the environment. Finally, no fading or shadowing is considered here. Although this scenario is fairly simplistic, it provides a first step in analyzing remote operation for the SIFA.

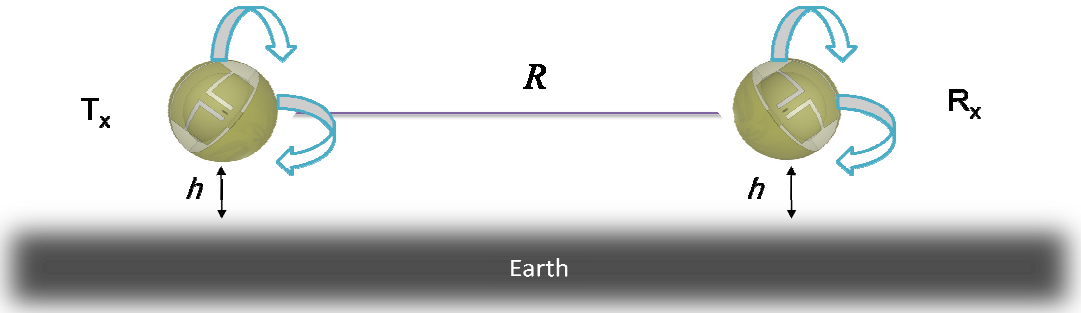

Fig. 42. Two-node LOS communication link between SIFAs. The orientation of each SIFA is random, and each SIFA lies above the ground by a height *h*

The best way to evaluate this two-node LOS SIFA link is in a statistical sense. Specifically, if both the transmitting and the receiving SIFAs are rotated in place independently above the ground into different orientations – each orientation being equally likely in a statistical sense – then the data from all of the possible orientations can be compiled and summarized into statistical distributions, such as probability density functions. The statistical distributions can demonstrate how predictably (as well as how efficiently) the SIFA would perform given random orientations of both transmitter and

receiver. Furthermore, the dielectric properties of the ground can be changed to compare these statistical distributions in different dielectric environments.

C. Simulation Technique

The two-node LOS scenario introduced above is a somewhat abstract description. The actual implementation of this scenario is performed using electromagnetic software simulation [27] followed by computations with a program coded in [41]. Specifically, the antenna is simulated for its radiation characteristics, and then a program is used to calculate the power transfer between the transmitter and receiver. The program is also used to determine the statistical distributions describing the performance for various orientations.

The independent rotation of both the transmitter and receiver can be achieved by rotating only one simulated SIFA design and using the data from that simulation for both antennas. The simulated SIFA design is placed above a flat ground, as shown in Fig. 43. It is then rotated in 18° increments around two axes, for a total of 400 different orientations. For each orientation, the SIFA is simulated, and the following data is recorded: input impedance (referenced to 50 Ω), radiation efficiency, and radiation pattern (a full 360° pattern).

The data from these simulations of a single SIFA can be used for both the transmitter and receiver in the two-node link scenario. Each antenna is assumed to have a local reference coordinate system exactly the same as shown in Fig. 11; these coordinate systems remain fixed as each antenna rotates independently. Since only a

LOS link is required, only a single value from the three-dimensional radiation pattern is needed for both the transmitter and receiver. Specifically, the field value at $\theta = 90^{\circ}$ and $\phi = 90^{\circ}$ is taken for the transmitter and the field value at $\theta = 90^{\circ}$ and $\phi = 270^{\circ}$ is taken for the receiver. This extraction of field pattern data is done for each rotation of the antenna. Along with the radiation pattern data (field intensity and gain) in these two directions, the impedance and radiation efficiency for each rotation is recorded (these quantities are always the same for the transmitter and receiver). Once data is recorded for all 400 orientations of a single antenna in the simulation, the coded program can be used to extend these possible orientations to both transmitter and receiver. If both antennas can assume any of the 400 orientations independently, then a total of 160,000 transmitter-receiver orientations are possible. A number of calculations are then performed in the program for each of these 160,000 possibilities; these calculations are described in the following section.

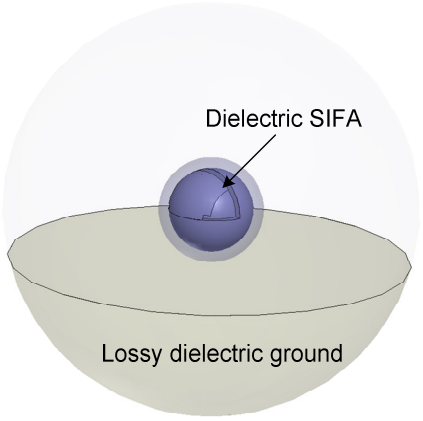

Fig. 43. Simulation of a SIFA operating in the presence of a lossy ground

D. LOS Link Calculations

The governing equation for the power transfer between the two SIFAs in the LOS link scenario described above can be written as:

$$P_r = P_t G_t(\Omega) G_r(\Omega)\left(1-|\Gamma_t|^2\right)\left(1-|\Gamma_r|^2\right)\eta_t^{rad}\eta_r^{rad}\eta^{pol}\left(\frac{\lambda}{4\pi R}\right)^n e^{-\alpha n R} \qquad (160)$$

This is essentially a Frii's transmission scheme (e.g. as in [40]). Here, P_t is the power transmitted, and P_r is the received power. $G_t(\Omega)$ and $G_r(\Omega)$ are the gains of the transmitter and receiver, respectively; these are a function of the spherical angle $\Omega=(\theta,\phi)$. Γ_t and Γ_r are the reflection coefficients of the respective antennas, with $\left(1-|\Gamma|^2\right)$ being the coefficient by which these reflections reduce the power. η_t^{rad} and η_r^{rad} are the radiation of the transmitter and receiver. The polarization efficiency, given by η^{pol}, combines the effects of both the transmitter and receiver and is thus not split into two quantities. The term $(\lambda/4\pi R)^n$ accounts for the path loss of the signal as it travels a distance R between the antennas. In the case of this scenario, where multipath is not considered, the exponential factor n is simply equal to 2; multipath can easily be added to the scenario by changing n, but this work will not pursue this possibility. Finally, any propagation loss is accounted for by the exponential term $e^{-\alpha n R}$; however, if air is assumed to be the propagation media, then this loss in negligible and the whole term can be reduced to unity. This assumption of negligible propagation loss will be used here.

For each of the 160,000 possible orientations of the transmitter and receiver, equation (160) is applied to the scenario to determine the power transfer between the

antennas. For all of the simulations in this work, the transmitted power is assumed to be 100 W, and the distance between the antennas is chosen as 100 m. These are arbitrary values. The gain and the radiation efficiency of the antennas are taken directly from the simulations. The reflection coefficients are simply calculated using the VSWR values from the simulations via the following formula:

$$\Gamma = \frac{VSWR - 1}{VSWR + 1} \tag{161}$$

The polarization efficiency is a slightly more involved calculation [43]. It is calculated in (162).

$$\eta^{pol} = \frac{1 + |p_t|^2 |p_r|^2 + 2|p_t||p_r|\cos(\delta_t - \delta_r)}{\left(1 + |p_t|^2\right)\left(1 + |p_r|^2\right)} \tag{162}$$

Here, p_t and p_r are the magnitudes of the polarization ratios of the transmitter and receiver, respectively, and δ_t and δ_r are the corresponding phases of these ratios. The polarization ratio is the ratio of the phi component of the electric field to the theta component:

$$p = \left| \frac{E_\phi(\Omega)}{E_\theta(\Omega)} \right| \tag{163}$$

Obviously, the electric field components are dependent on the orientation Ω. The electric field values are taken directly from the simulations.

Once equation (160) is applied to all of the possible orientations, the data is ready to be analyzed statistically. The first step in this process is to compile cumulative distribution functions (CDFs) of the following antenna parameters: received power,

VSWR, radiation efficiency, and polarization efficiency. Again, these distributions are made assuming that all 160,000 orientations of transmitter and receiver are equally likely statistically. Practically, the CDFs are calculated by choosing an appropriate range for the antenna parameter (e.g. the polarization efficiency range is 0 to 1); dividing that range into discrete steps; for each discrete value in the range, counting the number of orientations for which the desired antenna parameter is less than or equal to that discrete value; and dividing the number of counted orientations at each discrete value by the total number of orientations. This method essentially constructs the CDF using its statistical definition.

Once the CDFs are found for the desired quantities, the corresponding probability functions (PDFs) can be computed. By definition, the PDF is simply the derivative of the CDF. The PDFs perhaps provide the best way to visualize the data, showing what values of received power, VSWR, radiation efficiency, and polarization efficiency are most likely, as well as how concentrated or spread out the distribution of these quantities are.

E. Uncoated vs. Coated SIFA

It is of significant interest to compare the performance of the original uncoated SIFA design to a coated design in the two node link scenario described above. The coated design promises many possible advantages. First, a durable coating can provide a physical advantage: protection of the antenna from harsh environmental conditions, as well as structural rigidity, if the right materials are used. Second, a coating can provide

electromagnetic advantages: if the coating is made out of a high dielectric material, it will minimize the adverse effects of being in the presence of unknown dielectric surroundings; if the coating is also slightly lossy, then the predictability of the antenna's performance can be improved. These advantages will occur because with a lossy dielectric coating, the SIFA's bandwidth will be improved, and the antenna will be less likely to detune as the outside environment changes; the resonant characteristics of the antenna will remain more stable at the desired operating frequency.

There are many possibilities for what coated design to use to compare to the original SIFA; the design could resonate at the same frequency, be the same physical size, be the same electrical size, etc. For the purposes of this work, a coated design is chosen such that the outer radius of the SIFA structure (not including the coating) is the same size as the original SIFA. Specifically, the design introduced in Chapter III is used. A coating of 2.5 cm is added around the SIFA. The coating, as well as the substrate under the patch, is given a relative dielectric constant of $\varepsilon_r = 50$. The antenna is tuned to operate at around 75 MHz. The dimensions, operating frequencies, and electrical sizes of the original SIFA and this coated design are compared in Fig. 44.

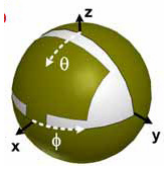

Uncoated Design:
- Radius = 10.16 cm
- Foam substrate approximated as a vacuum
- Nominally inefficient radiation (electrically small)
- Resonance ~ 400 MHz
- Electrical size: *ka* = 0.88

Coated Design:
- Radius = 10.16 cm
- 2.5 cm coating and substrate with ε_r = 50
- Very inefficient radiation (more electrically small)
- Resonance ~ 75 MHz
- Electrical size: *ka* = 0.2

Fig. 44. Comparison of coated and uncoated designs used for remote LOS link simulations

Both the uncoated and the coated design are used in the two-node link simulation, under identical conditions. The dielectric properties of the ground, as well as the dielectric loss tangent of the coated SIFA's coating, are varied. The results of these simulations are discussed in the following section.

F. Simulation Results

The simulations and calculations described in the preceding sections for a two-node LOS SIFA link were performed several times over. Each iteration of the process involved a different combination of the following values: dielectric loss tangent of the SIFA coating, relative dielectric constant of the ground, and dielectric loss tangent of the ground. Table 4 lists these different iterations. The goal of varying these values was to obtain a simplistic view of how they might affect the SIFA's performance in this two-node scenario; again, they are not meant to provide an exhaustive study of the SIFA's remote functioning capabilities.

Table 4. Simulation variations for remote LOS link scenario

Simulation	Loss tangent of SIFA coating/substrate	Relative dielectric constant of ground	Loss tangent of ground
Simulation 1	0.02	5	1.1
Simulation 2	0.02	15	1.1
Simulation 3	0.1	5	1.1

The results of Simulation 1 are shown in Fig. 45. Specifically, the PDF's of the VSWR, received power, polarization efficiency, and radiation efficiency are given. The PDF of VSWR indicates that the coated design maintains a very small impedance mismatch (i.e. a VSWR well below 2); the VSWR of the uncoated design is much more distributed across the given range of 1 to 5. This is a clear operational advantage of the coated design: regardless of the orientation, it is able to maintain a very good impedance match in the presence of a lossy ground. This feature is unattainable with the uncoated design.

The next plot of interest in Fig. 45 is the PDF of the received power. Both the coated and uncoated designs demonstrate fairly concentrated distributions, with the coated design being slightly more concentrated. However, the averaged received power for the coated design is significantly less than for the uncoated design. This is expected, though, since the coated design is plagued by the loss of the dielectric coating and substrate. Depending upon the demands of a specific application, this reduction of received power could be a fairly heavy price to pay for a relatively low improvement in the concentration (i.e. the predictability) of the received power.

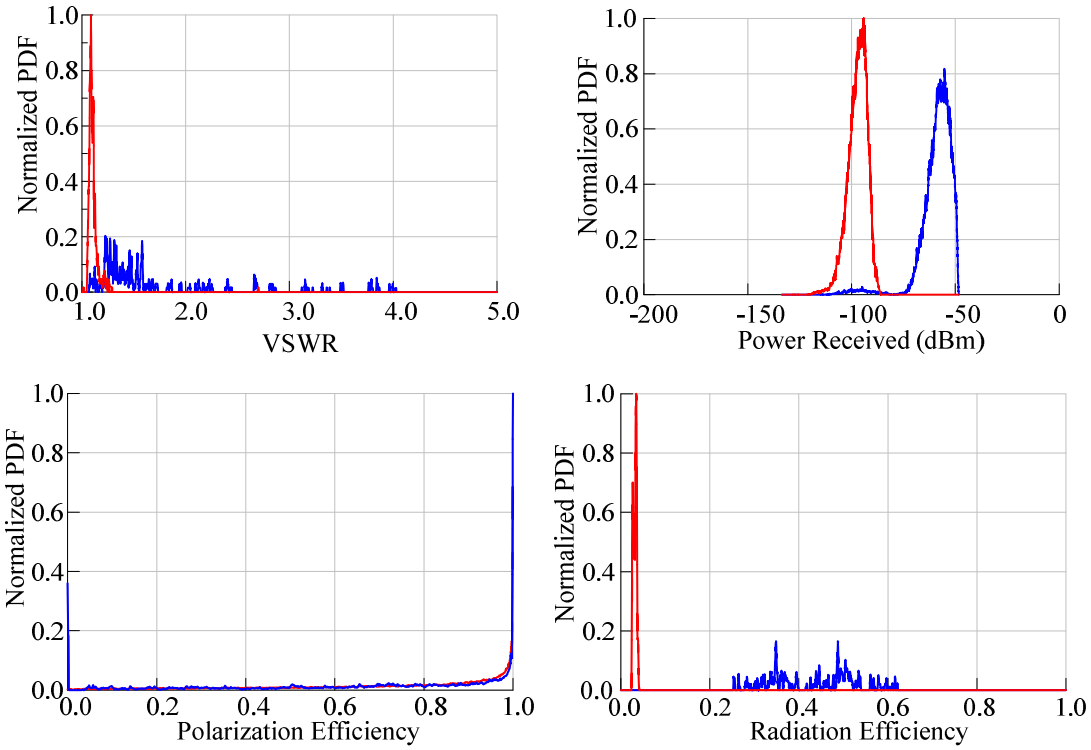

Fig. 45. Simulation 1 results (remote LOS link). Coated design in red, uncoated design in blue

The PDF of the radiation efficiency in Fig. 45 demonstrates an interesting tradeoff between the two designs. The coated design shows significantly lower radiation efficiency than the uncoated design. Again, this is largely due to the lossy coating and dielectric; an additional factor is the naturally lower efficiency of an electrically smaller design. However, the coated design is much more concentrated in its distribution, meaning that this particular antenna performance metric is very predictable compared to the uncoated design; this could be very advantageous in designing a reliable remote network. Thus, the two designs offer a tradeoff in terms of efficiency on the one hand and predictability on the other hand.

The final plot in Fig. 45 is the PDF of polarization efficiency. There is no discernible difference between the two distributions, and both show very high efficiencies. This is due mainly to the omnidirectional qualities of the SIFA's radiation patterns (both in the θ and ϕ polarizations). However, this particular quantity does not provide a distinguishing feature between the two designs.

The results of Simulation 2 are shown in Fig. 46. For this simulation, the relative dielectric constant of the ground was increased by three times. The results are fairly similar to the Simulation 1 results in Fig. 45, and the same general conclusions can be drawn.

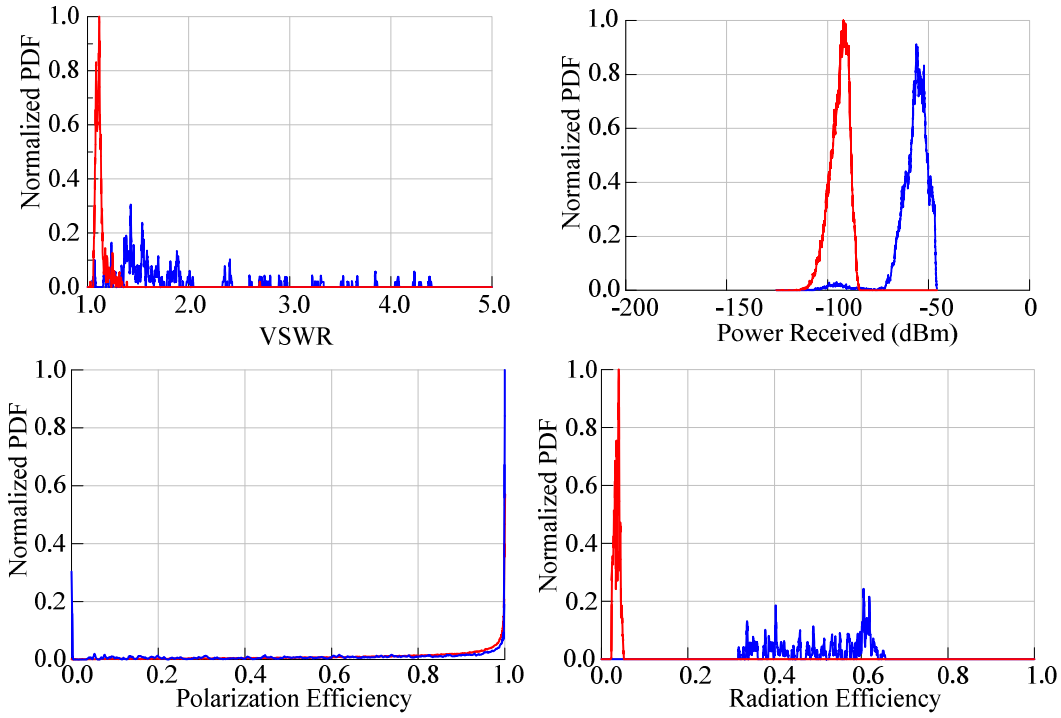

Fig. 46. Simulation 2 results (remote LOS link). Coated design in red, uncoated design in blue

The results of Simulation 3 are shown in Fig. 47. For this simulation, the loss tangent of the coating and substrate was increased by five times in order to see how a more lossy coating would affect the performance of the coated design. Again, the results are similar to those in both Fig. 45 and Fig. 46. There are only two noticeable (but minor) differences. First, the PDF of VSWR for the coated design was shifted to even lower values (i.e. the impedance match was even better than for the previous simulations). Clearly, increasing the loss of the coating and substrate helps to maintain the impedance match as the antenna orientation changes. Second, the radiation efficiency of the coated design was shifted further down in value from the previous simulations; this is to be expected, though, since the loss of the coating and substrate was increased.

In summary, a number of observations and conclusions can be drawn from the simulations of a 2-node LOS SIFA link in a remote network scenario. The coated and uncoated designs come with tradeoffs as far as desirable networking qualities are concerned. The coated design clearly tends to increase the predictability of various performance parameters, especially the radiation efficiency and impedance match. This makes the coated design a favorable choice if the dependability of a network were crucial. However, this increased predictability comes at the cost of less efficiency as compared to the uncoated design. If received power thresholds were crucial to a network design, the coated SIFA may not be as desirable. However, the coated design simulated here is only one of a myriad of possible designs. For practical applications, the dielectric properties of the coating could theoretically be optimized to yield the right balance between the competing interests of predictability and efficiency. The coated design here

is by no means intended to represent an optimal design. It was useful, however, in determining the general operating principles of the dielectric SIFA as compared to the uncoated SIFA. Future work could center on optimizing the coating for specific applications.

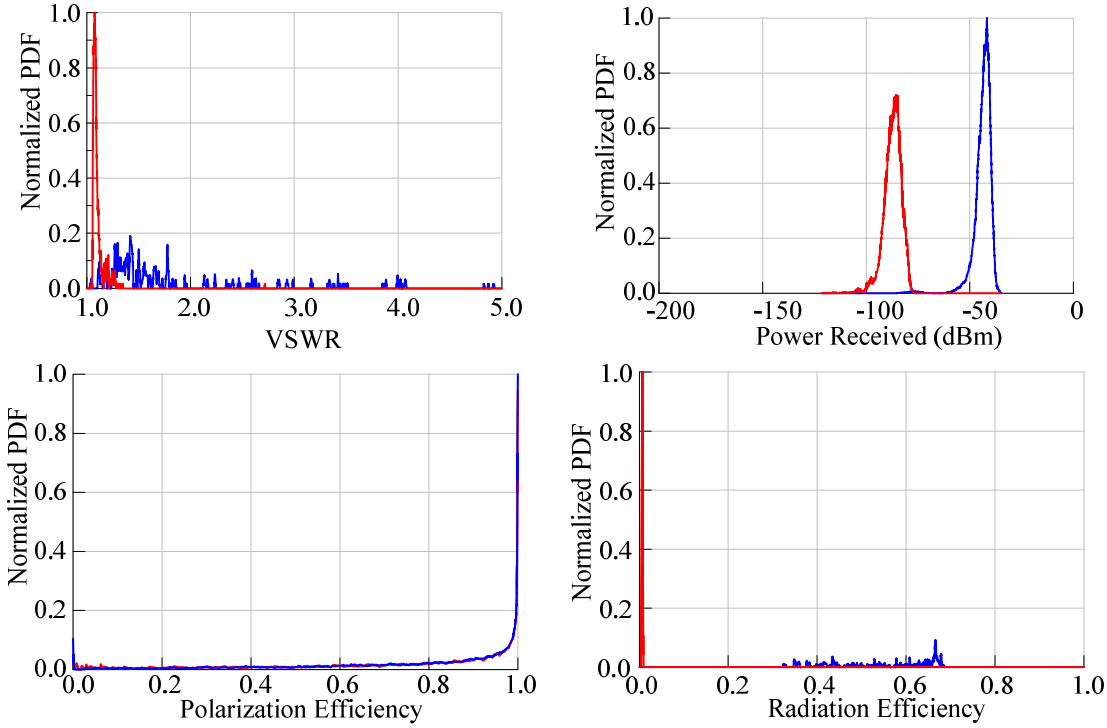

Fig. 47. Simulation 3 results (remote LOS link). Coated design in red, uncoated design in blue

CHAPTER VII

CONCLUSION

This work extends the understanding of a recently developed conformal antenna design, the spherical inverted-F antenna. A new analytical model employing the cavity method describes the antenna in a much more rigorous manner than the previous transmission line model approximation could do. A dielectric SIFA fabrication demonstrates the viability of constructing the SIFA with a coating. Analysis of the SIFA – both of the coated and uncoated variety – in a remote network scenario indicates a tradeoff between the designs in terms of predictability and efficiency. All of these developments lead to further possibilities for future work.

In terms of analytical treatment of the SIFA, much more can be done. First, neither the transmission line model nor the cavity model takes into account the effect of the full spherical ground plane of the SIFA. In future work, this could possibly be accomplished by considering the characteristic modes of this ground structure. Also, as of yet, there is no extension of the analytical models to include a dielectric coating; the dielectric SIFA remains completely unexplored analytically. One approach that could be used is to consider the coating as a spherical dielectric resonator excited by the patch structure beneath it. Finally, there is no consolidated analytical design process for the SIFA; all designs to this point, have, at least to some extent, been heuristic in nature. Development of a standard and simple design method would go very far to making the SIFA an attractive option for commercial pursuits.

Fabrication methods provide another promising frontier for future work on the SIFA. The basic functionality of this antenna has already been successfully demonstrated with relatively basic hand fabrication methods. Better fabrication materials and techniques would facilitate the adoption of the SIFA into real-world applications. Also along the lines of fabrication, work should be done to consider how the SIFA might be packaged with other devices in an integrated system. One of the SIFA's chief values is the possibilities it presents as a multifunctional structure; however, in order to realize this potential, work has to be carried beyond the stage of simple antenna engineering.

Remote networking has certainly been demonstrated as a likely multifunctional application of the SIFA. However, the understanding of the dielectric-coated SIFA and its performance in remote environments is still only elementary. In order for this application to be realized, more work needs to be done on optimizing the dielectric properties of the SIFA coating to achieve the desired balance between efficiency and predictability in the presence of changing environments. Furthermore, analysis of multipath, shadowing, and other properties of communication channels is necessary to form a more complete picture of how the SIFA could work in remote networking.

REFERENCES

[1] S. R. Saunders and A. Aragon-Zavala, *Antennas and Propagation for Wireless Communication Systems,* 2nd ed. Chichester, UK: John Wiley & Sons, Inc., 2007.

[2] H. Meikle, *Modern Radar Systems,* 2nd ed. Norwood, MA: Artech House, Inc., 2008.

[3] L. Sevgi, "The antenna as a transducer: Simple circuit and electromagnetic models", *IEEE Antennas Propag. Mag.*, vol. 49, no. 6, pp. 211-218, Dec. 2007.

[4] A. Zhao, J. Xue, C. Jing, and A. Salo, "The use of Murata ceramic Bluetooth antenna for wrist device based on flexible printed circuit boards", in *Proc. 38th European Microwave Conf.*, Amsterdam, Netherlands, Oct. 2008, pp. 1755-1758.

[5] S. D. Targonski and D. M. Pozar, "Analysis and design of a microstrip reflectarray using patches of variable size", in *Antennas Propag. Soc. Int. Symp.*, Seattle, WA, June 1994, pp. 1820-1823.

[6] Y. T. Lo and S. W. Lee, *Antenna Handbook: Applications,* vol. 3. New York: Chapman & Hall, 1993.

[7] C.-M. Lee, T.-C. Yo, C.-H. Luo, C.-H. Tu, and Y.-Z. Juang, "Compact broadband stacked implantable antenna for biotelemetry with medical devices", *Electron. Lett.*, vol. 43, no. 12, pp. 660-662, June 2007.

[8] S. Lindenmeier, J. F. Luy, and P. Russer, "A multifunctional antenna for terrestrial and satellite radio applications", in *IEEE MTT-S Int. Microw. Symp. Dig.*, Phoenix, AZ, May 2001, pp. 393-396.

[9] Y. T. Lo, D. Solomon, and W. F. Richards, "Theory and experiment on microstrip antennas", *IEEE Trans. Antennas Propag.*, vol. 27, no. 2, pp. 137-145, March 1979.

[10] J. R. James, P.S. Hall, and C. Wood, *Microstrip Antenna Theory and Design.* London, UK: Peter Peregrinus Ltd., 1981.

[11] R. A. Burberry, *VHF and UHF Antennas*. London, UK: Peter Peregrinus Ltd., 1992.

[12] D. E. Anagnostou, G. Zheng, S. E. Barbin, M. T. Chryssomallis, J. Papapolymerou, and C. G. Christodoulou, "An X-band reconfigurable planar dipole antenna", in *SBMO/IEEE MTT-S Int. Conf. Microw. Opt.*, Brasilia, Brazil, July 2005, pp. 654-656.

[13] Y. Kim and E. K. Walton, "Automobile conformal antenna design using non-dominated sorting genetic algorithm (NSGA)", *IEE Proc. Microw. Antennas Propag.*, vol. 153, no. 6, pp. 579-582, Dec. 2006.

[14] S. Nikolaou and D. E. Anagnostou, "Conformal antenna on LCP for sensor applications", in *Antennas Propag. Soc. Int. Symp.,* San Diego, CA, July 2008, pp. 1-4.

[15] P. S. Neelankanta and R. Chatterjee, *Antennas for Information Super Skyways: An Exposition on Outdoor and Indoor Wireless Antennas*. Hertfordshire, UK: Research Studies Press Ltd., 2003.

[16] G. H. Huff and J. J. McDonald, "A spherical inverted-F antenna (SIFA)", *IEEE Antennas Wireless Propag. Lett.*, vol. 8, pp. 649-652, May 2009.

[17] K. Fujimoto, *Mobile Antenna Systems Handbook,* 3rd ed. Norwood, MA: Artech House, Inc., 2008.

[18] J. J. McDonald, "Analysis, design, and operation of a spherical inverted-F antenna", M.S. Thesis, Texas A&M University, College Station, TX, May 2008.

[19] D. K. Cheng, *Fundamentals of Engineering Electromagnetics*. Reading, MA: Addison-Wesley Publishing Company, Inc., 1993.

[20] R. F. Harrington, *Time Harmonic Electromagnetic Fields*. New York: John Wiley and Sons, Inc., 2001.

[21] C. A. Balanis, *Antenna Theory: Analysis and Design,* 3rd ed. Hoboken, NJ: John Wiley & Sons, Inc., 2005.

[22] R.C. Johnson and H. Jasik, *Antenna Engineering Handbook*. New York: McGraw-Hill, 1984.

[23] K.-L. Wong, *Design of Nonplanar Microstrip Antennas and Transmission Lines*. New York: John Wiley & Sons, Inc., 1999.

[24] M. Kanghou and X. Menglin, "A study of conformal microstrip antenna array on a cylinder", in *5th Int. Symp. Antennas, Propag., and EM Theory,* Beijing, August 2000, pp. 18-21.

[25] K. Zhang, Q. Zhang, C. Guo, and J. Xu, "Analysis of conformal Sierpinski fractal microstrip antenna", in *Int. Conf. Microw. and Millimeter Wave Tech.*, Nanjing, April 2008, pp. 1106-1109.

[26] D. M. Pozar and D. Schaubert, *Microstrip Antennas: The Design and Analysis of Microstrip Antennas and Arrays*. Hoboken, NJ: John Wiley & Sons, Inc., 1995.

[27] HFSS ver. 9.1, Ansoft, Pittsburgh, PA.

[28] R. Garg, *Microstrip Antenna Design Handbook*. Norwood, MA: Artech Publishing House, 2001.

[29] K. A. Bakshi, A. V. Bakshi, and U. A. Bakshi, *Antennas and Wave Propagation*. Shaniwar Peth, India: Technical Publications Pune, 2009.

[30] J. M. Golio, *The RF and Microwave Handbook: RF and Microwave Passive and Active Technologies,* 2nd ed. Boca Raton, FL: Taylor & Francis Group, 2008.

[31] T.-F. Chien, "Develop CPW-fed monopole broadband implantable antennas on the high dielectric constant ceramic substrates", *Microw. and Optical Tech. Lett.*, vol. 52, no. 9, pp. 2136-2139, Sept. 2010.

[32] J. Volakis, C.-C. Chen, and K. Fujimoto, *Small Antennas: Miniaturization Techniques & Applications*. New York: McGraw-Hill, 2010.

[33] J. McDonald and G. H. Huff, "Design and packaging of a spherical inverted-F antenna (SIFA) for biomedical applications", presented at 2008 IEEE Int. Symp. Antennas and Propag., San Diego, CA, June 2008.

[34] A. Van Gossum, M. Munoz-Navas, I. Fernandez-Urien, C. Carretero, G. Gay, M. Delvaux, M. G. Lapalus, T. Ponchon, H. Neuhaus, M. Philipper, G. Costamagna, M. E. Riccioni, C. Spada, L. Petruzziello, C. Fraser, A. Postgate, A. Fitzpatrick, F. Hagenmuller, M. Keuchel, N. Schoofs, and J. Deviere, "Capsule endoscopy versus colonoscopy for the detection of polyps and cancer", *New England Journal Medicine*, vol 361, no. 3, pp. 264-270, July 2009.

[35] OOMOO^{TM} Silicone Rubber, Reynolds Advanced Materials, Dallas, TX. Available: http://www.reynoldsam.com/

[36] M. Lazebnik, E.L. Madsen, G.R. Frank, and S.C. Hagness, "Tissue-mimicking phantom materials for narrowband and utrawideband microwave applications", *Physics in Medicine and Biology*, vol. 50, no. 18, pp. 4245-4258, Aug. 2005.

[37] Y. Nikawa, M. Chino, and K. Kikuchi, "Soft and dry phantom modeling material using silicone rubber with carbon fiber", *IEEE Trans. Microw. Theory and Techniques,* vol. 44, no. 10, pp. 1949-1953, October 1996.

[38] V. I. Piercey, "The Lamé and metric coefficients for curvilinear coordinates in $\mathbb{R}^3$", unpublished, Nov. 2007. Available: http:/ odessa.phy.sdsmt.edu/~andre/

[39] L. A. Costa, O. M. C. Pereira-Filho, and F. J. S. Moreira, "Analysis of spherical-rectangular microstrip antennas", in *SBMO/IEEE MTT-S Int. Conf. Micorw. And Optoelectronics*, Brasilia, Brazil, July 2005, pp. 279-282.

[40] W. L. Stutzman and G. A. Thiele, *Antenna Theory and Design*, 2nd ed. Hoboken, NJ: John Wiley & Sons, Inc., 1998.

[41] Matlab Student ver. 7.1, Math Works, Natick, MA.

[42] T. Rodziewicz, J. Nakata, K. Taira, I. Inagawa, M. Waclawek, and A. Zaremba, "Performance of Sphelar® module at outdoor conditions in higher latitude areas", in *23rd European Photovoltaic Solar Energy Conf. Exhibition*, Valencia, Spain, Sept. 2008, pp. 596-599.

[43] T. A. Milligan, *Modern Antenna Design,* 2nd ed. Hoboken, NJ: John Wiley & Sons, Inc., 2005.

APPENDIX A

NUMERICAL CALCULATION OF SCHELKUNOFF-TYPE SPHERICAL BESSEL FUNCTIONS OF FRACTIONAL ORDER AND ASSOCIATED LEGENDRE FUNCTIONS OF FRACTIONAL ORDER AND DEGREE

A. Introduction

The Schelkunoff-type spherical Bessel functions and associated Legendre functions used in the modal calculations of the SIFA cavity model can only be calculated numerically. The calculations are further complicated because modal solutions to the wave equation in the cavity dictate that the functions have fractional orders and degrees. A brief description of the numerical routines used to compute these functions, along with their derivatives, follows. Then, the Matlab code used to implement these routines is provided.

B. Associated Legendre functions

The associated Legendre functions of fractional order and degree (i.e. $P_{\nu_r}^{\mu_r}$ and $Q_{\nu_r}^{\mu_r}$) can be calculated in the form of an infinite series (i.e. a series solution to the Legendre differential equation). This series is simply an infinite polynomial of the form:

$$y = a_0 + a_1 x + a_2 x^2 + \ldots + a_k x^k \tag{164}$$

In other words,

$$y = \sum_{k=0}^{\infty} a_k x^k \tag{165}$$

This method works for functions of both the first and second kinds. The coefficients a_k are determined through a numerical recurrence relation:

$$a_{k+2} = \frac{\left[\mu_r{}^2 + 2k^2 - \nu_r\left(\nu_r+1\right)\right]a_k + \left[\left(k-2\right)\left(1-k\right)+\nu_r\left(\nu_r+1\right)\right]a_{k-2}}{\left(k+1\right)\left(k+2\right)} \tag{166}$$

To begin calculation of this recurrence formula, the initial coefficients are given as:

$$a_{-1} = 0 \tag{167}$$

$$a_{-2} = 0 \tag{168}$$

The initial coefficients a_0 and a_1 depend on whether the Legendre function is of the first or second kind. Specifically, for $P_{\nu_r}^{\mu_r}$:

$$a_0 = \frac{2^{\mu_r}}{\sqrt{\pi}}\cos\left(\frac{\pi}{2}\left(\nu_r+\mu_r\right)\right)\frac{\Gamma\left(\frac{\nu_r+\mu_r+1}{2}\right)}{\Gamma\left(\frac{\nu_r-\mu_r+2}{2}\right)} \tag{169}$$

$$a_1 = \frac{2^{\mu_r+1}}{\sqrt{\pi}}\sin\left(\frac{\pi}{2}\left(\nu_r+\mu_r\right)\right)\frac{\Gamma\left(\frac{\nu_r+\mu_r+2}{2}\right)}{\Gamma\left(\frac{\nu_r-\mu_r+1}{2}\right)} \tag{170}$$

For $Q_{\nu_r}^{\mu_r}$:

$$a_0 = -2^{\mu_r-1}\sqrt{\pi}\sin\left(\frac{\pi}{2}\left(\nu_r+\mu_r\right)\right)\frac{\Gamma\left(\frac{\nu_r+\mu_r+1}{2}\right)}{\Gamma\left(\frac{\nu_r-\mu_r+2}{2}\right)} \tag{171}$$

$$a_1 = 2^{\mu_r}\sqrt{\pi}\cos\left(\frac{\pi}{2}\left(\nu_r+\mu_r\right)\right)\frac{\Gamma\left(\frac{\nu_r+\mu_r+2}{2}\right)}{\Gamma\left(\frac{\nu_r-\mu_r+1}{2}\right)} \tag{172}$$

In these equations, $\Gamma(\mathrm{x})$ is the gamma function, a well-known extension and translation of the factorial function:

$$\Gamma(\mathrm{x}) = (x-1)! \tag{173}$$

Numerical computation of the gamma function is fairly routine. Equations (167) - (172) allow the recurrence relation in (166) to be computed. Evaluating the summation for values of k up to 50 provides sufficient accuracy for the purposes of the SIFA cavity model.

The derivatives of the associated Legendre functions are straightforward closed-form expressions in terms of the functions themselves. The formulas for the derivatives of the first and second kind functions are:

$$P_{\nu_r}^{\mu_r\prime}(x) = \frac{\nu_r x P_{\nu_r}^{\mu_r}(x) - (\nu_r + \mu_r) P_{\nu_r-1}^{\mu_r}(x)}{x^2 - 1} \tag{174}$$

$$Q_{\nu_r}^{\mu_r\prime}(x) = \frac{\nu_r x Q_{\nu_r}^{\mu_r}(x) - (\nu_r + \mu_r) Q_{\nu_r-1}^{\mu_r}(x)}{x^2 - 1} \tag{175}$$

Thus, calculation of the derivatives is a simple extension of the numerical calculation used for the functions themselves.

C. Schelkunoff-type Spherical Bessel Functions

The Schelkunoff-type spherical Bessel functions of the first and second kind used in the SIFA cavity model ($\widehat{J}_{\nu_r}(x)$ and $\widehat{N}_{\nu_r}(x)$) are derived from the standard Bessel functions of the first and second kind ($J_{\nu_r}(x)$ and $N_{\nu_r}(x)$). They were originally developed by Schelkunoff as more convenient functions to use in electromagnetic

problems in spherical coordinates. The Schelkunoff-type functions are related to standard Bessel functions as follows:

$$\hat{J}_{\nu_r}(x) = \sqrt{\frac{\pi x}{2}} J_{\nu_r + 1/2}(x) \tag{176}$$

$$\hat{N}_{\nu_r}(x) = \sqrt{\frac{\pi x}{2}} N_{\nu_r + 1/2}(x) \tag{177}$$

Thus, the Schelkunoff-type functions are easily calculated once the standard Bessel functions are determined. The standard Bessel function of the first kind with fractional order ν_r can be calculated as an infinite series expression:

$$J_{\nu_r}(x) = \sum_{k=0}^{\infty} \frac{(-1)^k x^{2k+\nu_r}}{\Gamma(k+1)\Gamma(k+\nu_r+1)2^{2k+\nu_r}} \tag{178}$$

Evaluating this summation to $k = 50$ provides acceptable accuracy for the SIFA cavity model. The Bessel function of the second kind, $N_{\nu_r}(x)$, can be obtained directly from $J_{\nu_r}(x)$, rather than constructing a separate series expression:

$$N_{\nu_r}(x) = \frac{J_{\nu_r}(x)\cos(\nu_r \pi) - J_{-\nu_r}(x)}{\sin(\nu_r \pi)} \tag{179}$$

The derivatives of the Schelkunoff-type functions can also be computed in terms of the standard Bessel functions:

$$\hat{J}_{\nu_r}'(x) = \sqrt{\frac{\pi}{2}} \left[\frac{1}{2\sqrt{x}} J_{\nu_r + 1/2}(x) + \frac{\sqrt{x}}{2} \left(J_{\nu_r - 1/2}(x) - J_{\nu_r + 3/2}(x) \right) \right] \tag{180}$$

$$\hat{N}_{\nu_r}'(x) = \sqrt{\frac{\pi}{2}} \left[\frac{1}{2\sqrt{x}} N_{\nu_r + 1/2}(x) + \frac{\sqrt{x}}{2} \left(N_{\nu_r - 1/2}(x) - N_{\nu_r + 3/2}(x) \right) \right] \tag{181}$$

D. Matlab Code

The following function m-file, associated_legend.m, calculates the associated Legendre function of a number x_0 (or its derivative at x_0) given the order ν_r, the degree μ_r, and the kind of the function (first or second).

```
function out = associated_legend(x,mu,nu,kind,soln);
% Calculates the associated Legendre function of arbitrary order and
% degree as well as its derivative (of both the first and second kind).
%
% First kind:
if kind == 1
  % Function value:
  if soln == 1
    out = P(x,mu,nu);
  % Derivative value:
  elseif soln == 2
    out = (nu.*x.*P(x,mu,nu)-(nu+mu).*P(x,mu,nu-1))./(x.^2-1);
  end
% Second kind:
elseif kind == 2
  % Function value:
  if soln == 1
    out = Q(x,mu,nu);;
  % Derivative value:
  elseif soln == 2
    out = (nu.*x.*Q(x,mu,nu)-(nu+mu).*Q(x,mu,nu-1))./(x.^2-1);
  end
end
```

The function above calls another function P.m, which computes the associated Legendre function of the first kind:

```
function out = P(x,mu,nu)
% Computes the associated legendre function of the first kind with
% arbitrary degree and order for arguments abs(x)<1
%
echo off;
% Integer order and degree:
if round(mu)==mu & round(nu)==nu
  m = mu; n = nu;
  if m>n
    out = zeros(1,length(x));
  else
    L = legendre(n,x);
    out = L(m+1,:);
  end
```

```
% Non-integer order and degree:
else
  a1 = 0; a2 = 0;
  a3 = 2^mu/pi^(1/2)*cos(pi*(nu+mu)/2).*gamma((nu+mu+1)/2)./...
   gamma((nu-mu+2)/2);
  a4 = 2^(mu+1)/pi^(1/2).*sin(pi*(nu+mu)/2).*gamma((nu+mu+2)/2)./...
   gamma((nu-mu+1)/2);
  y = a3 + a4.*x;
   for k = 0:50
  new = ((mu^2+2*k^2-nu*(nu+1)).*a3+((k-2)*(1-k)+nu*(nu+1)).*a1)...
    ./((k+1).*(k+2));
  y = y + new.*x.^(k+2);
   a1 = a2;   a2 = a3;   a3 = a4;   a4 = new;
  end
  out = y;
end
```

The function associated_legend.m also calls the function N.m, which computes the associated Legendre function of the second kind:

```
function out = N(x,nu)
% Calculates the bessel function of the second kind with arbitrary
order
out = (J(x,nu).*cos(nu*pi)-J(x,-nu))./sin(nu*pi);
```

The following function m-file, Schelk_spherical_bessel.m, calculates the Schelkunoff-type spherical Bessel function of a number x_0 (or its derivative at x_0), given the order ν_r and the kind of function (first or second).

```
function out = Schelk_spherical_bessel(x,nu,kind,soln)
out1 = zeros(1,length(x));
% Calculates a Schelkenoff-type spherical bessel function of the first
or
% second kind, or its derivative
echo off;
% Standard J or Y function:
if soln == 1
   % First kind:
   if kind == 1
       % Integer:
       if round(nu+1/2)==nu+1/2
           out = sqrt(pi*x/2).*besselj(nu+1/2,x);
       % Non-integer:
       else
           out = sqrt(pi*x/2).*J(x,nu+1/2);
       end
   % Second kind:
   elseif kind == 2
```

```
        % Integer:
        if round(nu+1/2)==nu+1/2
            out = sqrt(pi*x/2).*bessely(nu+1/2,x);
        % Non-integer:
        else
            out = sqrt(pi*x/2).*N(x,nu+1/2);
        end
    end
% Derivative of J or Y:
elseif soln == 2
    % First kind:
    if kind == 1
         % Integer:
         if round(nu+1/2)==nu+1/2
            out = sqrt(pi/2).*(1./(2.*sqrt(x)).*besselj(nu+1/2,x)+...
                sqrt(x).*1/2.*(besselj(nu-1/2,x)-besselj(nu+3/2,x)));
         % Non-integer:
         else
            out = sqrt(pi/2).*(1./(2.*sqrt(x)).*J(x,nu+1/2)+sqrt(x).*...
                1/2.*(J(x,nu-1/2)-J(x,nu+3/2)));
         end
    % Second kind:
    elseif kind == 2
         % Integer:
         if round(nu+1/2)==nu+1/2
            out = sqrt(pi/2).*(1./(2.*sqrt(x)).*N(x,nu+1/2)+sqrt(x).*...
                1/2.*(N(x,nu-1/2)-N(x,nu+3/2)));
         % Non-integer:
         else
            out = sqrt(pi/2).*(1./(2.*sqrt(x)).*bessely(nu+1/2,x)+...
                sqrt(x).*1/2.*(bessely(nu-1/2,x)-bessely(nu+3/2,x)));
         end
    end
end
```

The function above calls another function, J.m, which computes the standard Bessel function (arbitrary order):

```
function out = J(x,nu)
% Calculates the bessel function of the first kind with arbitrary order
out1 = 0;
for m = 0:50
  out1 = out1+(-1).^m.*x.^(2*m+nu)./(gamma(m+1).*gamma(m+nu+1).*...
    2.^(2*m+nu));
end
out2 = sqrt(2./(pi*x)).*cos(x-pi/4-nu*pi/2);
out = (x<=40).*out1 + (x>40).*out2;
```

APPENDIX B

MATLAB CODE FOR THE NUMERICAL IMPLEMENTATION OF THE SIFA CAVITY MODEL

The first step in the numerical computation of the SIFA cavity model is to compute the modes of the cavity (i.e. the modal parameters m, μ_r, ν_r, and k_d). This is accomplished by the program res_freq_automated, which solves the necessary transcendental equations:

```
delete res_freq_automated.txt; diary res_freq_automated.txt;
clear all; close all; clc; echo on;
%
% Dielectric Substrate Constant:
er = 1;
% SIFA parameters:
Ri = 76.2e-3; Ro = 101.6e-3;
phi_w = pi/2;
theta_g = 13*pi/180;
theta_s = 11*pi/180;
phi_s = 22*pi/180;
h = Ro-Ri;
Wp = Ro*phi_w;
Wp2 = Ro*phi_s;
eep = (er+1)/2+(er-1)/2*(1+12*h/Wp)^(-1/2);
% length of patch = lp = Ro*cos(phi_w/2)*(pi/2-theta_g-theta_s)
% length of extension = le = Ro*cos(theta_s)*(phi_w-phi_s)/2
% (le/de)*(dp/lp) = cos(phi_w/2)/cos(theta_s);
theta_length = pi/2-theta_s-theta_g;
dtheta=0.412*h*(eep+.3)/(eep-.258)*(Wp/h+0.262)/(Wp/h+0.813)/Ro;
dtheta2=0.412*h*(eep+.3)/(eep-.258)*(Wp2/h+0.262)/(Wp2/h+0.813)/Ro;
theta_extend = (phi_w-phi_s)/2*cos(phi_w/2)/cos(theta_s);
Res_freq = [];
% Loop through modes:
echo off;
for m = 1:1:5
  % Calculate mu:
  mu = m*pi/(2*(theta_length+theta_s+theta_extend+dtheta+dtheta2));
  mu = m*pi/(2*(theta_length));
  % vector for nu:
  nu = linspace(floor(mu)+0.01,floor(mu)+5,500);
  % Calculate possible values for nu from transcendental equation:
  fun1 = zeros(1,length(nu));
  for i = 1:length(nu)
```

```
    fun1(i) = associated_legend(sin(-phi_w/2),mu,nu(i),2,2).*...
      associated_legend(sin(phi_w/2),mu,nu(i),1,2)-...
      associated_legend(sin(-phi_w/2),mu,nu(i),1,2).*...
      associated_legend(sin(phi_w/2),mu,nu(i),2,2);
  end
  nu_value = [];
  for i = 2:length(fun1)
    if sign(fun1(i))~=sign(fun1(i-1))
      nu_value = [nu_value nu(i-1)-fun1(i-1)*(nu(i)-nu(i-1))/...
        (fun1(i)-fun1(i-1))];
    end
  end
  % Caluclate the value of kd for each value of nu:
  for n = 1:length(nu_value)
    % Select current value of nu:
    nu = nu_value(n);
    % Vector for kd:
    kd = linspace(1,200,500);
    % Calculate value of kd through transcendental equation:
    fun2 = zeros(1,length(kd));
    for i = 1:length(kd)
      fun2(i) = Schelk_spherical_bessel(kd(i)*Ri,nu,2,2)*...
        Schelk_spherical_bessel(kd(i)*Ro,nu,1,2)-...
        Schelk_spherical_bessel(kd(i)*Ri,nu,1,2)*...
        Schelk_spherical_bessel(kd(i)*Ro,nu,2,2);
    end
    fun2 = real(fun2);
    kd_value = [];
    for i = 2:length(fun2)
      if sign(fun2(i))~=sign(fun2(i-1))
        kd_value = kd(i-1)-fun2(i-1)*(kd(i)-kd(i-1))/...
          (fun2(i)-fun2(i-1));
        break
      end
    end
    kd = kd_value;
    % Calculate resonant frequency:
    fr = kd/(2*pi*sqrt(4*pi*10^-7*er*8.854e-12));
    Res_freq = [Res_freq m mu nu kd fr/1e6];
    display(['Resonant frequency: ' num2str(fr/1e6) ' MHz']);
  end
end
% Export resonant frequencies to excel file:
rows = length(Res_freq)/5;
Res_freq = reshape(Res_freq,5,rows).';
[SUCCESS,MESSAGE]=xlswrite('Res_freq.xls',Res_freq);
if SUCCESS == 1
  display('Data successfully exported to Excel file');
end
%
echo off; diary off;
```

The program above outputs a Microsoft Excel file, Res_freq.xls, which contains all of the pertinent modal information. This spreadsheet is imported into the next program, Input_Imp.m, which computes the fields for each mode, the radiation from the side slots and primary slot, and the input impedance:

```
delete Input_Imp.txt; diary Input_Imp.txt;
clear all; close all; clc; echo on;
%
tic
eps0 = 8.854e-12; mu0 = 4*pi*10^-7; er = eps0;
% SIFA parameters:
global theta_g theta_s phi_w Ri Ro length_eff
Ri = 76.2e-3; Ro = 101.6e-3; h = Ro-Ri;
phi_w = pi/2;
theta_g = 13*pi/180;
theta_s = 11*pi/180;
phi_s = 22*pi/180;
theta_f = 21*pi/180;
rc = 0.92e-3; rp = 2.98e-3;
Wp = Ro*phi_w;
Wp2 = Ro*phi_s;
eep = (er+1)/2+(er-1)/2*(1+12*h/Wp)^(-1/2);
theta_length = pi/2-theta_s-theta_g;
dtheta=0.412*h*(eep+.3)/(eep-.258)*(Wp/h+0.262)/(Wp/h+0.813)/Ro;
dtheta2=0.412*h*(eep+.3)/(eep-.258)*(Wp2/h+0.262)/(Wp2/h+0.813)/Ro;
theta_extend = (phi_w-phi_s)/2*cos(phi_w/2)/cos(theta_s);
length_eff = theta_length+dtheta+dtheta2+theta_extend+theta_s;
length_eff = theta_length;
% Read resonant frequencies from excel file:
[NUM,TXT,RAW]=xlsread('Res_freq.xls');
m = NUM(:,1);
mu = NUM(:,2);
nu = NUM(:,3);
kmn = NUM(:,4);
num_modes = length(mu);
% Frequency span of impedance calculation:
freq = linspace(300e6,500e6,100);
% Loop through the desired frequencies:
VSWR = []; R = []; X = [];
echo off;
for i = 1:length(freq)
    f = freq(i); % Current frequency
    display(['Current frequency:' num2str(f/1e6)])
    k = 2*pi*f*sqrt(mu0*eps0); % Current wavenumber
    % Loop through the modes to be considered:
    for j = 1:num_modes
        % 3D modal solution:
        [Psi U V W] = modes3D(m(j),mu(j),nu(j),kmn(j));
        if j == 1
```

```
            Psi_total = zeros(size(Psi));
        end
        size_3D = size(U);
        U1 = reshape(U,1,size_3D(1)*size_3D(2)*size_3D(3));
        V1 = reshape(V,1,size_3D(1)*size_3D(2)*size_3D(3));
        W1 = reshape(W,1,size_3D(1)*size_3D(2)*size_3D(3));
        ustep = (Ro-Ri)/size_3D(1);
        vstep = (pi/2-theta_g-theta_s)/size_3D(2);
        wstep = (phi_w/2-(-phi_w/2))/size_3D(3);
        % Calculate the excitation coefficient inner product:
        J1 = zeros(1,length(U1));
        J_index = find((W1==min(min(min(abs(W1)))))&...
            ((abs(V1-(pi/2-theta_f)))==...
            min(min(min(abs(V1-(pi/2-theta_f)))))));
        J1(J_index) = 1;
        J = reshape(J1,size_3D(1),size_3D(2),size_3D(3));
        integrand1 = J.*conj(Psi).*U.^2.*cos(W);
        Excite_Coeff =
sum(sum(sum(integrand1*wstep,3)*vstep,2)*ustep,1);
        % Calculate the inner product in the denominator:
        integrand2 = Psi.*conj(Psi).*U.^2.*cos(W);
        Orthog_Coeff =
sum(sum(sum(integrand2*wstep,3)*vstep,2)*ustep,1);
        % Calculate the total contribution of the mode to Psi and add:
        Coeff = sqrt(-1)*2*pi*f*mu0*Excite_Coeff/Orthog_Coeff/...
            (kmn(j)^2-k^2);
        Psi_total = Psi_total + Psi*Coeff;
    end
    Psi1 = reshape(Psi_total,1,size_3D(1)*size_3D(2)*size_3D(3));
    % Compute all of the field components from Psi:
    dPsi_du = zeros(size(Psi_total));
    dPsi_dv = zeros(size(Psi_total));
    dPsi_dw = zeros(size(Psi_total));
    d2Psi_du2 = zeros(size(Psi_total));
    d2Psi_dudv = zeros(size(Psi_total));
    for i = 1:size_3D(1)
        for j = 1:size_3D(1)
            % Derivative with respect to u:
            a = zeros(1,size_3D(1)); aa = a; a(1,:) = U(:,i,j);
            aa(1,:) = Psi_total(:,i,j);
            dPsi_du(:,i,j) = num_diff(a,aa);
            % Derivative with respect to v:
            a = zeros(1,size_3D(2)); aa = a; a(1,:) = V(i,:,j);
            aa(1,:) = Psi_total(i,:,j);
            dPsi_dv(i,:,j) = num_diff(a,aa);
            % Derivative with respect to w:
            a = zeros(1,size_3D(3)); aa = a; a(1,:) = W(i,j,:);
            aa(1,:) = Psi_total(i,j,:);
            dPsi_dw(i,j,:) = num_diff(a,aa);
            % Second derivative with respect to u:
            a = zeros(1,size_3D(1)); aa = a; a(1,:) = U(:,i,j);
            aa(1,:) = dPsi_du(:,i,j);
            d2Psi_du2(:,i,j) = num_diff(a,aa);
            % Mixed derivative with respect to u and v:
```

```
            a = zeros(1,size_3D(1)); aa = a; a(1,:) = V(i,:,j);
            aa(1,:) = dPsi_du(i,:,j);
            d2Psi_dudv(:,i,j) = num_diff(a,aa);
        end
    end
    Eu = 1/(sqrt(-1)*2*pi*f*eps0)*(d2Psi_du2+k^2*Psi_total);
    Ev = -1./(sqrt(-1)*2*pi*f*eps0*U.*cos(W)).*d2Psi_dudv;
    Ew = 1./(sqrt(-1)*2*pi*f*eps0*U).*d2Psi_dudv;
    Hu = zeros(size(Psi_total));
    Hv = 1./U.*dPsi_dw;
    Hw = -1./(U.*cos(W)).*dPsi_dv;
    % Normalize the field components with respect to Eu along the feed:
    Eu1 = reshape(Eu,1,size_3D(1)*size_3D(2)*size_3D(3));
    E0 = abs(Eu1(J_index)); E0 = E0(1);
    Eu = Eu/E0; Ev = Ev/E0; Ew = Ew/E0;
    Hu = Hu/E0; Hv = Hv/E0; Hw = Hw/E0;
    Eu1 = Eu1/E0;
    % Extract the side slot, primary slot, and feed location data from
Er:
    ss = zeros(size_3D(1),size_3D(2));
    ss2 = zeros(size_3D(1),size_3D(2));
    ps = zeros(size_3D(1),size_3D(3));
    feed = zeros(1,length(J_index));
    for j = 1:size_3D(1)
        feed(1,j) = abs(Eu1(J_index(j)));
        for l = 1:size_3D(2)
            ss(j,l) = Eu(j,l,1);
            ss2(j,l) = Eu(j,l,50);
            ps(j,l) = Eu(j,1,l);
        end
    end
    % Compute the radiated power of the slots:
    [E_theta_ss1 E_phi_ss1 Ib_ss1] = side_slot(ss,f);
    [E_theta_ss2 E_phi_ss2 Ib_ss2] = side_slot2(ss2,f);
    [E_theta_ps E_phi_ps Id_ps] = primary_slot(ps,f);
    Prad = Ib_ss1+Ib_ss2+Id_ps;
    Power_radiated = [Power_radiated Prad];
    % Compute the stored electric energy:
    We =
eps0/4*sum(sum(sum((Eu.*conj(Eu)+Ev.*conj(Ev)+Ew.*conj(Ew)).*...
        U.^2.*cos(W)*ustep,1)*vstep,2)*wstep,3);
    % Compute the stored magnetic energy:
    Wm =
mu0/4*sum(sum(sum((Hu.*conj(Hu)+Hv.*conj(Hv)+Hw.*conj(Hw)).*...
        U.^2.*cos(W)*ustep,1)*vstep,2)*wstep,3);
    Stored_Energy = [Stored_Energy (Wm-We)];
    % Compute the impedance:
    Voltage = h;
    Y = (Prad+sqrt(-1)*2*2*pi*f*(We-Wm))/abs(Voltage)^2;
    Z = 1/Y;
    R = [R real(Z)];
    X = [X imag(Z)];
    Tau = (Z-50)/(Z+50);
    VSWR = [VSWR (1+abs(Tau))/(1-abs(Tau))];
```

```
    display(['VSWR = ' num2str(VSWR(end))]);
    display(['R = ' num2str(R(end))]);
    display(['X = ' num2str(X(end))]);
end
% Compute the radiation pattern:
theta = linspace(0,pi,101);
phi = linspace(0,2*pi,101);
[Theta Phi] = meshgrid(theta,phi);
E_theta = E_theta_ps;
E_phi = E_phi_ss1 + E_phi_ss2 + E_phi_ps;
E_rad_max = max(max(max(abs(sqrt(E_theta.^2+E_phi.^2)))));
E_theta = abs(E_theta/E_rad_max);
E_phi = abs(E_phi/E_rad_max);
% XY cut plane:
xy_Phi = Phi(:,51);
xy_E_theta = E_theta(:,51);
xy_E_phi = E_phi(:,51);
% XZ cut plane:
xz_Theta = [Theta(1,:) linspace(pi,2*pi,101)];
xz_E_theta = [E_theta(1,:) fliplr(E_theta(51,:))];
xz_E_phi = [E_phi(1,:) fliplr(E_phi(51,:))];
% YZ cut plane:
yz_Theta = [Theta(26,:) linspace(pi,2*pi,101)];
yz_E_theta = [E_theta(26,:) fliplr(E_theta(76,:))];
yz_E_phi = [E_phi(26,:) fliplr(E_phi(76,:))];
% Three-dimensional pattern:
X_Theta = abs(E_theta).*sin(Theta).*cos(Phi);
Y_Theta = abs(E_theta).*sin(Theta).*sin(Phi);
Z_Theta = abs(E_theta).*cos(Theta);
X_Phi = abs(E_phi).*sin(Theta).*cos(Phi);
Y_Phi = abs(E_phi).*sin(Theta).*sin(Phi);
Z_Phi = abs(E_phi).*cos(Theta);
% Plot the VSWR and Impedance curves:
plot(freq/1e6,VSWR,'Linewidth',3); grid on;
xlabel('Freq (MHz)'); ylabel('VSWR'); axis([min(freq)/1e6
max(freq)/1e6...
    1 5]);
toc
%
echo off; diary off;
```

The program above makes use of the function file modes3D.m, which does the actual computation of the three-dimensional wave potential in the cavity for each mode (including the modal coefficient):

```
function [Psi U V W] = modes3D(m,mu,nu,kmn)
%
global theta_g theta_s phi_w Ri Ro length_eff
% theta_g = 13*pi/180; theta_s = 11*pi/180;
% phi_w = pi/2;
```

```
% Ri = 76.2e-3; Ro = 101.6e-3;
mur = mu;
nur = nu;
kd = kmn;
xa = linspace(Ri,Ro,50);
A = Schelk_spherical_bessel(kd*Ri,nur,2,2).*...
  Schelk_spherical_bessel(kd*xa,nur,1,1)-...
  Schelk_spherical_bessel(kd*Ri,nur,1,2).*...
  Schelk_spherical_bessel(kd*xa,nur,2,1);
xb = linspace(theta_g,pi/2-theta_s,50);
B = cos(m*pi/(2*(pi/2-theta_s-theta_g))*(xb-theta_g));
xc = linspace(-phi_w/2,phi_w/2,50);
C = associated_legend(sin(-phi_w/2),mur,nur,2,2)*...
  associated_legend(sin(xc),mur,nur,1,1)-...
  associated_legend(sin(-phi_w/2),mur,nur,1,2).*...
  associated_legend(sin(xc),mur,nur,2,1);
% Create 3-D space for interproduct calculations over the cavity:
u = xa;
v = xb;
w = xc;
echo off;
points = length(u)*length(v)*length(w);
U = zeros(length(u),length(v),length(w)); V = U; W = U; Psi = U;
counter = 1;
for i = 1:length(u)
  for j = 1:length(v)
    for l = 1:length(w)
      U(i,j,l) = u(i);
      V(i,j,l) = v(j);
      W(i,j,l) = w(l);
      Psi(i,j,l) = A(i)*B(j)*C(l);
    end
  end
end
```

Input_Imp.m also calls the function primary_slot.m, which computes the radiation from the primary slot of the cavity:

```
function [E_theta E_phi Id] = primary_slot(ps,f)
% Computes the radiated power from the SIFA primary slot
eps0 = 8.854e-12; mu0 = 4*pi*10^-7; eta0 = sqrt(mu0/eps0);
% SIFA parameters:
Ri = 76.2e-3; Ro = 101.6e-3;
phi_w = pi/2;
theta_g = 13*pi/180;
theta_s = 11*pi/180;
phi_s = 22*pi/180;
theta_f = 21*pi/180;
er = 1; eps = er*eps0;
% Wavenumber:
k = 2*pi*f*sqrt(eps0*mu0);
% Create a mesh over the side slot geometry for the electric vector
```

```
% potential calculation:
[u_size w_size] = size(ps);
u = linspace(Ri,Ro,u_size);
w = linspace(-phi_w/2,phi_w/2,w_size);
[U W] = meshgrid(u,w);
ustep = u(2)-u(1);
wstep = w(2)-w(1);
% Create a mesh over all angles in the far field:
theta = linspace(0,pi,100); theta_length = length(theta);
phi = linspace(0,2*pi,100); phi_length = length(phi);
[Theta Phi] = meshgrid(theta,phi);
theta_step = theta(2)-theta(1);
phi_step = phi(2)-phi(1);
% Matrices to store values of electric vector potential in the far
field:
Ic_phi = zeros(theta_length,phi_length); Ic_theta = Ic_phi;
% Loop through the angles in the far field and compute the electric
vector
% potential at each angle:
for i = 1:theta_length
  for j = 1:phi_length
    theta = Theta(i,j);
    phi = Phi(i,j);
    % Cross product between normal vector and radial unit vector:
    n_cross_r_phi = U.*(cos(theta_g)*cos(theta)*cos(phi)+sin(...
      theta_g)*sin(theta));
    n_cross_r_theta = U.*cos(theta_g)*sin(phi);
    % Cosine of angle between R and R_prime:
    cosa = sin(theta)*cos(phi)*cos(W)*sin(theta_g)+sin(theta)*...
      sin(phi)*sin(W)+cos(theta)*cos(W)*cos(theta_g);
    % Compute the phase term:
    phase_term = exp(sqrt(-1)*k*U.*abs(cosa));
    % Integrand of electric vector potential:
    integrand_phi = n_cross_r_phi.*ps.*phase_term;
    integrand_theta = n_cross_r_theta.*ps.*phase_term;
    % Integrate numerically:
    integral_phi = sum(sum(integrand_phi*wstep)*ustep);
    integral_theta = sum(sum(integrand_theta*wstep)*ustep);
    % Multiply the integral by the known constants:
    Ic_phi(i,j) = -2*eps/(4*pi)*integral_phi;
    Ic_theta(i,j) = -2*eps/(4*pi)*integral_theta;
  end
end
% Compute the radiated power:
Id =
(2*pi*f)^2*eta0*sum(sum((abs(Ic_phi)^2+abs(Ic_theta)^2).*sin(Theta)...
  .*theta_step).*phi_step);
E_theta = Ic_phi;
E_phi = Ic_theta;
```

Finally, Input_Imp.m calls the functions side_slot.m and side_slot2.m, which compute the radiation from the two side slots of the cavity:

```
function [E_theta E_phi Ib] = side_slot(ss,f)
% Computes the radiated power from the SIFA side slot
eps0 = 8.854e-12; mu0 = 4*pi*10^-7; eta0 = sqrt(mu0/eps0);
% SIFA parameters:
Ri = 76.2e-3; Ro = 101.6e-3;
phi_w = pi/2;
theta_g = 13*pi/180;
theta_s = 11*pi/180;
phi_s = 22*pi/180;
theta_f = 21*pi/180;
er = 1; eps = er*eps0;
% Wavenumber:
k = 2*pi*f*sqrt(eps0*mu0);
% Create a mesh over the side slot geometry for the electric vector
% potential calculation:
[u_size v_size] = size(ss);
u = linspace(Ri,Ro,u_size);
v = linspace(theta_g,pi/2-theta_s,v_size);
[U V] = meshgrid(u,v);
ustep = u(2)-u(1);
vstep = v(2)-v(1);
% Create a mesh over all angles in the far field:
theta = linspace(0,pi,100); theta_length = length(theta);
phi = linspace(0,2*pi,100); phi_length = length(phi);
[Theta Phi] = meshgrid(theta,phi);
theta_step = theta(2)-theta(1);
phi_step = phi(2)-phi(1);
% Matrices to store values of electric vector potential in the far
field:
Ia_phi = zeros(theta_length,phi_length); Ia_theta = Ia_phi;
% Loop through the angles in the far field and compute the electric
vector
% potential for each far field direction:
for i = 1:theta_length
  for j = 1:phi_length
    theta = Theta(i,j);
    phi = Phi(i,j);
    % Cross product between normal vector and radial unit vector:
    n_cross_r_phi = U.*(sin(phi_w/2)*cos(phi_w/2)*sin(V)*cos(theta)*...
      cos(phi)-cos(phi_w/2)^2*cos(theta)*sin(phi));
    n_cross_r_theta = U.*(sin(phi_w/2)*cos(phi_w/2)*sin(V)*sin(phi)+...
      cos(phi_w/2)^2*cos(phi));
    % Cosine of angle between R and R_prime:
    cosa = sin(theta)*cos(phi)*cos(phi_w/2)*sin(V)+sin(theta)*...
      sin(phi)*sin(phi_w/2)+cos(theta)*cos(phi_w/2)*cos(V);
    % Compute the phase term:
    phase_term = exp(sqrt(-1)*k*U.*abs(cosa));
    % Integrand of electric vector potential:
    integrand_phi = n_cross_r_phi.*ss.*phase_term;
    integrand_theta = n_cross_r_theta.*ss.*phase_term;
    % Integrate numerically:
    integral_phi = sum(sum(integrand_phi*vstep)*ustep);
    integral_theta = sum(sum(integrand_theta*vstep)*ustep);
    % Multiply the integral by the known constants:
```

```
    Ia_phi(i,j) = -2*eps/(4*pi)*integral_phi;
    Ia_theta(i,j) = -2*eps/(4*pi)*integral_theta;
  end
end
% Compute the radiated power:
Ib =
(2*pi*f)^2*eta0*sum(sum((abs(Ia_phi)^2+abs(Ia_theta)^2).*sin(Theta)...
  .*theta_step).*phi_step);
E_theta = Ia_phi;
E_phi = Ia_theta;


function [E_theta E_phi Ib] = side_slot2(ss,f)
% Computes the radiated power from the SIFA side slot
eps0 = 8.854e-12; mu0 = 4*pi*10^-7; eta0 = sqrt(mu0/eps0);
% SIFA parameters:
Ri = 76.2e-3; Ro = 101.6e-3;
phi_w = pi/2;
theta_g = 13*pi/180;
theta_s = 11*pi/180;
phi_s = 22*pi/180;
theta_f = 21*pi/180;
er = 1; eps = er*eps0;
% Wavenumber:
k = 2*pi*f*sqrt(eps0*mu0);
% Create a mesh over the side slot geometry for the electric vector
% potential calculation:
[u_size v_size] = size(ss);
u = linspace(Ri,Ro,u_size);
v = linspace(theta_g,pi/2-theta_s,v_size);
[U V] = meshgrid(u,v);
ustep = u(2)-u(1);
vstep = v(2)-v(1);
% Create a mesh over all angles in the far field:
theta = linspace(0,pi,101); theta_length = length(theta);
phi = linspace(0,2*pi,101); phi_length = length(phi);
[Theta Phi] = meshgrid(theta,phi);
theta_step = theta(2)-theta(1);
phi_step = phi(2)-phi(1);
% Matrices to store values of electric vector potential in the far
field:
Ia_phi = zeros(theta_length,phi_length); Ia_theta = Ia_phi;
% Loop through the angles in the far field and compute the electric
vector
% potential for each far field direction:
for i = 1:theta_length
    for j = 1:phi_length
        theta = Theta(i,j);
        phi = Phi(i,j);
        % Cross product between normal vector and radial unit vector:
        n_cross_r_phi =
U.*(sin(phi_w/2)*cos(phi_w/2)*sin(V)*cos(theta)*...
            cos(phi)-cos(phi_w/2)^2*cos(theta)*sin(phi));
```

```
        n_cross_r_theta = -
U.*(sin(phi_w/2)*cos(phi_w/2)*sin(V)*sin(phi)+...
            cos(phi_w/2)^2*cos(phi));
        % Cosine of angle between R and R_prime:
        cosa = sin(theta)*cos(phi)*cos(phi_w/2)*sin(V)-sin(theta)*...
            sin(phi)*sin(phi_w/2)+cos(theta)*cos(phi_w/2)*cos(V);
        % Compute the phase term:
        phase_term = exp(sqrt(-1)*k*U.*abs(cosa));
        % Integrand of electric vector potential:
        integrand_phi = n_cross_r_phi.*ss.*phase_term;
        integrand_theta = n_cross_r_theta.*ss.*phase_term;
        % Integrate numerically:
        integral_phi = sum(sum(integrand_phi*vstep)*ustep);
        integral_theta = sum(sum(integrand_theta*vstep)*ustep);
        % Multiply the integral by the known constants:
        Ia_phi(i,j) = -2*eps/(4*pi)*integral_phi;
        Ia_theta(i,j) = -2*eps/(4*pi)*integral_theta;
    end
end
% Compute the radiated power:
Ib =
(2*pi*f)^2*eta0*sum(sum((abs(Ia_phi)^2+abs(Ia_theta)^2).*sin(Theta)...
    .*theta_step).*phi_step);
E_theta = Ia_phi;
E_phi = Ia_theta;
```

APPENDIX C

MATLAB CODE FOR SIMULATION OF A LINE-OF-SIGHT REMOTE SIFA LINK

The remote, two-node, LOS link problem requires computations in Matlab using data extracted from HFSS simulations. The primary Matlab program used to do this is LOS_comm.m, shown below. This program reads data in from carefully crafted Excel spreadsheets (the details of which will not be given here). The data is used to calculate the power transfer from transmitter to receiver and subsequently the PDF distributions discussed in Chapter VI.

```
delete LOS_comm.txt; diary LOS_comm.txt;
clear all; close all; clc; echo on;
%
% This program imports data from simulations of the SIFA above ground.
It
% performs a monte carlo analysis of a LOS link between transmitting
and
% receiving SIFAs.  In variable names, the suffix "a" denotes the
uncoated
% SIFA variety, while "b" denotes the coated variety; the "1" suffix
% denotes the transmitting SIFA, while "2" denotes the receiving SIFA.
%
% Transmit Power:
Pt = 1;
% Wavelength:
lambda_a = 3e8/412e6;
lambda_b = 3e8/74.4e6;
% Read in electric field data for different orientations above ground:
[E_theta_1a E_phi_1a E_theta_angle_1a E_phi_angle_1a E_theta_2a ...
    E_phi_2a E_theta_angle_2a E_phi_angle_2a] = E_field_read(1);
[E_theta_1b E_phi_1b E_theta_angle_1b E_phi_angle_1b E_theta_2b ...
    E_phi_2b E_theta_angle_2b E_phi_angle_2b] = E_field_read(2);
% Read in gain data for different orientations above ground:
[Gain_theta_1a Gain_phi_1a Gain_theta_2a Gain_phi_2a] = Gain_read(1);
[Gain_theta_1b Gain_phi_1b Gain_theta_2b Gain_phi_2b] = Gain_read(2);
Gain_1a = Gain_theta_1a + Gain_phi_1a;
Gain_2a = Gain_theta_2a + Gain_phi_2a;
Gain_1b = Gain_theta_1b + Gain_phi_1b;
Gain_2b = Gain_theta_2b + Gain_phi_2b;
% Read in VSWR for different orientations above ground:
VSWRa = VSWR_read(1);
```

```
VSWRb = VSWR_read(2);
% Read in radiation efficiency for different orientations above ground:
Rad_eff_1a = Rad_eff_read(1); Rad_eff_2a = Rad_eff_1a;
Rad_eff_1b = Rad_eff_read(2); Rad_eff_2b = Rad_eff_1b;
% Read in bandwidth for different orientations above ground:
BW_1a = Bandwidth_read(1); BW_2a = BW_1a;
BW_1b = Bandwidth_read(2); BW_2b = BW_1b;
% Calculate Reflection Coefficient from VSWR:
Gamma_a = (VSWRa-1)./(VSWRa+1);
Gamma_b = (VSWRb-1)./(VSWRb+1);
% Dimensions specifying the number of variations in orientation:
[x_size y_size] = size(VSWRa);
% Received Power cell arrays:
Pr_a = {};
Pr_b = {};
% Storage arrays for other data:
Transmitter_Gain_a = []; Receiver_Gain_a = [];
Transmitter_Match_a = []; Receiver_Match_a = [];
Path_loss_a = []; Pr_cut_a = [];
Transmitter_Gain_b = []; Receiver_Gain_b = [];
Transmitter_Match_b = []; Receiver_Match_b = [];
Path_loss_b = []; Pr_cut_b = [];
% Distance vector:
d = logspace(0,3); d_size = length(d);
% Distance at which to take a cut of the received power:
d_cut = 100;
cut_index = find(min(abs(d-d_cut))==abs(d-d_cut));
% Multipath factor:
n = 2;
% Loop through the various orientations of the transmitter and
receiver:
echo off;
count = 1;
total_count = x_size^2*y_size^2;
file1_a = fopen('Received_Power_Uncoated.bin','w');
file1_b = fopen('Received_Power_Coated.bin','w');
file2_a = fopen('Data_Uncoated.bin','w');
file2_b = fopen('Data_Coated.bin','w');
file3_a = fopen('Capacity_Uncoated.bin','w');
file3_b = fopen('Capacity_Coated.bin','w');
Bandwidth_a_average = 0; Bandwidth_b_average = 0;
for i = 1:x_size
    for j = 1:y_size
        for ii = 1:x_size
            for jj = 1:y_size
                % Uncoated SIFA
                % Polarization efficiency:
                p_1a = E_phi_1a(i,j)/E_theta_1a(i,j);
                p_2a = E_phi_2a(ii,jj)/E_theta_2a(ii,jj);
                delta_1a = E_phi_angle_1a(i,j) - E_theta_angle_1a(i,j);
                delta_2a = E_phi_angle_1a(i,j) - E_theta_angle_1a(i,j);
                Tau_pol_a = (1+abs(p_1a).^2.*abs(p_2a).^2+2*...
                    abs(p_1a).*abs(p_2a).*cos(delta_1a-delta_2a))./...
                    ((1+abs(p_1a).^2).*(1+abs(p_2a).^2));
```

```
% Received power:
Pr_a = Pt.*Gain_1a(i,j).*Gain_2a(ii,jj).*...
    Tau_pol_a.*(1-Gamma_a(i,j).^2).*...
    (1-Gamma_a(ii,jj).^2).*...
    Rad_eff_1a(i,j).*Rad_eff_2a(ii,jj).*...
    (lambda_a./(4*pi.*d)).^n;
Pr_dB_a = 10.*log10(Pr_a./1e-3);
fwrite(file1_a,Pr_dB_a,'double');
Transmitter_Gain_a = Gain_1a(i,j);
Receiver_Gain_a = Gain_2a(ii,jj);
Transmitter_Match_a = (1-Gamma_a(i,j).^2);
Receiver_Match_a = (1-Gamma_a(ii,jj).^2);
Path_loss_a = (lambda_a./(4*pi.*d(1))).^n;
Pr_cut_a = 10.*log10(Pr_a(cut_index)/1e-3);
fwrite(file2_a,[Path_loss_a Pr_cut_a Receiver_Gain_a
...
    Receiver_Match_a Transmitter_Gain_a ...
    Transmitter_Match_a Tau_pol_a],'double');
% Effective Bandwidth:
B_min_1a = BW_1a(i,j*2-1); B_max_1a = BW_1a(i,j*2);
B_min_2a = BW_2a(ii,jj*2-1); B_max_2a = BW_2a(ii,jj*2);
B_min_a = max([B_min_1a B_min_2a]);
B_max_a = min([B_max_1a B_max_2a]);
BW_a = B_max_a - B_min_a;
if BW_a < 0
    BW_a = 0;
end
Bandwidth_a_average = (Bandwidth_a_average*...
    (count-1)+BW_a)/count;
% Channel Capacity:
SNR = linspace(0,30);
C_a = BW_a*log2(1+SNR);
fwrite(file3_a,C_a,'double');
% Coated SIFA
% Polarization efficiency:
p_1b = E_phi_1b(i,j)/E_theta_1b(i,j);
p_2b = E_phi_2b(ii,jj)/E_theta_2b(ii,jj);
delta_1b = E_phi_angle_1b(i,j) - E_theta_angle_1b(i,j);
delta_2b = E_phi_angle_1b(i,j) - E_theta_angle_1b(i,j);
Tau_pol_b = (1+abs(p_1b).^2.*abs(p_2b).^2+2*...
    abs(p_1b).*abs(p_2b).*cos(delta_1b-delta_2b))./...
    ((1+abs(p_1b).^2).*(1+abs(p_2b).^2));
% Received power:
Pr_b = Pt.*Gain_1b(i,j).*Gain_2b(ii,jj).*...
    Tau_pol_b.*(1-Gamma_b(i,j).^2).*...
    (1-Gamma_b(ii,jj).^2).*...
    Rad_eff_1b(i,j).*Rad_eff_2b(ii,jj).*...
    (lambda_b./(4*pi.*d)).^n;
Pr_dB_b = 10.*log10(Pr_b./1e-3);
fwrite(file1_b,Pr_dB_b,'double');
Transmitter_Gain_b = Gain_1b(i,j);
Receiver_Gain_b = Gain_2b(ii,jj);
Transmitter_Match_b = (1-Gamma_b(i,j).^2);
Receiver_Match_b = (1-Gamma_b(ii,jj).^2);
```

```
                Path_loss_b = (lambda_b./(4*pi.*d(1))).^n;
                Pr_cut_b = 10.*log10(Pr_b(cut_index)/1e-3);
                fwrite(file2_b,[Path_loss_b Pr_cut_b Receiver_Gain_b
...
                    Receiver_Match_b Transmitter_Gain_b ...
                    Transmitter_Match_b Tau_pol_b],'double');
                % Effective Bandwidth:
                B_min_1b = BW_1b(i,j*2-1); B_max_1b = BW_1b(i,j*2);
                B_min_2b = BW_2b(ii,jj*2-1); B_max_2b = BW_2b(ii,jj*2);
                B_min_b = max([B_min_1b B_min_2b]);
                B_max_b = min([B_max_1b B_max_2b]);
                BW_b = B_max_b - B_min_b;
                if BW_b < 0
                    display('got here');
                    display([num2str(B_min_b) ', ' num2str(B_max_b)]);
                    display([num2str(B_max_1b) ', '
num2str(B_max_2b)]);
                    BW_b = 0;
                end
                Bandwidth_b_average = (Bandwidth_b_average*...
                    (count-1)+BW_b)/count;
                % Channel Capacity:
                SNR = linspace(0,30);
                C_b = BW_b*log2(1+SNR);
                fwrite(file3_b,C_b,'double');
                % Display progress:
                if mod(count,5000)==0
                    display(['Looping through orientations...Progress
'...
                        num2str(count/total_count*100) '%']);
                end
                % Go to next orientation:
                count = count+1;
                pack
            end
        end
    end
end
fclose(file1_a); fclose(file1_b); fclose(file2_a); fclose(file2_b);
fclose(file3_a); fclose(file3_b);
% Open the files containing the path loss curves:
file2_a = fopen('Data_Uncoated.bin','r');
file2_b = fopen('Data_Coated.bin','r');
% Extract data from the files:
Data_Matrix_a = fread(file2_a,total_count*7,'double');
Data_Matrix_b = fread(file2_b,total_count*7,'double');
Data_Matrix_a_reshape = reshape(Data_Matrix_a,7,total_count);
Multipath_a = Data_Matrix_a_reshape(1,:);
Pr_cut_a = Data_Matrix_a_reshape(2,:);
Receiver_Gain_a = Data_Matrix_a_reshape(3,:);
Receiver_Match_a = Data_Matrix_a_reshape(4,:);
Transmitter_Gain_a = Data_Matrix_a_reshape(5,:);
Transmitter_Match_a = Data_Matrix_a_reshape(6,:);
Pol_eff_a = Data_Matrix_a_reshape(7,:);
```

```
Data_Matrix_b_reshape = reshape(Data_Matrix_b,7,total_count);
Multipath_b = Data_Matrix_b_reshape(1,:);
Pr_cut_b = Data_Matrix_b_reshape(2,:);
Receiver_Gain_b = Data_Matrix_b_reshape(3,:);
Receiver_Match_b = Data_Matrix_b_reshape(4,:);
Transmitter_Gain_b = Data_Matrix_b_reshape(5,:);
Transmitter_Match_b = Data_Matrix_b_reshape(6,:);
Pol_eff_b = Data_Matrix_b_reshape(7,:);
fclose(file2_a); fclose(file2_b);
% Determine the probability distribution of the received power:
Pr_domain = linspace(min([min(Pr_cut_a) min(Pr_cut_b)]),...
    max([max(Pr_cut_a) max(Pr_cut_b)]),1000);
CDF_a = []; CDF_b = [];
for i = 1:length(Pr_domain)
    A = find(Pr_cut_a<=Pr_domain(i));
    B = find(Pr_cut_b<=Pr_domain(i));
    CDF_a = [CDF_a length(A)/length(Pr_cut_a)];
    CDF_b = [CDF_b length(B)/length(Pr_cut_b)];
end
figure; plot(Pr_domain,CDF_a); grid on; hold on;
axis([Pr_domain(1) Pr_domain(end) 0 1]); title('CDF of Received
Power');
plot(Pr_domain,CDF_b,'r');
PDF_a = num_diff(Pr_domain,CDF_a);
PDF_b = num_diff(Pr_domain,CDF_b);
Pr_domain_step = Pr_domain(2)-Pr_domain(1);
scale_a = sum(PDF_a*Pr_domain_step);
scale_b = sum(PDF_b*Pr_domain_step);
PDF_a = PDF_a/scale_a;
PDF_b = PDF_b/scale_b;
Pr_normal = max([PDF_a PDF_b]);
PDF_a = PDF_a/Pr_normal;
PDF_b = PDF_b/Pr_normal;
figure; plot(Pr_domain,PDF_a); grid on; hold on; ...
    title('PDF of Received Power');
plot(Pr_domain,PDF_b,'r');
% Determine the distribution of the VSWR:
VSWR_domain = linspace(1,5,1000);
CDF_VSWR_a = []; CDF_VSWR_b = [];
for i = 1:length(VSWR_domain)
    A = find(VSWRa<=VSWR_domain(i));
    B = find(VSWRb<=VSWR_domain(i));
    CDF_VSWR_a = [CDF_VSWR_a length(A)/length(VSWRa)];
    CDF_VSWR_b = [CDF_VSWR_b length(B)/length(VSWRb)];
end
figure; plot(VSWR_domain,CDF_VSWR_a); grid on; hold on; ...
    title('CDF of VSWR');
plot(VSWR_domain,CDF_VSWR_b,'r');
PDF_VSWR_a = num_diff(VSWR_domain,CDF_VSWR_a);
PDF_VSWR_b = num_diff(VSWR_domain,CDF_VSWR_b);
VSWR_domain_step = VSWR_domain(2)-VSWR_domain(1);
scale_a = sum(PDF_VSWR_a*VSWR_domain_step);
scale_b = sum(PDF_VSWR_b*VSWR_domain_step);
PDF_VSWR_a = PDF_VSWR_a/scale_a;
```

```
PDF_VSWR_b = PDF_VSWR_b/scale_b;
VSWR_normal = max([PDF_VSWR_a PDF_VSWR_b]);
PDF_VSWR_a = PDF_VSWR_a/VSWR_normal;
PDF_VSWR_b = PDF_VSWR_b/VSWR_normal;
figure; plot(VSWR_domain,PDF_VSWR_a); grid on; hold on; ...
    title('PDF of VSWR');
plot(VSWR_domain,PDF_VSWR_b,'r');
% Determine the distribution of the radiation efficiency:
RE_domain = linspace(0,1,1000);
CDF_RE_a = []; CDF_RE_b = [];
for i = 1:length(RE_domain)
    A = find(Rad_eff_1a<=RE_domain(i));
    B = find(Rad_eff_1b<=RE_domain(i));
    CDF_RE_a = [CDF_RE_a length(A)/length(Rad_eff_1a)];
    CDF_RE_b = [CDF_RE_b length(B)/length(Rad_eff_1b)];
end
figure; plot(RE_domain,CDF_RE_a); grid on; hold on; ...
    title('CDF of Radiation Efficiency');
plot(RE_domain,CDF_RE_b,'r');
PDF_RE_a = num_diff(RE_domain,CDF_RE_a);
PDF_RE_b = num_diff(RE_domain,CDF_RE_b);
RE_domain_step = RE_domain(2)-RE_domain(1);
scale_a = sum(PDF_RE_a*RE_domain_step);
scale_b = sum(PDF_RE_b*RE_domain_step);
PDF_RE_a = PDF_RE_a/scale_a;
PDF_RE_b = PDF_RE_b/scale_b;
RE_normal = max([PDF_RE_a PDF_RE_b]);
PDF_RE_a = PDF_RE_a/RE_normal;
PDF_RE_b = PDF_RE_b/RE_normal;
figure; plot(RE_domain,PDF_RE_a); grid on; hold on; ...
    title('PDF of Radiation Efficiency');
plot(RE_domain,PDF_RE_b,'r');
% Determine the distribution of the polarization efficiency:
PE_domain = linspace(0,1,1000);
CDF_PE_a = []; CDF_PE_b = [];
for i = 1:length(PE_domain)
    A = find(Pol_eff_a<=PE_domain(i));
    B = find(Pol_eff_b<=PE_domain(i));
    CDF_PE_a = [CDF_PE_a length(A)/length(Pol_eff_a)];
    CDF_PE_b = [CDF_PE_b length(B)/length(Pol_eff_b)];
end
figure; plot(PE_domain,CDF_PE_a); grid on; hold on; ...
    title('CDF of Polarization Efficiency');
plot(PE_domain,CDF_PE_b,'r');
PDF_PE_a = num_diff(PE_domain,CDF_PE_a);
PDF_PE_b = num_diff(PE_domain,CDF_PE_b);
PE_domain_step = PE_domain(2)-PE_domain(1);
scale_a = sum(PDF_PE_a*PE_domain_step);
scale_b = sum(PDF_PE_b*PE_domain_step);
PDF_PE_a = PDF_PE_a/scale_a;
PDF_PE_b = PDF_PE_b/scale_b;
PE_normal = max([PDF_PE_a PDF_PE_b]);
PDF_PE_a = PDF_PE_a/PE_normal;
PDF_PE_b = PDF_PE_b/PE_normal;
```

```
figure; plot(PE_domain,PDF_PE_a); grid on; hold on; ...
    title('PDF of Polarization Efficiency');
plot(PE_domain,PDF_PE_b,'r');
% Calculate Lifetime:
energy = 5641;
Rb = 0;
pps = 0;
packet_len = logspace(5,8);
% life = energy*Rb./(pps*packet_len*Pt);
%plot(packet_len,life);
% Extract, plot, and and export minimum and maximum path loss curves:
file_a1 = fopen('Received_Power_Uncoated.bin','r');
file_b1 = fopen('Received_Power_Coated.bin','r');
Rec_Matrix_a = fread(file_a1,total_count*d_size,'double');
Rec_Matrix_a_reshape = reshape(Rec_Matrix_a,d_size,total_count);
min_index_a = find(min(Pr_cut_a)==Pr_cut_a); min_index_a =
min_index_a(1);
if length(min_index_a) > 1
    min_index_a = min_index_a(1);
end
min_path_a = Rec_Matrix_a_reshape(:,min_index_a);
max_index_a = find(max(Pr_cut_a)==Pr_cut_a);
if length(max_index_a) > 1
    max_index_a = max_index_a(1);
end
max_path_a = Rec_Matrix_a_reshape(:,max_index_a);
clear('Rec_Matrix_a','Rec_Matrix_a_reshape');
Rec_Matrix_b = fread(file_b1,total_count*d_size,'double');
Rec_Matrix_b_reshape = reshape(Rec_Matrix_b,d_size,total_count);
min_index_b = find(min(Pr_cut_b)==Pr_cut_b);
if length(min_index_b) > 1
    min_index_b = min_index_b(1);
end
min_path_b = Rec_Matrix_b_reshape(:,min_index_b);
max_index_b = find(max(Pr_cut_b)==Pr_cut_b);
if length(max_index_b) > 1
    max_index_b = max_index_b(1);
end
max_path_b = Rec_Matrix_b_reshape(:,max_index_b);
figure; semilogx(d,min_path_a,'--b',d,min_path_b,'--
r',d,max_path_a,'b',...
    d,max_path_b,'r'); grid on;
xlabel('Log distance'); ylabel('Received Power (dBm');
title(['Received Power as a Function of Distance, '...
    'Transmitted Power = 1 W']);
Export_table_1 = zeros(length(d),5);
Export_table_1(:,1) = d;
Export_table_1(:,2) = min_path_a;
Export_table_1(:,3) = max_path_a;
Export_table_1(:,4) = min_path_b;
Export_table_1(:,5) = max_path_b;
[success message] =
xlswrite('Calculated_Data\min_max_path_loss.xls',...
    Export_table_1);
```

```
% Extract, plot, and export channel capacity curves:
file_a3 = fopen('Capacity_Uncoated.bin','r');
file_b3 = fopen('Capacity_Coated.bin','r');
Cap_Matrix_a = fread(file_a3,total_count*length(SNR),'double');
Cap_Matrix_a_reshape = reshape(Cap_Matrix_a,length(SNR),total_count);
Cap_min_index_a = find(sum(Cap_Matrix_a_reshape,1) == ...
    min(sum(Cap_Matrix_a_reshape,1)));
if length(Cap_min_index_a) > 1
    Cap_min_index_a = Cap_min_index_a(1);
end
Cap_max_index_a = find(sum(Cap_Matrix_a_reshape,1) == ...
    max(sum(Cap_Matrix_a_reshape,1)));
if length(Cap_max_index_a) > 1
    Cap_max_index_a = Cap_max_index_a(1);
end
Cap_curve_min_a = Cap_Matrix_a_reshape(:,Cap_min_index_a);
Cap_curve_max_a = Cap_Matrix_a_reshape(:,Cap_max_index_a);
Cap_mean_a = mean(Cap_Matrix_a_reshape,2).';
figure; plot(SNR,Cap_mean_a,'b',SNR,Cap_curve_min_a,'--b',SNR,...
    Cap_curve_max_a,'--b'); grid on; hold on;
Cap_Matrix_b = fread(file_b3,total_count*length(SNR),'double');
Cap_Matrix_b_reshape = reshape(Cap_Matrix_b,length(SNR),total_count);
Cap_min_index_b = find(sum(Cap_Matrix_b_reshape,1) == ...
    min(sum(Cap_Matrix_b_reshape,1)));
if length(Cap_min_index_b) > 1
    Cap_min_index_b = Cap_min_index_b(1);
end
Cap_max_index_b = find(sum(Cap_Matrix_b_reshape,1) == ...
    max(sum(Cap_Matrix_b_reshape,1)));
if length(Cap_max_index_b) > 1
    Cap_max_index_b = Cap_max_index_b(1);
end
Cap_curve_min_b = Cap_Matrix_b_reshape(:,Cap_min_index_b);
Cap_curve_max_b = Cap_Matrix_b_reshape(:,Cap_max_index_b);
Cap_mean_b = mean(Cap_Matrix_b_reshape,2).';
plot(SNR,Cap_mean_b,'r',SNR,Cap_curve_min_b,'--r',SNR,...
    Cap_curve_max_b,'--r');
Export_table_6 = zeros(length(SNR),7);
Export_table_6(:,1) = SNR;
Export_table_6(:,2) = Cap_mean_a;
Export_table_6(:,3) = Cap_curve_min_a;
Export_table_6(:,4) = Cap_curve_max_a;
Export_table_6(:,5) = Cap_mean_b;
Export_table_6(:,6) = Cap_curve_min_b;
Export_table_6(:,7) = Cap_curve_max_b;
[success message] = xlswrite('Calculated_Data\Capacity.xls',...
    Export_table_6);
% Calculate, plot, and export lifetime:
Energy = 5641;
packet_rate = 1;
packet_length = logspace(2,8);
lifetime_a =
Energy*Cap_mean_a(34)*1e6./(packet_rate*packet_length*Pt)...
    /86400;
```

```
lifetime_b =
Energy*Cap_mean_b(34)*1e6./(packet_rate*packet_length*Pt)...
    /86400;
figure; semilogx(packet_length,lifetime_a,'b',packet_length,...
    lifetime_b,'r');
grid on; ylim([0 10]);
[success message] = xlswrite('Calculated_Data\Lifetime.xls',...
    [packet_length.' lifetime_a.' lifetime_b.']);
% Export CDF and PDF curves of received power:
Export_table_2 = zeros(length(Pr_domain),5);
Export_table_2(:,1) = Pr_domain;
Export_table_2(:,2) = CDF_a;
Export_table_2(:,3) = PDF_a;
Export_table_2(:,4) = CDF_b;
Export_table_2(:,5) = PDF_b;
[success message] = xlswrite('Calculated_Data\prob_dist_Pr.xls',...
    Export_table_2);
% Export CDF and PDF curves of radiation efficiency:
Export_table_3 = zeros(length(RE_domain),5);
Export_table_3(:,1) = RE_domain;
Export_table_3(:,2) = CDF_RE_a;
Export_table_3(:,3) = PDF_RE_a;
Export_table_3(:,4) = CDF_RE_b;
Export_table_3(:,5) = PDF_RE_b;
[success message] = xlswrite('Calculated_Data\prob_dist_RE.xls',...
    Export_table_3);
% Export CDF and PDF curves of polarization efficiency:
Export_table_4 = zeros(length(PE_domain),5);
Export_table_4(:,1) = PE_domain;
Export_table_4(:,2) = CDF_PE_a;
Export_table_4(:,3) = PDF_PE_a;
Export_table_4(:,4) = CDF_PE_b;
Export_table_4(:,5) = PDF_PE_b;
[success message] = xlswrite('Calculated_Data\prob_dist_PE.xls',...
    Export_table_4);
% Export CDF and PDF curves of VSWR:
Export_table_5 = zeros(length(VSWR_domain),5);
Export_table_5(:,1) = VSWR_domain;
Export_table_5(:,2) = CDF_VSWR_a;
Export_table_5(:,3) = PDF_VSWR_a;
Export_table_5(:,4) = CDF_VSWR_b;
Export_table_5(:,5) = PDF_VSWR_b;
[success message] = xlswrite('Calculated_Data\prob_dist_VSWR.xls',...
    Export_table_5);
%
echo off; diary off;
```

VITA

Name:	David Lee Rolando
Address:	3128 TAMU, 214 Zachry Bldg., College Station, TX, 77843
Email Address:	r25.david@gmail.com
Education:	B.S., Electrical Engineering, Texas A&M University, 2008 M.S., Electrical Engineering, Texas A&M University, 2010